AN ABSTRACT OF THE THESIS OF

Patricio A. Catalán Mondaca for the degree of Master of Ocean Engineering in Ocean Engineering presented on June, 10 2005.

Title: Hybrid Approach to Estimating Nearshore Bathymetry using Remote Sensing

Abstract approved:

Merrick C. Haller

The characterization of bathymetry and its time evolution is very important for both oceanographic science applications, and for societal reasons relating to coastal engineering and development. Historically, the process of depth surveying has been costly and labor-intensive. This is especially true in nearshore regions, hence a method that is both economic and reliable is of great interest. In this regard, depth inversion techniques take advantage of the interaction between the surface wave field and the underlying bathymetry such that observations of surface wave propagation can be coupled with a dispersion relation to infer bathymetry. Using field measurements, several different types of wave observation data have been tested in inversion methods, e.g. arrays of pressure sensors (*Holland*, 2001), marine radar (*Bell*, 1999), aerial photogrammetry (*Dugan et al.*, 2001) and video imagery (*Stockdon and Holman*, 2000). Typically, these studies use the linear wave dispersion relation and measured wave phase speeds (c) to perform the inversion, and agreement is generally good in intermediate water depths in the absence of currents; errors increase as waves enter shallow water, increase in nonlinearity, and eventually break. In addition, numerical techniques exist that account for some nonlinear processes (e.g. *Kennedy et al.*, 2000b; *Misra et al.*, 2003) but they require more input data, usually in the form of high resolution free surface measurements. These nonlinear

methods can potentially make improved depth estimates, however,they have only been tested with synthetic data.

In this study, we undertake a novel approach for investigating phase speeds of nonlinear waves and the potential for using them for depth inversions. The approach is novel in the sense that our observational data set consists of both in situ and remotely sensed data and also high resolution numerical data for interpolating between the in situ measurements. Our observations were made from a set of laboratory experiments conducted in large scale wave flume. Laboratory wave conditions included both regular and random waves and a range of wave heights and periods were considered. The final data set used for the depth inversion algorithm was reduced to regular cases only.

The wave height profile $H(x)$ is simulated with high spatial resolution using a combined refraction/difraction model REF/DIF1 (*Kirby and Dalrymple*, 1994), where the in situ data is used for calibration. Next, wave parameters such as phase speed, wavenumber and frequency are estimated based on the remote video measurements. The resulting hybrid data set is used as input for performing depth inversion including nonlinearity using the composite dispersion relation of *Kirby and Dalrymple* (1986).

Results indicate that inclusion of nonlinearity significantly improves the retrieved depths, especially in shallow water. The resulting degree of accuracy is comparable with previous observations for intermediate water. Analysis of the error suggests that the main source of error can be attributed to the phase speed estimation, thus it is apparent that the composite dispersion equation is capable of explaining the principal physical process well.

Hybrid Approach to Estimating Nearshore Bathymetry using Remote Sensing

by

Patricio A. Catalán Mondaca

A THESIS

submitted to

Oregon State University

in partial fulfillment of
the requirements for the
degree of

Master of Ocean Engineering

Presented June, 10 2005

Commencement June 2006

Master of Ocean Engineering thesis of Patricio A. Catalán Mondaca

presented on June, 10 2005

APPROVED:

Major Professor, representing Ocean Engineering

Head of the Department of Civil, Construction and Environmental Enginnering

---

Dean of the Graduate School

I understand that my thesis will become part of the permanent collection of the Oregon State University libraries. My signature below authorizes release of my thesis to any reader upon request

---

Patricio A. Catalán Mondaca, Author

ACKNOWLEDGEMENTS

I would like to thank Dr. Merrick Haller for his continuous support, help and guidance throughout the project, and helping me on seeing things from the brighter side. I would also like to thank all the people who helped me to get and process the data for this project, Dr. Rob Holman and all the Coastal Imaging Lab people (Dan, Jason, Chris and John) and Dr. Dan Cox and the O.H. Hindsdale Wave Research Laboratory staff (Tim, Terry and Chris). Additionally I would like to thank Dr. Harry Yeh and Dr. Philip Humpfrey for being part of my committee.

Finally, I would like to thank my muses, Ximena and Beatriz, for their love and support.

TABLE OF CONTENTS

TABLE OF CONTENTS (Continued)

LIST OF FIGURES

LIST OF FIGURES (Continued)

LIST OF TABLES

1. INTRODUCTION

This study investigates how the inclusion of nonlinearity affects the accuracy of depth estimates using remotely sensed wave data. Typically depth inversions using field data are based on the linear dispersion relation due to its simplicity and the existing limitations on obtaining a remote a data set suitable for nonlinear inversions. On the other hand, depth inversions using synthetically generated data have shown that inclusion of nonlinear effects can significatively improve the accuracy of depth estimations, especially in shallow water. However, the equations used are usually more complex and require a high quality data set typically consisting of highly resolved free surface records.

It is of interest then, to find a technique than can provide a method capable of including nonlinear effects, though simple enough to be used with field data. One feasible alternative is the use of a dispersion relation on the form of the composite dispersion equation of *Kirby and Dalrymple* (1986). This equation includes nonlinearity by incorporating a wave amplitude profile which, in principle, is the simplest variable to be obtained from field data. Though current status of the remote sensing techniques does not provide this data set, some methods show the potential to do so in the future.

Therefore, in this study we use a hybrid data set consisting of remotely sensed wave data combined with numerically simulated amplitude profiles to test the capabilities of the composite dispersion equation for depth inversions. Experiments were conducted in a laboratory facility under controlled conditions for a fixed bathymetric profile.

The present document is organized as follows. Previous work done in the field of depth inversions is reviewed and analyzed on Chapter 2, with special emphasis in characterizing the previously observed sources of error. Chapter 3 describes the methodology used in this study to perform the depth inversion, describing the nonlinear model to be used, experimental set up, data collection and analysis techniques used. Estimation of wave parameters and retrieved depth results are discussed in detail on Chapter 4, and overall conclusions are presented on Chapter 5.

2. LITERATURE REVIEW

2.1 Introduction

The nearshore is a region where several human activities take place, like recreation, fishing, navigation, etc. and it may also provide protection against environmental hazards such as flooding and many others. At the same time it is an interesting region from a scientific point of view, because it is an environment characterized by a dynamic interaction between waves and the underlying bathymetry, where breaking waves and currents induce sediment transport reshaping the coastal morphology. In turn, these bathymetric changes provide feedback to the wave field, modifying it and hence inducing eventually more change. Temporal and spatial scales vary over several orders of magnitude, and this results in morphologic features with different degrees of complexity. Thus the understanding of the processes that take place in this region is important from both societal and scientific perspectives, with an eventual long term goal of improving management and increased safety for human activities.

In order to improve the understanding of this active zone, the bottom topography has proven to be a key factor. Even under the assumption of no bathymetric change, for instance for short temporal scales, the underlying bottom profile is one of the primary inputs required to model wave hydrodynamics and other nearshore processes such as sediment transport. Good quality bathymetric data is hence required in order to identify correctly the physical processes that are taking place. Since under such a scheme bathymetry is the input, it has been defined as the "forward" problem (*Narayanan et al.*, 2004).

However, bathymetric data collection is not an easy task. Traditional surveying methods are labor intensive as they usually require manual installation of equipment under varying wave conditions. Even using advanced techniques such as global positioning systems, the process is expensive in labor, time and money, and often dangerous.

Furthermore, spatial and most especially temporal resolutions are generally limited.

When considering these situations, it is apparent that in order to obtain the bathymetry required as input to study an eventually complex forward problem, it is possible to solve a simpler "inverse" problem first. That is, instead of using expensive techniques to collect bathymetric data it is possible to use alternate techniques to collect a different set of data, usually in the form of wave properties, and then previous knowledge of how wave properties relate to the bathymetry in order to infer bathymetry from it. This process, termed *depth inversion*, can potentially provide a powerful tool to estimate bathymetry, with the possible added benefit of improved spatial and temporal resolutions.

However, by doing this the focus has been shifted from the single problem of bathymetry measurement, to a new set of problems. First, it is required to select an appropriate transfer function that enables the estimation of bathymetry when another set of parameters has been measured. Secondly, the measurement technique of the selected target parameters should provide substantial advantages over traditional bathymetry collection, in terms of accuracy, resolution, costs, etc. Previous work in this field has shown encouraging results utilizing less expensive measurement techniques and this represents an active area of research.

Depth inversion methods have been classified in different ways. *Misra et al.* (2003) for instance distinguish between *frequency domain* inversions and *time domain* inversions. Frequency domain inversions utilize as input dense temporal sets of wave data to estimate wave parameters using Fourier analysis, whereas in time domain inversions data is coarser temporally. *Narayanan et al.* (2004) classify the inversions into *a priori* and *full* approaches. A priori methods rely on the assumption that wave properties and water depth can be related by means of a previously known relationship, usually in the form of a dispersion relationship. Full inversions use some version of the equations of motion, the Boussinesq equations for instance, to characterize the physics of the process of wave propagation and evolution, without assuming an explicit simpler relationship between wave properties and water depth. This classification can be considered ambiguous when we take into account that some a priori assumptions need to be made in order to select the equations to be used, therefore arguably all inversions methods can be considered as

a priori. In the following, we classify depth inversions by means of the nature of the data collection technique used.

We identify *field-based* inversions, although field data and laboratory data will be treated as the same, as long as the wave parameters are collected either in situ or remotely. This differs from *synthetic* inversions, when wave data is generated numerically to test the accuracy of the depth inversion algorithm over simulated bathymetries. Since data is generated numerically, typically this type of inversion assumes that the model used to create the data set is capable of explaining all of the relevant physical processes. Although this might not be exactly true, this assumption implies that the main goal of synthetic inversions is to test a particular inversion algorithm rather than the accuracy of the wave model used.

This review is organized as follows. First we review previous depth inversion works using field and synthetic based data. Typical errors observed are analyzed in detail in § 2.4 , and conclusions are presented in § 2.5

2.2 Field based inversions

Regarding field inversions, *Stockdon and Holman* (2000) mention that depth inversions were being performed using remotely sensed data as early as the 1950s, when time-elapsed aerial photography of the free surface was used to estimate the velocity of propagation of long crested waves, from which depth was estimated. The technique relies on the fact that wavelengths and phase speeds decrease as waves propagate into shallower water. If the fundamental frequency is known, depth can be estimated from a single image by comparison of the local wavelength with the deep water wavelength. If the frequency is unknown, then a sequence of images can be used instead. More recently this particular technique has been updated using newer sources of airborne imaging systems, such as infrared images (IR) (*Dugan et al.*, 1996), or the Airborne Remote Optical Spotlight System (AROSS, (e.g. *Dugan et al.*, 2001; *Piotrowski and Dugan*, 2002)). These studies rely on the usage of the general form of the linear dispersion relation

$$\sigma = \sqrt{gk \tanh(kh)} + \mathbf{U} \cdot \mathbf{k} \tag{2.1}$$

where $\sigma = 2\pi/T$ is the radian frequency, g is the gravitational acceleration, $\mathbf{k} = (k_x, k_y)$ is the wavenumber vector of magnitude k, and $\mathbf{U}$ is the water mean velocity vector. Data was collected in the form of a sequence of images of the free surface with footprints of the order of km^2, forming what its called data cubes. Analysis consisted of fast Fourier transforms (FFT) that yield 3-D power spectrum density maps (frequency-wavenumber coordinates). Although traditional Fourier analysis of free surface time series allows estimation of the wave amplitude, for remotely sensed dataset this is often not possible because the observed signal $I(f)$ is only a proxy of the true wave signal $W(f)$, and both can be related by

$$I(f) = M(f)W(f) \tag{2.2}$$

where $M(f)$ corresponds to the modulation transfer function (MTF) which describes the relationship between phases and amplitudes between the observed and the true signal. The nature of this function will depend on the mechanism by which waves are seen by a particular remote sensing technique, and this mechanism can vary across the field of view. Depth inversions based on remotely sensed data typically rely on phase-based MTFs, thus limiting of amplitude retrieval. For the case of airborne systems for instance, the magnitude of the resulting spectrum is affected by variation on the sky radiance observed by the camera system (*Dugan et al.*, 2001). However, the effect of sky radiance does not affect the location of the dispersion surface defined by $\sigma - k_x - k_y$ triads satisfying Eq. 2.1 . To estimate the location of this surface, 2-D frequency wavenumber slices are used instead, where a nonlinear least squares fit is used to determine the two free parameters $\mathbf{U}$ and h in Eq. 2.1 , with the capability to resolve for multiple frequencies (or wavenumbers) simultaneously. *Piotrowski and Dugan* (2002) reported errors of about 30% in depth estimation for the data set of *Dugan et al.* (1996), where the technique was affected by camera positioning and errors in the correct mapping of the images to world coordinates. *Dugan et al.* (2001) improved mapping and camera positioning,

and compared the retrieved tide corrected depths with in situ surveyed depths. Depth retrievals compared well with surveys between 4 m and 12 m depths, with root-mean-square (hereafter RMS) errors in the range of $\sim 5-13\%$, but with relative coarse spatial resolution ($O(50)$ m). In situ measured wave heights were in the range $H_s = 0.6-1.2m$, and nonlinear effects were not included in the analysis. Later, *Piotrowski and Dugan* (2002) also analyzed the data set of *Dugan et al.* (2001) to account for dependencies of the error on system and environmental parameters, focusing on sampling accuracy and dependency on the relative water depths kh. Since the analysis for this source of error is applicable to other studies as well, it will be reviewed in later sections of this study (see § 2.4).

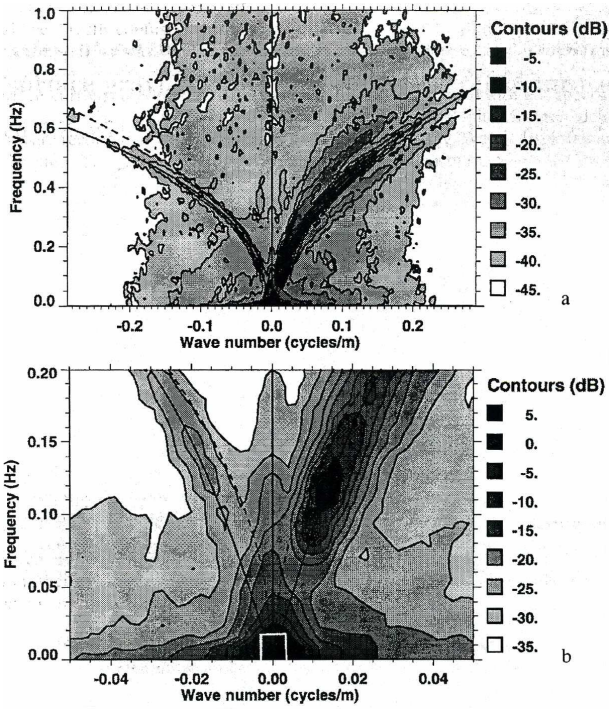

Fig. 2.1: Example of 3D frequency-wavenumber spectrum slice, showing cross-shore wavenumber. Solid line represents the theoretical dispersion relation (Eq. 2.1) and dashed the deep water value approximation. a) Full spectrum b)Close up of the low frequency and wavenumber portion (from *Dugan et al.*, 2001).

Similar data cubes can also be obtained using other remote sensing sources, like X-band marine radar (*Bell*, 1999; *Wolf and Bell*, 2001; *Trizna*, 2001). *Bell* (1999) suggested that Fourier analysis of these images in the wavenumber domain implies the assumption

of a spatially stationary process, that is, waves do not change significatively in length inside the sample window. This is not true for the rapidly changing shoaling waves, thus Fourier analysis returns averaged wave properties. To avoid this, *Bell* (1999) used a cross-correlation analysis of the time series from individual pixels with their surrounding pixels at a later time, in a similar way to Particle Image Velocimetry (PIV) analysis. Peaks in correlation are used to estimate the motion vector, from where wavenumbers can be estimated. Peak periods were obtained by spectral analysis of the time series, which in this particular study yield periods longer than those measured by an in situ buoy. Nevertheless, *Bell* (1999) commented that for relatively shallow water ($h < 10$ m) errors in period have little importance in the estimation of wave celerity, suggesting that it is more important to obtain accurate measurements of celerity than of wave period.

Significant wave heights were $H_s = 2$ m, and even though nonlinearity may affect the results, he used Eq. 2.1 with the assumption of no currents ($\mathbf{U} = 0$) to derive explicitly the depth as a function of the phase speed c and deep water conditions

$$h = \frac{L_o}{2\pi}\frac{c}{c_o}\tanh^{-1}\left(\frac{c}{c_o}\right) \tag{2.3}$$

$$c = L/T = \sigma/k \tag{2.4}$$

$$L_o = \frac{gT^2}{2\pi} \tag{2.5}$$

where the subscript o denote deep water conditions. No local in situ wave data was available, and only a crude estimate of the accuracy of the method was performed by comparing the tidal signal measured with that observed by the offshore buoy, showing good qualitative agreement. Possible sources of error were attributed to the use of the full wave signal in the analysis (i.e. without filtering or time windowing), causing smearing on the estimation of wavenumber. Therefore, it is hard to identify the exact frequency that corresponds to the celerity obtained, which introduces error in the estimation of the deep water parameters in Eq. 2.3 . In addition, even though the period has little influence in speed estimation in shallower water, it is expected that nonlinearities may cause departure from the linear dispersion causing depth overprediction.

Wolf and Bell (2001) used similar data sets from X-band radar at the same location to estimate wave properties from the images. Since no local bathymetry was available, they used the inversion technique to estimate the required bathymetry. Instead of using deep water conditions as in Eq. 2.3 , they solved Eq. 2.1 analytically in the absence of currents by using

$$h = \frac{1}{2k} \ln \left(\frac{gk + \sigma^2}{gk - \sigma^2} \right) \tag{2.6}$$

where k, σ were evaluated at the peak of the 3D frequency-wavenumber spectrum. Errors of about 25% were typical at 10 m true water depths, assumedly caused by coarse resolution in wavenumber and frequency estimates.

Dalrymple et al. (1998) analyzed the ability of two depth inversion methods. Although they used synthetically generated data, the methods studied can be safely applied to field data and for that reason are included in this section. The first method used the linear dispersion relation for the depth inversion. In this case, free surface maps were generated by the combined refraction/difraction model REF/DIF1 (*Kirby and Dalrymple*, 1994). A single image (2DH map of free surface) is analyzed by means of Hilbert transforms, which allows estimation of the phase over the image. Horizontal gradients of the phase yield the wavenumber vector field, which was used with a previously known (input) radian frequency to estimate depth using linear wave theory. The method was capable of accurately resolving two dimensional bathymetric features such as a conical island, and further runs were performed with the introduction of noise, wave period errors and nonlinear amplitude effects. The technique showed to be particularly sensitive to wave period errors, but performed well on intermediate to shallow waters.

Although not explicitly stated, it is apparent that wavenumber retrieval using this technique for irregular conditions would be affected by smearing and how to determine the wave period to be used is less clear, similar to what *Bell* (1999) observed. Therefore, *Dalrymple et al.* (1998) used a lag-correlation method for irregular waves instead. For this case, free surface maps were created using the fully nonlinear Boussinesq model of *Wei et al.* (1995). The data was analyzed in terms of auto and cross-correlations of the

free surface signal over subregions of the image assuming that the power density spectrum can be reconstructed from these. Auto and cross-correlations can be also obtained from the wavenumber spectrum and the dispersion relation based on an assumed depth. The inverted depth is obtained by minimizing the mismatch between measured and estimated auto and cross correlations. Agreement was found to be good, but small scale features were hard to detect due to smearing introduced in the analysis technique caused by window size and finite record lengths. Nonlinear effects were studied by amplification of the input wave height. The resulting depths were overpredicted in regions of large wave height due to amplitude dispersion that was not correctly interpreted by the linear dispersion relation.

During the last few years, remote sensing in the form of video has proven to be a useful tool to study the nearshore (see *Aarninkhof and Holman*, 1999, for an overview). Results from *Lippmann and Holman* (1991) showed that remote video signals are well correlated with progressive waves and phase speed can be inferred from these pixel intensity series. Consequently, *Stockdon and Holman* (2000) introduced a video technique for depth inversion by collecting pixel intensity time series at cross-shore arrays with a pixel footprint of 2.5 m. Hence, instead of using data cubes they used data planes (time-space maps) of pixel intensity, usually known as timestacks, from which wave properties could be inferred. Peak wave frequency was estimated using the averaged pixel intensity spectrum calculated over cross-shore pixel arrays. Cross-shore and longshore wavenumbers are estimated from timestacks by means of frequency domain Complex Empirical Orthogonal Functions (*CEOF*), allowing the determination of propagating signals at different frequencies. It was assumed that the first CEOF mode explains most of the variance associated with the incident wave field, and linear wave theory with no currents was used to estimate depths. Taking advantage of the continuous monitoring capabilities of the video method, data was collected hourly over a month at Duck, NC, leading to over 710,000 individual estimates of depth, which were screened, retaining data with onshore propagation, wavelengths satisfying $k < 0.9k_o$ and large CEOF amplitude. The remaining data set was tide corrected. Results showed an overall good agreement with in situ surveys of a beach profile with a single bar. Mean relative errors were on the order of

11% deeper than surveyed depths, meaning that measured speeds were larger than the speeds predicted by linear wave theory. This was especially significant in shallow water, where speeds departed from linear theory likely due to amplitude dispersion. In addition, depth errors were observed to increase near the onset of breaking region owing to a phase change in the imaging mechanism as waves begin to break, changing from specular reflection from the wave surface to diffuse reflection form the white foam associated with breaking turbulence. The long temporal extent of the data set also allowed them to evaluate the performance of the method under changing wave height conditions and it was observed that errors showed a tendency to increase with wave height. Suggested possible reasons were amplitude dispersion effects and/or poor coherence of short crested seas typical of large wave conditions. Since errors concentrated in shallow water, they compared the speed predicted by solitary wave theory and that predicted by the shallow water approximation. Results showed that overestimations of order γ (percent) can be associated with finite amplitude dispersion, where $\gamma = H/h$ in the saturated surf zone, with a typical value of $\gamma = 0.42$ (*Thornton and Guza*, 1982).

The same site was also studied by *Holland* (2001) using an extensive array of pressure sensors to collect wave data in an attempt to assess the accuracy of the inversions performed using linear wave theory and the possible effect of environmental parameters such as currents and wave heights. Wave and depth data from various experiments at Duck, NC was used in the analysis. The technique involved the estimation of the cross-shore wavenumber spectrum $k_x(f)$ from the cross-spectra between two adjacent sensors and an extension of the same technique to multiple sensors. Eq. 2.1 was used for the inversion in the range of frequencies coherent with sea swell, with posterior tidal correction. By grouping results in depth bins, results showed good agreement ($\pm 10\%$) in depths on the range 8-13 m, with an average bias of 3% and outliers associated with large wave height conditions ($H > 4$ m at 8 m depth). Error increased significantly in shallower regions up to 25% in the $h < 4$ m bin, where errors up to 50% were common. Analysis of the error suggested that it was consistent with amplitude dispersion effects as it correlated well with an offshore value of the significant wave height H_s, while no significant correlations were found for parameters such as peak period T_p, incidence angle θ or the surf similarity

parameter. *Holland* (2001) introduced an empirical correction to the speeds in the form a cnoidal wave equation

$$c(x) = \sqrt{g(h(x) + \alpha H_s)} \tag{2.7}$$

where α is a function of the Ursell number and H_s is the wave height. However, *Holland* (2001) only an offshore measured of H_s and looked for the best fit value for α when solving Eq. 2.7 with the measured phase speeds and true depths. Values of α= 0.42 and 0.48 where found, consistent with theoretical, Ursell-based values. After correcting the depth estimates using Eq. 2.7 , shallow water errors were reduced from 25% to 7%, within the range of accuracy of the deeper water observations.

Up to this point, the linear wave dispersion relation provided an easy to use transfer function between water depths and wave properties. Alternative formulations to the depth inversion problem have been made with alternate data sets obtained with some of the mentioned remote sensing techniques. Instead of using time series of instantaneous video or radar data, it is possible to use the average of the signal over timescales longer than the timescale of wave periods (several minutes instead of seconds). In these time-averaged images, modulations are averaged out and the resulting regions of high pixel intensity correlate well with areas of depth-induced breaking, such as sand bars. In this way, the time-averaged pixel intensity series can be associated with breaking related energy dissipation. Furthermore, previous work showed that the cross-shore location of the maximum of pixel intensity is well correlated with bar crest location, although with some shoreward bias (e.g. *van Enckevort and Ruessink*, 2001, 2003). On the other hand, wave evolution models have been developed to model wave decay in the surf zone with a good level of agreement by incorporating various formulations of wave dissipation (e.g. *Thornton and Guza*, 1983). In consequence, it is possible to use an iterative approach to estimate bathymetry by coupling the observed dissipation patterns and wave decay models. By starting with a beach profile estimate, wave dissipation D_c from a wave model can be obtained. This quantity can be compared with remotely sensed dissipation D_o. Mismatch between the two values is used to update the bathymetry until convergence is

achieved.

Aarninkhof et al. (2003) used this methodology with time averaged video images. The process involved two steps for each useful image. First, dissipation from the video signal is set to be proportional to the ratio E_r/c, where E_r is the roller energy and c is the phase speed. The quantification process requires special care for removal of persistent foam signal not related with breaking. In parallel, dissipation is computed from a numerical model and the two values compared. The second step is the minimization of the depth update by spatial redistribution of a sediment layer, where a sediment conservation condition inside the domain is imposed to improve numerical stability.

The technique was tested under field conditions to model beach evolution over a 12 month period, comparing results with in situ surveys that showed a multiple barred profile. Although the model is capable to predict bar migrations well, we focus here on results for individual profile estimation, to make it comparable with other studies presented here. Relative (RMS) errors for individual profiles where approximately 20-25 %, with a concentration of larger errors in shallower water. Typically bar troughs were underpredicted and bar crests were overpredicted, where overprediction is understood as the true water depth is smaller than the predicted value. Results for a sample profile where classified in cross-shore sections according to the topographic features present (bars and troughs), from where it was observed that bars were better predicted than troughs with a typical relative error of 10% or less, and RMS errors went up to 50% of overprediction in the inner surf zone.

Using X-band radar as the source of data, *Ruessink et al.* (2002) used a similar technique with emphasis in the cross-shore location of bars rather than accurate depth retrieval. Nevertheless, it shows the possibility of extending the technique to other remotely sensed sources of data.

In general, this approach requires information of offshore wave conditions (H_s, T_p) to drive the wave model, and a suite of parameters to be calibrated for the numerical model, dissipation quantification and bathymetry updating routines. Although this technique appears to be very useful for long timescale assessment of morphological change, the instantaneous depth prediction capabilities require improvement.

2.3 Synthetic data based inversions

Considering that amplitude dispersion effects appeared to be of importance, *Grilli* (1998) used a fully nonlinear potential flow (FNPF) numerical wave tank to simulate periodic, non-breaking waves. The model is very accurate and the main objective is to use the model outputs to perform depth inversions in the shoaling region, where both dispersive and amplitude effects are present. Therefore, phase speed is different from what is predicted by the linear dispersion relation and needs to be corrected. To account for this behavior, *Grilli* (1998) used empirical relations for a planar sloping beach by defining the ratio c/c_o as function of the observed wavenumber k, phase speed c, water depth h and the offshore steepness $k_o H_o$, where H_o is the offshore wave height. Hence, assuming that fields of c, H and two characteristic wave lengths defined as the distance between two consecutive crests (L_c) and two consecutive troughs (L_t, see Figure 2.2) are known from free surface spatial maps, depth h, period T and offshore wave height H_o can be obtained iteratively. This approach was termed DIA1. However, considering that wave height fields can be difficult to obtain from traditional remote sensing methods, a second approach (DIA2) was developed in terms of wave asymmetry, defined as the ratio of two characteristic wave lengths L_1 and L_2, where L_1 is the distance between a wave crest and its following trough, and L_2 is the distance between a wave crest and its preceding trough. Again, best fit empirical relations of asymmetry as function of the offshore steepness were calculated, and used as a corrector step in the calculations for h, T and H_o.

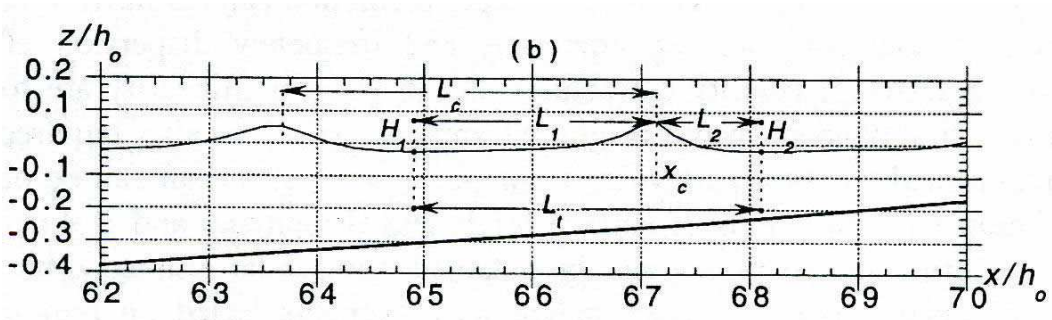

Fig. 2.2: Sketch from the shoaling wave and wave parameters used for the depth inversion algorithms (from *Grilli*, 1998).

Results for piecewise continuous beaches consisting of different planar slopes, showed very good results on the inversions (DIA1, $\sim (1\%)$), whereas simultaneous linear theory inversion relative errors went up to 50 %. Similar results were obtained for an equilibrium profile, indicating the possible use of the empirical relations obtained for planar beaches for this case. DIA2 provided slightly larger errors (up to $\sim (6\%)$), suggesting that detailed information of the wave height profile is not relevant provided that the offshore wave height estimate is accurate.

Grilli and Skourup (1998) tried to extend these algorithms for periodic waves shoaling over more complex bathymetries such as barred beaches. However, it was found that for large nonlinearity, the region of increasing depth shoreward of the bar causes wave decomposition, with the release of free harmonics causing modulation patterns on all the relevant signals (c, H, k), thus seriously limiting the use of the DIAs studied. An additional limitation of the DIAs used is that the empirical equations used were developed for one dimensional monochromatic wave conditions.

In order to test a depth inversion algorithm under what it is assumed to be the best possible remote sensing scenario, *Kennedy et al.* (2000b) created synthetic maps of free surface elevation and orbital velocities by using an updated version of the fully nonlinear Boussinesq model (*Kennedy et al.*, 2000a; *Chen et al.*, 2000) for 1D and 2D cases. Instead of solving a dispersion relation, they used an assimilation technique in which bathymetry is updated based on the mismatch between wave properties of the "measured" data (corresponding to a depth profile $h_m(x)$) to those obtained by the model driven by the measured data at $t = 0$ over an assumed bathymetry $h_t(x)$. The property under analysis was phase speed, obtained by cross-correlations of the free surface or orbital velocities data using spatial sub-domains. Depth updating relied on the fact that waves travel slower in shallower water, thus if the modeled speed is larger than the modeled speed at $t = t_o$, the local depth should be increased. This is achieved by the ratio

$$h_m = h_{t_o}(c_m/c_{t_o})^{\beta} \tag{2.8}$$

where the exponent $\beta = 4$ was selected in order to expand the method from shallow water

($\beta = 2$) to intermediate water without adding the requirement of accurate measurements of wavenumber. Furthermore, the explicit inclusion of the velocity field in the calculations allowed the estimation of mean current effects. Results showed RMS errors of $O(5\%)$ (regular waves) and $O(7\%)$ (irregular waves), with a tendency to increase in the region near wave breaking with a bias to overpredict the depth. The algorithm showed some sensitivity to the sub-domain size and selection of the snapshots to perform the cross-correlations. Nonlinear effects can not be evaluated because the same model was used in the simulation and inversion steps.

To avoid some of the problems observed by *Kennedy et al.* (2000b) when estimating phase speed using cross-correlations, *Misra et al.* (2003) used a least-squares approach over spatial sub-domains for one-dimensional cases. They extended the algorithm used by *Kennedy et al.* (2000b) by allowing the estimation of depths when either the free surface *or* the orbital velocities are known, and developed inversion algorithms for the linearized extended Boussinesq equations (based on *Nwogu* (1993)) and the fully nonlinear Boussinesq equations in order to estimate the effects of nonlinearity. In both cases, the equations of motion are used (mass and momentum) which can be written in terms of the phase speed c, the local water depth h, the free surface η and the velocity u. Measurements of c and an assumed bathymetry allows for computation of u (or η) when η (or u) is known. Since an estimate of the unknown variable can be obtained from each equation, the correction is based on the mismatch between the estimates

$$h_{\text{new}} = h_{\text{old}} \left(\frac{\sum_W |\eta_{\text{momentum}}|}{\sum_W |\eta_{\text{mass}}|} \right)^{\beta} \tag{2.9a}$$

$$h_{\text{new}} = h_{\text{old}} \left(\frac{\sum_W |u_{\text{mass}}|}{\sum_W |u_{\text{momentum}}|} \right)^{\beta} \tag{2.9b}$$

where W is a window centered about the point under evaluation, and β is a shallowness parameter similar to the one used by *Kennedy et al.* (2000b). When free surface data is available, results showed that inclusion of nonlinear effects reduced depth estimation errors by 10% for simple bathymetries. When a bar system with regular waves is considered, the presence of harmonics shoreward of the bar hinders the estimation of phase

speed, resulting in shallower depth predictions (about 50 % error in depth), consistent with the findings of *Grilli* (1998). Random waves shoaling over a simple bathymetry consisting of a parabolic section led to RMS errors of about 14%, the error being correlated with the broadness of the input spectrum and dispersive effects in deep water. Inclusion of currents leads to a Doppler shift in phase speed that is interpreted as depth changes when the free surface is the input data set. This is improved by using an inversion algorithm based on velocities, but the applicability of this algorithm is more limited considering the difficulties of obtaining such data set for actual situations.

2.4 Observed sources of error

Based on the review of previous work, it is possible to group qualitatively the sources of error in three groups: First, it is possible to identify the sensitivity of equations used to different wave conditions (characterized by the wave parameters) assuming that the chosen equations fully describe all the relevant physical processes. These errors are thus related with the functional form of the equation. Secondly, we can group reported errors related with the inaccuracy of the previous assumption that the chosen equations are capable of accounting for the relevant wave processes, hence this error is related with the physics of the wave evolution process. In a third group, we find errors induced by the different implementations and their limitations based on measurement systems (e.g. rectification and registration for video based systems), analysis techniques used and others (e.g., the sensitivity and accuracy of Fourier based methods on record length and stationarity). We will focus on the two first groups because of their generality.

As can be seen, most of the previous work relies in the usage of the linear dispersion relation and typically the presence of currents is not considered. This equation relates depth h with the input parameters wavenumber k and wave period T (or radian frequency σ). Using variational calculus, it is possible to write the error on the retrieved depth when the input parameters deviate from their true values as (*Dalrymple et al.*, 1998; *Piotrowski and Dugan*, 2002)

$$\frac{\delta h}{h} = F(kh)\frac{\delta \sigma}{\sigma} - G(kh)\frac{\delta k}{k} \tag{2.10}$$

$$= 2\left(\frac{\sinh 2kh}{2kh}\right)\frac{\delta \sigma}{\sigma} - \left(1 + \left(\frac{\sinh 2kh}{2kh}\right)\right)\frac{\delta k}{k}$$

which shows a clear dependence on the dispersion parameter kh, as can be seen on Figure 2.3(a) . Thus any perturbation δk ($\delta\sigma$) on the estimate of k (σ), causes an error at least twice as large, with increasing magnitude as depths get deeper or waves get shorter.

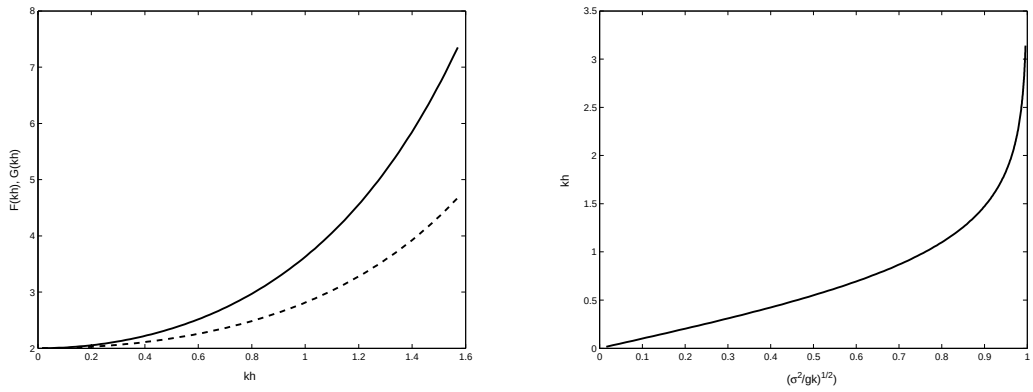

(a) (b)

Fig. 2.3: Linear dispersion relation. a) Error amplification functions $F(kh)$ (solid) and $G(kh)$ (dashed), (Eq. 2.10); b) Depth dependency as a function of frequency, following *Kennedy et al.* (2000b)

In addition, as relative depths become larger, wave properties (k, σ) are less dependent on bathymetry, or it can be said that depth determination is less accurate for any given $k - \sigma$ pair provided kh is relatively large ($kh > 1.5$) as can be seen on Figure 2.3(b) , where $\tan kh$ is plotted as a function of $\sigma/\sqrt{gk}$.

These two conditions put some constraints on the depth inversion capabilities for intermediate to deep water, even if the assumption of linearity is true everywhere. Therefore, some screening of the data appears to be necessary as to perform inversions over wave conditions that allow more accurate results (e.g. *Stockdon and Holman*, 2000).

Various wave phenomena can be related with the second group of errors, for instance

the Doppler shift caused by the presence of currents in cases where they were assumed to be negligible. The effect on speed varies whether there is a favorable or opposite current. Either way, the speed will diverge from the theoretical value predicted using Eq. 2.1 with the absence of currents.

Also important appears to be departures from linearity that can not be explained by the linear dispersion relation, as mentioned previously. Two significant processes can be distinguished to occur in different regions. First, the increase in nonlinear amplitude dispersion as the waves shoal before breaking while frequency dispersion is still present. *Stockdon and Holman* (2000) considered that this effect can explain part of the errors observed before breaking. *Grilli* (1998) calculated the error on the estimation of the phase speed when wave height effects are included up to third order Stokes theory

$$\frac{c_H}{c_L} = 1 + (kH)^2 \Psi_1(kh) \tag{2.11a}$$

$$\Psi_1(kh) = \frac{8 + \cosh 4kh - 2\tanh^2 kh}{32 \sinh^4 kh} \tag{2.11b}$$

$$kH = k_o H_o \Psi_2(kh) \tag{2.11c}$$

$$\Psi_2(kh) = (\tanh(kh))^{-3/2} \left(1 + \frac{2kh}{\sinh skh}\right)^{-1/2} \tag{2.11d}$$

where c_L and c_H are the linear and height corrected phase speeds, respectively. A measure of nonlinearity is given by the wave steepness parameter kH. Figure 2.4 shows the ratio between the wave height corrected phase speed c_H and the linear case c_L. Although error seems to be quite large when water is very shallow or waves are very nonlinear, this can be attributed to the functional form of the Ψ functions, which were derived for waves of permanent symmetric shape. Nevertheless, even for small steepness, errors of order 10% on the speed estimate can be common, therefore affecting the depth estimates if linear theory is used, doubling the error in depth (e.g. Eq. 2.10). However, as *Stockdon and Holman* (2000) suggested this effect can be minimized if different wave conditions (H_o, T_p)

are selected to perform the inversion, which is a suitable option in field measurements with long data records.

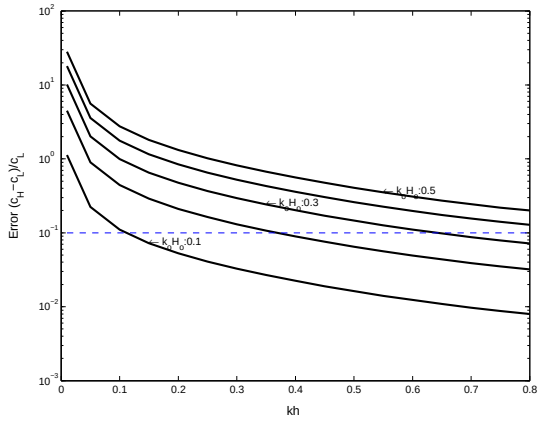

Fig. 2.4: Estimation of the error due to nonlinear effects on phase speed as a function of the offshore wave steepness $k_o H_o$ and kh, following Eq. 2.11 (*Grilli*, 1998).

The second region affected by nonlinear effects is the surf zone, especially shallow water. Waves in this region tend to be saw-tooth shaped, with a frequency non dispersive behavior, and linear wave theory collapses to the simple form

$$c_L = \sqrt{gh} \tag{2.12}$$

from where it is apparent that depth inversion is straightforward. However, it is in this region where most of the previous work found significant errors, usually with an overprediction of depths (e.g. *Stockdon and Holman*, 2000; *Holland*, 2001). For the depths to be overpredicted, the measured phase speed must be larger than the theoretical phase speed given by Eq. 2.12 evaluated with the true depth. This situation will occur in the inner surf zone regardless of the wave conditions, thus can not be avoided and an alternative formulation for c has to be used instead.

Similar departures from the linear dispersion have been observed on field measurements. *Suhayda and Pettigrew* (1977) photographed an array of wave poles placed between the swash zone and the breaking point. By tracking the passage of the crest at each pole, they found that outside the surf zone, wave phase speed was in agreement

with the linear approximation given by Eq. 2.12 , but inside the surf zone the measured speed deviated ±20% from the linear value.

Thornton and Guza (1982) obtained measurements of phase and celerity spectrum in the surf zone, and compared their results with linear wave theory, showing that waves in the surf zone can show frequency non dispersiveness and amplitude dispersion, which could be related to the speed of propagation of a solitary wave

$$c = \sqrt{g(h+H)} = \sqrt{gh(1+H/h)} = \sqrt{gh}\sqrt{1+\gamma} \tag{2.13}$$

which appears to be valid for a single characteristic frequency and the saturated breaker parameter had a value $\gamma = 0.42$. *Thornton and Guza* (1982) did not, however, discard other possible situations that can explain the differences, such as the effect of low frequency waves that can change the instantaneous value of h over several wave periods. *Lippmann and Holman* (1991) and *Puleo et al.* (2003) found good agreement between phase speed estimates using remotely sensed observations and values predicted using Eq. 2.13 , the latter using $\gamma = 0.5$. *Inman et al.* (1971) using an array of wave sensors measured phase speeds which were bounded by the linear and solitary limits, although a bias toward the solitary limit was apparent. γ was calculated for each individual case as H/h, with values in the range $0.33 \leq \gamma \leq 1.1$.

Shallow water theories also provide different values for the speed of propagation of a solitary wave, for instance

$$c = \left(1 + \frac{1}{2}\frac{H}{h}\right)\sqrt{gh} \tag{2.14}$$

$$c = \sqrt{g(h+\eta)} \tag{2.15}$$

$$c = \sqrt{g\left[h + H\frac{1}{m}\left(-3 + 2 - 3\frac{E}{K}\right)\right]} \tag{2.16}$$

Eq. 2.14 corresponds to the solitary solution to a Korteweg de Vries formulation, which is slightly different from Eq. 2.13 , corresponding to a Boussinesq formulation (*Dingemans*, 1997). Eq. 2.15 corresponds to the solution obtained when the Nonlinear

Shallow Water Equations (NSWE) are described in their characteristic form. It can be noticed that in this case, the perturbation is attributed to the instantaneous free surface η, thus the crest of the wave would travel faster than the troughs, steepening the front of the wave (*Musumeci et al.*, 2003). Eq. 2.16 corresponds to the general expression for a cnoidal wave (*Mei*, 1989), which *Holland* (2001) wrote in the simplified form presented on Eq. 2.7 .

Madsen et al. (1997) suggests the use of $c = 1.3\sqrt{gh}$ for regular waves, stressing that this approximation is not suitable for irregular cases. This corresponds to the approximation to the propagation speed of a breaking wave (bore), characterized by a moving hydraulic jump

$$c = \sqrt{gh\left(1 + \frac{3}{2}\frac{H}{h} + \frac{1}{2}\left(\frac{H}{h}\right)^2\right)} \tag{2.17}$$

from where the value 1.3 is obtained when $\gamma = H/h = 0.42$.

These experimental results, along with the aforementioned findings of *Holland* (2001) for α, show that there is a relatively wide range of possible values to be used for the different parameters (γ, α), but emphasize the need to include nonlinear effects when inverting depths in shallow water.

2.5 Conclusions

It can be seen that depth inversion is an active area of research, based on the potential that different remote sensing techniques have to provide a suitable set of data. However, most of the previous work based on field lacks the inclusion of nonlinear effects basically due to limitations to the current state of sensing techniques. At the same time, inversions based on synthetic data showed that inclusion of nonlinear effects can lead to significant improvements on the depth retrieval.

It is our interest then, to test the possible improvements of using a nonlinear inversion scheme with real data. Considering the limitations of remote sensing, an alternative hybrid data set is used on which the extra parameters required are numerically simulated and coupled with laboratory observations of the traditional parameters.

3. METHODOLOGY

3.1 Introduction

As mentioned before, to date nonlinear inversions have not been tested with real data basically because they require highly resolved wave information, typically in the form of free surface time series or at least wave height profiles. There exist a set of different techniques to be used in obtaining this data set. The most obvious appears to be the deployment of dense arrays of measuring devices (e.g. *Holland*, 2001), but this methodology has the disadvantage that it is very expensive, and the possibility of obtaining an adequate synoptic coverage in the horizontal plane is limited; although they generally provide high temporal resolution.

Remote sensing techniques solve part of the previous problem, in the sense that they can provide synoptic data over large regions with relatively high resolution. These techniques include remote sensing in the form of video time series (eg. *Stockdon and Holman*, 2000), airborne optical imaging (eg. *Dugan et al.*, 2001) or radar time series (eg. *Bell*, 1999). However, these techniques only provide a proxy for the free surface elevation time series. Airborne optical images and video for instance, register the intensity signal emitted by the light reflecting on the sea surface, either by specular reflection from the non breaking part of the waves, or diffuse reflection from the white foam produced for wave breaking. *Lippmann and Holman* (1991) compared time series of video pixel intensity and collocated pressure data and showed that both time series were coherent over the incident band. Although important wave properties such as wave period and phase speed can be retrieved from this data set, video is not able to provide estimates of wave height, thus making it an incomplete tool for nonlinear depth inversions.

Radar registers the scattering of incident radar energy from sea surface perturbations such as ripples and waves. The retrieved images correspond to maps of reflected radar energy intensity in a similar way to the video pixel intensity images, thus allowing esti-

mation of the same wave properties. However, radar based techniques offer the potential for estimation of wave heights based on empirical methods. For instance, *Wolf and Bell* (2001) derivated an empirical transfer function to relate X-band radar spectra to wave spectra. Further improvements allowed estimation of significant wave heights (e.g. *Nieto Borge and Guedes Soares*, 2000; *Izquierdo et al.*, 2005) and rough estimates of free surface time series (*Dankert and Rosenthal*, 2004). It is apparent that the potential for obtaining free surface elevation maps from these systems exists, thus making them suitable for nonlinear depth inversions.

However, the current status of the remote sensing methods is such that they can only provide a fraction of the required information to perform nonlinear depth inversions. In order to test nonlinear inversions with field data, wave properties associated with nonlinearity ($\eta(x, y, t)$ or $H(x, y, t)$) must be sought using other techniques. One feasible alternative is the use of numerical models, which can provide good estimates of wave height profiles. There are various models available, for instance the phase-averaged models of *Thornton and Guza* (1983), the REF/DIF1 model (*Kirby and Dalrymple*, 1994), which solves combined refraction and diffraction by solving the Mild Slope Equation; or phase resolving models based on the nonlinear Boussinesq equations (e.g. *Schäffer et al.*, 1993; *Wei et al.*, 1995; *Lynnet et al.*, 2002, and their extensions). Whichever the choice, it must be stressed that the model output is to be considered as a proxy of the possible output of future remote sensing systems.

By doing this, we have selected a hybrid data set in the sense that our wave parameters will be obtained by a combination of remote sensing techniques and numerical modeling. The next consideration is the choice of a suitable transfer function to be used for depth estimation that includes nonlinear effects.

3.1.1 Composite dispersion relation

Considering that most depth inversion methods used with remotely sensed data were based on the usage of the linear dispersion relation, it would be interesting to find a suitable relationship between wave parameters and water depth that also includes nonlinear effects in some degree. *Holland* (2001) suggested that the composite dispersion relation

of *Kirby and Dalrymple* (1986) might be appropriate.

The composite model is essentially an empirical combination of different theories depending upon the relative water depth. Intermediate to deep water waves are modeled using a third order Stokes theory, resulting from a series expansion of wave parameters under the assumption of smallness of the parameter $\epsilon = k|A|$, where k is the wavenumber and $A = H/2$ is the wave amplitude. Considering that this formulation has limitations in shallow water, the empirical model of *Hedges* (1976) is used in this region instead. The asymptotic behavior of the two is matched by the following dispersion relation (*Kirby and Dalrymple*, 1986)

$$\sigma^2 = gk(1 + f_1\epsilon^2 D)\tanh(kh + f_2\epsilon) \tag{3.1}$$

where

$$f_1(kh) = \tanh^5(kh) \tag{3.2a}$$

$$f_2(kh) = \left(\frac{kh}{\sinh(kh)}\right)^4 \tag{3.2b}$$

where σ is the radian frequency, g the gravitational acceleration and D is obtained from Stokes theory as

$$D = \frac{\cosh(4kh) + 8 - 2\tanh^2(kh)}{8\sinh^4(kh)} \tag{3.3}$$

The asymptotes are

$$\sigma^2 = gk\tanh(k(h + |A|)) \tag{3.4}$$

for shallow water (*Hedges*, 1976) and

$$\sigma^2 = gk(1 + f_1\epsilon^2 D)\tanh(kh) \tag{3.5}$$

for Stokes theory. The resulting monochromatic dispersion model collapses to the linear

dispersion for zero amplitude ($A = 0$), thus allowing direct comparison when estimating the benefits of adding nonlinearity to the depth inversion algorithm.

3.1.2 Depth inversion algorithm

Hence, by using the composite dispersion model given by Eq. 3.1 , it is possible to obtain depth h estimates once wave properties (σ, k and A) have been measured. The algorithm is similar to previous inversion methods based on the linear dispersion equation.

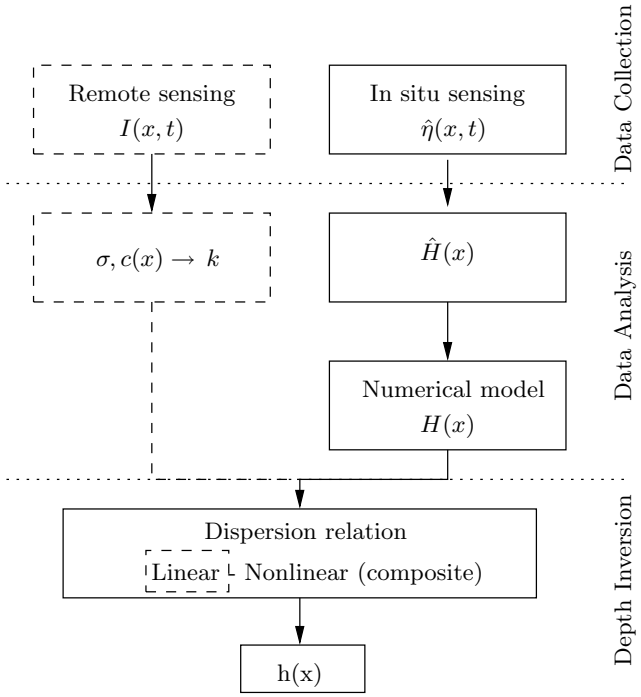

Fig. 3.1: Inversion algorithm flowchart. Dashed lines represent steps taken for linear inversions and solid lines represent additional steps taken for nonlinear inversion. For the present implementation, $\hat{()}$ denotes data with low spatial resolution.

Figure 3.1 sketch the inversion algorithm, where three steps are considered. The first step is collection of the hybrid data set. Remote sensing considers the use of video imagery. Since this technique can only provide phase speed and wave period information (thus wavenumber), additional measurements are taken in situ in the form of free surface time series at discrete locations. The second step is thus the estimation of the wave parameters σ, k, c and $\hat{H}$. The time series of free surface elevation are used to numerically simulate a more densely sampled wave height profile. The third step correspond to the

estimation of the bathymetric profile using the composite dispersion model and the linear dispersion model for comparison purposes. Unlike the linear dispersion, solution of the composite dispersion relation (Eq. 3.1) is not explicit and requires an iterative process.

3.2 Experimental Set-up.

The experiments were conducted in the Large Wave Flume (hereafter LWF) at O.H. Hindsdale Wave Research Laboratory, Oregon State University. This is a 104 m long (90 m useable), 3.7 m wide and 4.6 m deep wave channel, with a programmable flap-type wavemaker with active wave absorption capabilities. The one dimensional bathymetric profile can be adjusted by fixing concrete slabs to the sidewalls. For the present study, a concrete barred beach was deployed, as shown in Figure 3.2 , which was designed to approximate the bar geometry for the average profile observed on October 11, 1994, of the DUCK94 field experiment. More details of the bathymetric profile deployment can be found on *Scott et al.* (2004).

The beach profile was surveyed and a right hand coordinate system was set up and termed for future reference as WRLCS (Wave Research Lab Coordinate System). The origin of this system is located at the toe of the wavemaker, in the centerline of the tank. Thus the positive x axis is pointing onshore, and z pointing upward. It must be noted, however, that water depths are measured relative to the still water level, which was set at z =4.27 m (14 ft) and care was taken to maintain this level for all the runs, by refilling the tank.

The LWF also has an array of threaded inserts on each wall designed for instrument mounting and slabs positioning. These are located in horizontal pairs 8 in (0.20 m) apart and spanning the entire tank depth, 0.3 m apart vertically. They are also used as an auxiliary reference system, as 21 vertical pair arrays are located in each wall 3.66 m. (12 ft) apart. Each one of these bays is numbered starting from bay 1 at the onshore end of the tank (see Figure 3.2). This auxiliary system will be used in the remainder of this text for referencing instrument positioning.

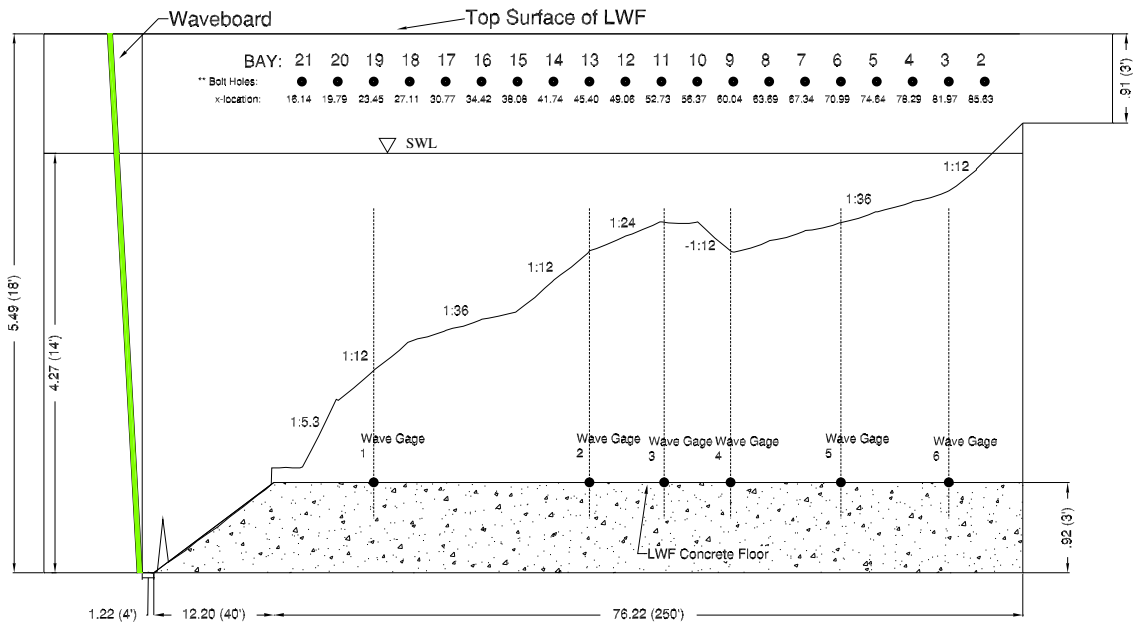

Fig. 3.2: Surveyed beach profile at the LWF.

3.2.1 In situ data collection.

Six resistance-type wave gages sampling at 50 Hz were used to measure free surface elevation. These were installed on the east wall of the tank, at cross-shore locations $x =$ 23.45, 45.40, 52.73, 60.04, 70.99 and 84.97 m (bays 19, 13, 11, 9, 6 and 3, respectively). The location for these was selected with the following criteria: Bay 19 corresponds to the toe of the barred beach and is located in the middle of the offshoremost section of the beach, with a local beach slope of $m = 1/12$, thus wave records at this location will be used later to drive the numerical model. Bays 13 and 11 corresponds to the bar, where breaking is expected, and bays 9, 6 and 3 are selected to record wave evolution shoreward of the bar, on a gently sloping beach ($m = 1/36$).

The resulting data series will be used to drive and calibrate the numerical model. For the case of REF/DIF1 , the calibration is based on the wave height profile.

3.2.2 Remote sensing data collection

Remote sensing data was collected with an ARGUS III video system developed by the Coastal Imaging Lab, COAS, OSU. Three ARGUS cameras were mounted on the roof of the laboratory's control room aiming at different sections of the wave flume, with the camera field of view spanning offshore from bay 14 (x=41.74 m) to the dry beach. Single snapshots of the each camera's field of view (FOV) can be seen in Figure 3.3 .

(a) Cam.3 (b) Cam.2 (c) Cam.1

Fig. 3.3: ARGUS cameras snapshots with low angle sun.

The collected data consisted of three different pixel arrays defined in laboratory coordinates (WRLCS), spanning from $x = 41.65$ m to $x = 100$ m at longshore coordinates $y = -1.2$, 0 and 0.6 m. The pixel selection is made by a coordinate transformation of each pixel from image space to world space in a process termed *rectification* (*Holland et al.*, 1997). This process, implicitly assumes that all pixels lie on the same world horizontal plane, which in this case was selected to be at the still water level (z=4.27 m = 14 ft). Figure 3.4 shows a rectified image of the tank with the approximate location of each pixel array. The world location of the target point of each pixel is assumed to remain invariant throughout the collection process.

Video data were sampled at 10 Hz, with a total of 5836 pixels (cross-shore pixel footprint of 1 cm) , thus covering 58.3 m of tank, from x=41.7 m to x=100 m. The resulting data set is a time-space map (timestack) of pixel intensity for each camera. Data collection considered also a time stamping of each frame, recorded in epoch format. Analysis of the time stamped series showed deviations of order $\pm 1 * 10^{-3}$ s from the target sampling rate of $\Delta t = 0.1$ s. It is assumed then that the sampling rate is exactly 10 Hz.

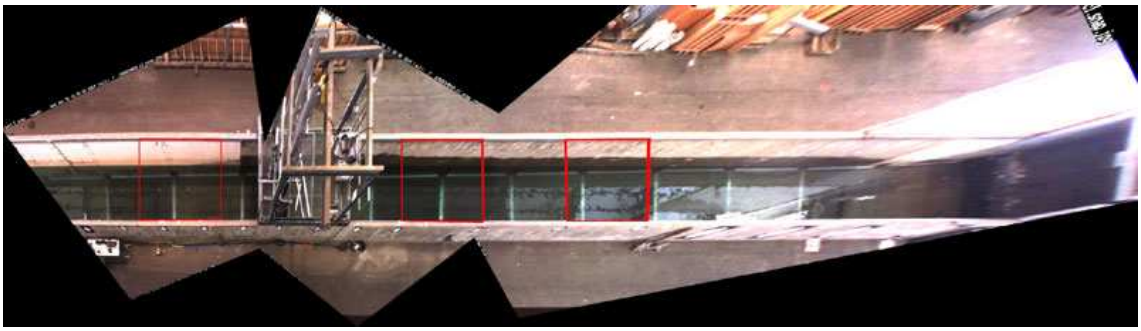

Fig. 3.4: ARGUS field of view and pixel arrays.

As mentioned previously, video registers the intensity of the light signal reflected or emitted by surfaces. It is our interest then that the wave signal can be clearly distinguishable from other signals on the water surface. As can be seen from the snapshot images, this is not necessary the case for this laboratory set up. Although the laboratory building is relatively dim and requires permanent artificial illumination, it also has windows along its perimeter, allowing for daylight to come in at low angles. This type of illumination does not present an immediate problem, because most of the time the water surface is in the shadow of the tank walls. When the sun is at a low angle, direct sunlight entered through the windows creating brightly illuminated regions (see Figure 3.3(b)), causing high contrast between the tank surroundings and the water surface. This is in fact an advantage, because in this case the main transfer function will be related with from scattered light in the turbulent breaking region and foam patches. (see Figure 3.3(c) and Figure 3.3(b)). However, for large waves the crest of the wave can be reached by direct sunlight, causing a bright region related with specular reflection. It is not clear that the observed wave signature will correspond to the same wave point all the time, thus eventually causing spurious speed estimates. It appears to be preferably then to have diffuse light sources because light would be eventually better distributed over the camera FOV.

This kind of illumination conditions are achieved when the sun is at high angles, as diffuse light comes in through the windows as ambient radiance. However, due to the discrete positioning of the light sources (windows) this causes a problem when the geometric configuration between the camera, the free surface and the window is such that

the incident light is effectively reflected by the water surface, resulting in a very bright region in the camera FOV. This problem can be observed on Figure 3.5(c) , where a bright region is present near the shoreline. Although this reflecting surface is unlikely to change position significatively during an individual run, the resultant low contrast between the wave signal and the stationary reflective spot makes harder to separate them. In order to minimize this problem, a fabric curtain was set up to block this incident ambient light as much as possible and making the passing light more diffuse. The curtain set up can be seen on Figure 3.5(c) and its effect on Figure 3.4 .

(a) Cam.3 (b) Cam.2 (c) Cam.1

Fig. 3.5: ARGUS cameras snapshots with low angle sun.

In addition to the aforementioned problems, other signals were also recorded by the cameras. For instance, the aluminum plates deployed on the slab junctions were clearly visible due to the water lack of turbidity (e.g. Figure 3.5(b)). It is of interest then to attempt to minimize the effect of these spurious signals on the measurements.

The collected data set consists of nine timestacks for each run, (3 pixel arrays x 3 cameras) . Each set of timestacks is merged as to provide a single image for the entire field of view. However, this process is not straightforward due to differences in gain between cameras. To solve this problem, it is necessary to address two different situations.

First we need to consider the background intensity at each location. As mentioned before, this is related with the visible signature of elements other than the waves, and it was assumed that this signature is stationary for each run. This include sources like the region of very intense reflection from ambient light near the shoreline, or the bright aluminum plates deployed between concrete slabs. In order to remove those signals, each run considered one minute of record with still water conditions. Analysis of the pixel

intensity time series showed that there was little variance during this period, and hence it was assumed this level as background level. Consequently, the mean value of pixel intensity during still water time was removed from the whole series. This process is repeated for each timestack individually. An example of the results of this procedure can be seen on Figure 3.6 for the onshore looking camera.

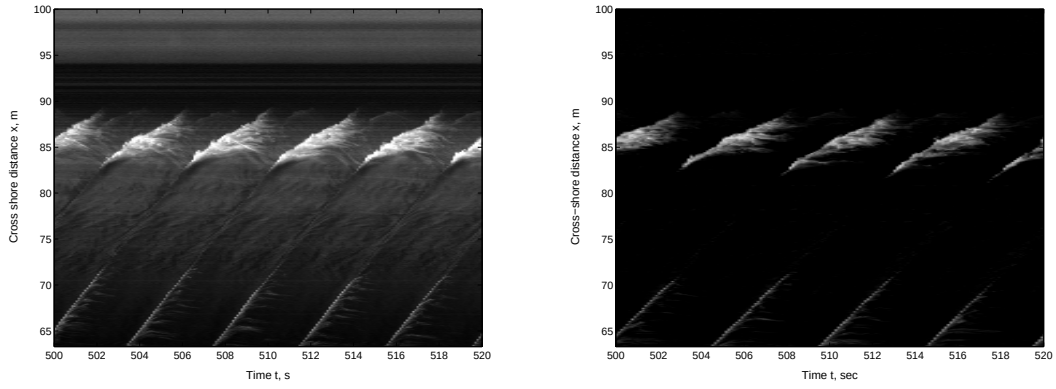

(a) (b)

Fig. 3.6: Example timestacks for Camera 1, $H = 0.40$ m, $T = 4.0$ s. a) Raw timestack, including background signal, b) Mean removed timestack

Secondly, we must consider that each camera is adjusted as to maximize the observed intensity range. This effect can lead to differences in the overall sensitivity *between* cameras, causing an abrupt change in the pixel intensity signal at the boundary between cameras when the images are merged. Since some of the analysis techniques rely on analysis of the spatial evolution of the intensity signal, it is necessary to remove this effect. To do so, we assume that the pixel intensity time series $I(x,t)$ at the boundary $x = x_0$ must be almost the same, considering that non-duplication of locations is explicit on the pixel arrays. Therefore, we can impose the condition that the mean of the two time series is the same at the boundary

$$\bar{I}(x_0^+) = \bar{I}(x_0^-) \tag{3.6}$$

where x_o^+ and x_0^- are taken from different cameras. Since typically these mean values are not the same, we can scale the series as to force the equality in Eq. 3.6 . Application

of the scaling has several alternatives. The first one would be to scale down the signal with larger mean value, but this approach has the problem that this would cause loss of breaking related information useful to estimate wave properties. The opposite method, scaling up the image with smaller mean presents initially the problem of saturation of the image, since the pixel intensity signal has to be in the range $I(x,t) = 0 - 255$. However, considering that the still water level mean values have been removed and the signal has already been reduced, it is expected that this approach effectively enhance the relevant wave signal and is preferred. The next consideration is how to apply the correcting factor to the remainder of the image. The simplest consideration of a uniform scaling was applied here. Alternative considerations like a linear spatial variation of the scaling ratio were not tested. The correction is then

$$I_{\text{new}}(x,t) = \frac{\bar{I}(x_0^-)}{\bar{I}(x_0^+)} I(x,t) \tag{3.7}$$

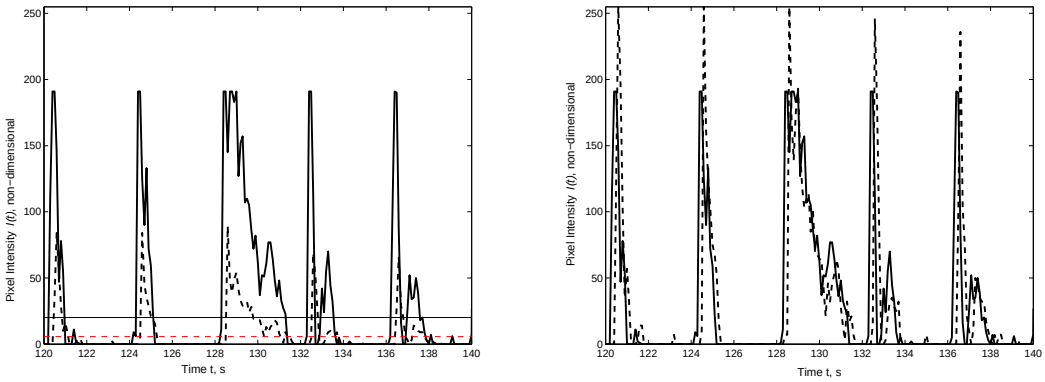

(a) (b)

Fig. 3.7: Example of timestack scaling and merging procedure. a) Raw data sets and mean pixel intensities $\bar{I}$ at the interface between cameras 2 (solid) and 3 (dashed), $x = 63.3$ m b) Modified pixel intensity signal for camera 3 (dashed), showing good correlation with the signal of camera 2 (solid).

Analysis of the cameras showed in general that the region with stronger wave related pixel intensities is over the bar, where typically waves are breaking for all the cases studied. This is on the field of view of camera 2, therefore, this camera is selected as the reference camera and the intensity signals on cameras 1 and 3 are scaled up as to satisfy

Eq. 3.6 . Typically, camera 3 (pointing offshore) has very little breaking information, which is enhanced by this method. On its part, camera 1 (pointing shoreward) is the camera that is more affected by non wave related signals, and the still water mean removal consequently reduced the original intensity range. It is expected that this method would restore in part the wave related signal.

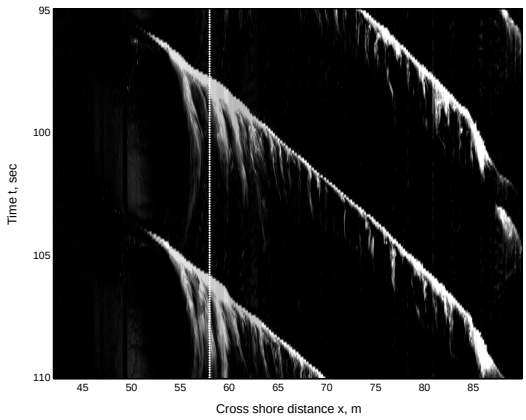

Fig. 3.8: Example of merged timestack, $H = 0.40$ m, $T = 8.0$ s. Vertical line denotes a transect at $x - 58$ m.

Figure 3.8 shows the resulting timestack for wave condition 5, where it can be seen that no abrupt transitions are present. It is also noticeable the clear signature of the breaking wave as it propagates and traces of foam being left behind describing orbital motion between $x = 55$ m and $x = 65$ m.

3.2.3 Other reference data sets

In addition, other reference data sets were also taken at bays 11, 9, 6 and 3. Video data were taken using a Sony Handycam camera mounted on a tripod during 45 s. These video records and snapshots are used as reference material only, in particular allowing the analysis of the breaking characteristics at each location.

3.2.4 Wave conditions.

A total of 10 wave conditions were used in this experiment, including 6 regular and 4 irregular waves conditions. The range of periods for the regular waves was 2.7 s to 8.0 s.

Regular waves were run for 7 minutes in order to allow the passage of at least 50 waves.

Table 3.1: Regular wave conditions

Wave Case	T, s	H_*, m	μ_*	δ_*	L_o, m	H_o, m	ε_o	**Breaker Type**
1	2.7	0.6	2.40	0.14	11.38	0.62	0.18	spilling
2	4.0	0.6	1.26	0.14	24.98	0.66	0.26	spilling
3	5.0	0.5	0.94	0.12	39.03	0.54	0.35	spilling
4	6.0	0.5	0.75	0.12	56.21	0.52	0.43	spilling-plunging
5	8.0	0.4	0.54	0.09	99.92	0.38	0.68	plunging
6	4.0	0.4	1.26	0.09	24.98	0.44	0.31	spilling

Table 3.1 and Table 3.2 show the tested wave conditions, where the subscript $*$ denotes values at the wavemaker ($x = 0$, $h_* = 4.27$ m) and the subscript o denotes theoretical deep water conditions. $\mu = kh$ is the dispersion parameter, $\delta = H/2h = A/h$ is the nonlinearity parameter and $\varepsilon_o = m/\sqrt{(H_o/L_o)}$ is the Iribarren number, calculated with a representative slope $m = 1/24$.

The peak periods for the irregular cases consist of a subset of the periods for the regular wave tests. A TMA spectrum was generated using a peak enhancement factor of $\gamma = 20$ to provide narrow banded spectra. However, it was noticed that the beach profile prevented the use of wave heights larger than $H_{rms} = 0.65$m, due to waves overtopping the wave gages. As a consequence, the maximum possible wave heights were selected according to the irregular cases and used in the corresponding regular case. Even though *Scott et al.* (2004) suggested that stable measurements of undertow can be obtained for 20 minute averages, the final run length for the random waves was selected to be 15 minutes, as it was assumed that offshore driven currents will not play a significant role on the depth inversion. For instance, for wave case 4.0, measured undertow over the bar represented 14% of the linear phase speed.

Table 3.2: Random wave conditions

Wave Case	T, s	H_*, m
7	4.0	0.6
8	5.0	0.5
9	2.7	0.6
10	4.0	0.4

An estimate of the abruptness of slope changes for the profile can be used by estimating the fractional change of depth over a wavelength, defined as (e.g. *Raubenheimer et al.*, 1996)

$$\frac{\Delta h}{h} \propto \frac{\beta}{kh} \tag{3.8}$$

where β is the local slope, k the wavenumber and h the local water depth. This parameter ranged between β/kh=0 to 0.5 for the proposed conditions, results within the range observed by *Raubenheimer et al.* (1996) for real beaches.

3.3 Data Analysis

3.3.1 Phase speed c

Typically the phase speed c, that is, the speed of propagation of a wave of constant form, is the most important wave parameter to be measured to perform depth inversion.

Field estimation of the phase speed c requires as input free surface elevation time series, or at least some proven proxy of it. Under the assumption of no change of shape, c can be determined by the trajectory of a specific point in the wave, for instance $\eta = 0$ (*Svendsen et al.*, 1978) or the crest $\eta = \eta_{\max}$ (*Suhayda and Pettigrew*, 1977). Within the scope of depth inversion, *Holland* (2001) used bottom mounted pressure sensors to measure the free surface and later cross-spectral methods to estimate phase speeds. Cross-spectra has been used also with video measurements of the free surface (e.g. *Lippmann and Holman*, 1991), or with the use of X-band marine radar (*Bell*, 1999). Video has also been used in conjunction of other speed estimation methods, like frequency domain Complex Empirical Orthogonal Functions (CEOF) (*Stockdon and Holman*, 2000).

In the following we present different techniques that were evaluated for the estimation of the phase speed from video timestacks.

Front and crest tracking methods

This method is based on the estimation of the local slope of the trajectory described by characteristic point of the wave. The trajectory can be expressed as $t = t(x)$ or $x = x(t)$.

Either case, the local speed phase speed is defined as

$$c(x,t) = \frac{dx}{dt} = \frac{\Delta x}{\Delta t} \tag{3.9}$$

for the discretely sampled trajectory. The implicit assumption is that the wave is not changing shape during the lapse Δt, and therefore the characteristic point to be tracked remains the same relative to the wave. Under this assumption of constant shape, the method is general enough to be applied to any point on the wave. However, two characteristic points are selected in the present study. First, the crest of the wave, assumed to be the point where the free surface is a local maximum, and second the front of the wave, which will be considered as the zero up crossing about the mean free surface level.

For measurements of the actual free surface, identification of these two points is fairly straightforward. However, for the case of pixel intensity series some assumptions have to be made, considering that these series represent only a proxy of the free surface. We analyze the front tracking case first.

Looking at Figure 3.8 , it is possible to distinguish clearly an abrupt change in the pixel intensity values as the breaking wave passes through certain location (change from dark to bright in the image). This abrupt change can be identified also on the pixel intensity time series shown in Figure 3.9 . This suggests initially that identification of the wave front is related with the identification of the time t when the pixel intensity shows a large positive gradient locally. However, the pixel intensity time series may present other instances where this gradient is large but are not related with the wave front. For example, Figure 3.9 shows the pixel intensity time series at $x = 58$ m, denoted by the white line on Figure 3.8 . Three different instants with large positive intensity gradients can be observed, the first two ($t = 97.5, 106$ s) are associated with the wave front, but the third is associated with the passage of a patch of foam moving offshore ($t = 107$ s). Thus, this technique is required to be coupled with another criterion for appropriate selection of the front.

The method considered the selection of individual waves (or breaking events) using MATLAB built-in subroutines for edge detection, based on the zero-up crossings from

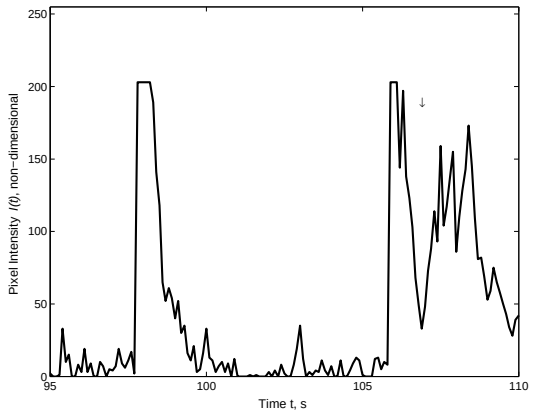

Fig. 3.9: Pixel intensity time series at $x = 58$ m, $T = 8.0$ s, $H = 0.40$ m. The arrow indicates the beginning of the foam related signal.

the mean removed timestack . Once each breaking event is isolated, the front of the wave will be characterized in the functional form $t = t(x)$, corresponding to the time t where the breaking event (wave) first occurs at each location x, thus removing temporal multiplicity for each location. This process is shown graphically on Figure 3.10 .

The process is repeated for all breaking events, and the results are averaged in time, yielding to $c(x)$. Alternatively, a similar procedure can be applied to a phase averaged timestack, but it was found that calculating for individual events and then averaging yield more stable results. In a similar way, *Madsen et al.* (1997) found that the accuracy of this method is limited, yielding noisy solutions. In the present case, it is expected that noise can be reduced by averaging over a large number of waves, plus the application of a low pass filter in the form of spatial running averages.

Regarding crest tracking, the definition of the crest is less obvious, in the sense that the maxima of the pixel intensity series are related with portions of the wave that emitted a strong signal, but the phase relationship between this point and the true wave peak is uncertain. In particular, analysis of the time series shows that the breaking signal can saturate the camera ($I = 255$) for relatively long periods of time ($O(1)$ s). In addition, local maxima are also present due to the persisting foam signal. Nevertheless, *Lippmann and Holman* (1991) compared the cross spectra between a pixel time series and a collocated pressure sensors showing that intensity time series can be considered to describe

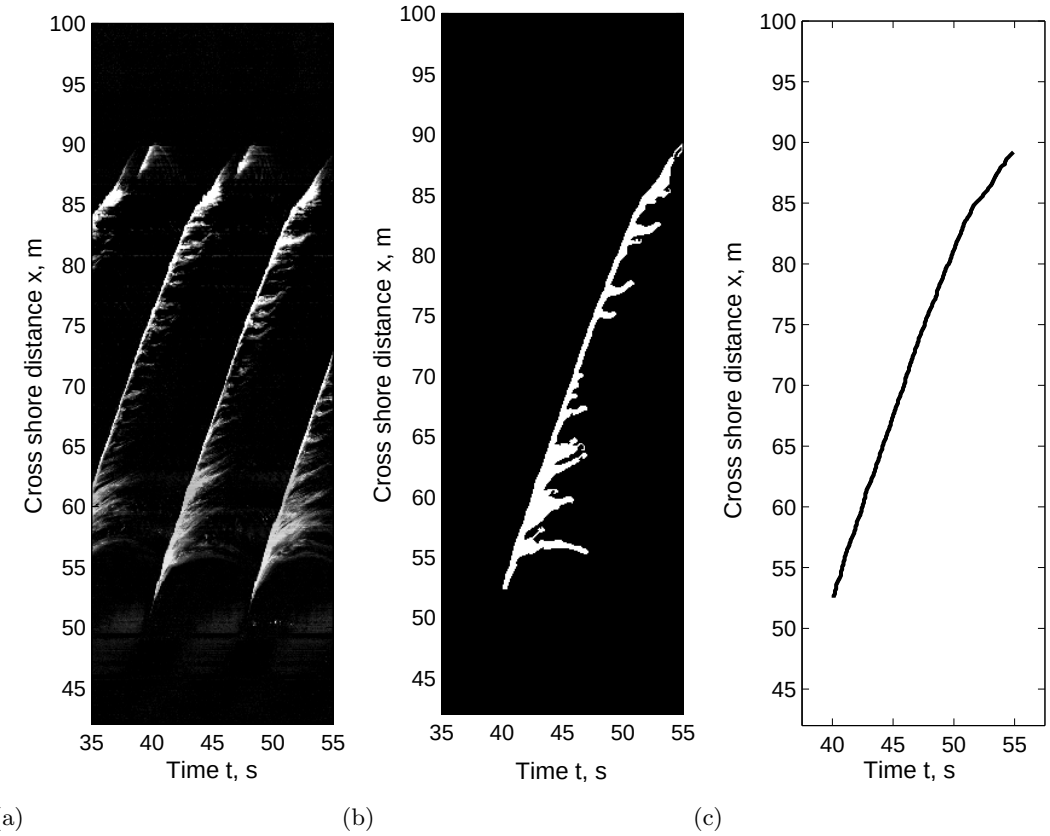

Fig. 3.10: Front selection and tracking procedure. a) Original timestack b)Binary image showing an isolated wave c)Wave front trajectory $t = t(x)$.

well the progression of breaking waves, with good correlation between wave crests and peaks on the intensity signal. A similar technique would require accurate synchronization between the two data collection systems, something that was not achieved for the present experiments.

However, assuming that pixel intensity correctly describes the propagation of the crest, it is possible to estimate the location of the pixel maxima by applying a low passing filter in the form of a spatial running average with a 61 points double sided window. This procedure reduces saturation, allowing estimation of the location of the maxima.

Since it is possible to have multiple waves breaking on the spatial domain at the same time, it is required to scan the timestack in time and space. For the spatial scan, windows of about 5.8 m long (583 pixels cross-shore) are used. As a result, two sets of (x, t) pairs

of the maxima location from each scan are obtained. The intersection between the two sets yield the crest location trajectory, a single valued function of space $t = t(x)$.

Complex Empirical Orthogonal Functions (CEOF)

Empirical Orthogonal Analysis (EOFs) and its complex extension (CEOF) are capable of identifying recurring patterns of variability in large data sets. The method allows the simultaneous characterization of different variables, spatial scales or frequencies explaining the variability present. In addition, it may have some advantages over cross-spectral analysis when the dominant frequencies and spatial scales are unknown (*Horel*, 1984). These methods have shown to be useful in identifying standing and traveling waves in geophysical data sets (e.g. *Wallace and Dickinson*, 1972b; *Kisthawal et al.*, 2001).

Consider a set of time series of a given variable (say, free surface elevation η) taken at M locations with N realizations at intervals Δt. In general, it is possible to express each of these time series as superposition of different modes of variability

$$\eta_m(t_n) = \sum_{i=1}^{M} a_i(t_n) F_i(x_m) \tag{3.10}$$

where $a_i(t_n)$ is an amplitude time series associated to the $i-th$ mode, which weights the spatial function $F_i(x_m)$ corresponding to the $i-th$ mode evaluated at location m. The goal of the method is to find a complete basis of functions $\mathbf{F} = \{F_i, i = 1, .., M\}$ that will describe in the most efficient way the input time series. It is important to note that this basis will have as many functions as measurement locations, M.

So far, this definition is general enough to be applied to several sets of functions, such as Fourier trigonometric functions for example, in which case the F_i functions are sines and cosines. However, the additional property of zero mean value for the cross product of the amplitude time series can be imposed, that is (*Wallace and Dickinson*, 1972a)

$$\langle a_j a_i \rangle = \delta_{jk} \lambda_i \tag{3.11}$$

where $\langle\rangle$ denotes an ensemble average, δ_{ij} is the Kronecker Delta and λ_i is the mean square value of the time series a_i. This condition defines a unique set $\mathbf{F}$ of functions

statistically uncorrelated, termed *Empirical Orthogonal Functions*. It can be shown that λ_i correspond to the eigenvalues of the matrix equation

$$(\mathbf{D} - \lambda\mathbf{I})\mathbf{F} = \mathbf{0} \tag{3.12}$$

where $D_{jl} = \langle \eta_j \eta_l \rangle$ is the covariance matrix. Since $\mathbf{D}$ is symmetric and positive definite, the eigenvalues λ_i are all real positive values. $\mathbf{F}$ is the MxM matrix with the associated eigenvectors, each column being one mode explaining uncorrelated variability of the time series set. How much of the total variance is explained by each mode, or relative importance of the mode, can be determined by normalizing the eigenvalues

$$P_i = \frac{\lambda_i}{\sum_{j=1}^{M} \lambda_j} \tag{3.13}$$

However, this specific approach is capable of detecting standing oscillations, in which case propagating oscillations are manifested as the superposition of two modes explaining a similar fraction of the total variance ($P_j \sim P_k$) and showing a phase difference, but its detection can be complicated when more than one propagating signal are present. In an attempt to extend this technique to detect propagating oscillations, alternative methods using frequency domain EOF and time domain CEOF using complex representations of the original time series have been developed. When comparing the two, *Horel* (1984) suggests that time domain CEOF might allow detecting propagating signals spread over a range of frequencies and for that reason we attempt it first.

In order to obtain these propagating features, the data is augmented in a way that phase information can be retained for later detection. To do this, each data series $\eta_m(t_n)$ can be extended into its corresponding *analytic signal*

$$z_m(t_n) = \eta_m(t_n) + iH(\eta_m(t_n)) \tag{3.14}$$

where H denotes the Hilbert transform of the original data set. By doing this, our data set is extended to a complex variable containing the original data set in its real part and the imaginary part containing the original data set unaltered in amplitude but all the

phases shifted by $-\pi/2$. This data set can be analyzed in similar fashion as described above for real time series, but in this case the resulting amplitude time series $a_i(t_n)$ and EOFs $F_i(m)$ are both complex. λ_i are positive and real since the covariance matrix $D_{jl} = \left\langle z_j^* z_l \right\rangle$ is Hermitian. It is possible to reconstruct the complex time series in terms of amplitudes and phases (*Merryfield and Guza*, 1990)

$$\begin{aligned} z_m(t_n) &= \sum_{i=1}^{M} a_i(t_n) F_i(x_m) \\ &= \sum_{i=1}^{M} A_i^a(t_n) \exp^{i\phi_i(t_n)} A_i^F(x_m) \exp^{i\theta_i(x_m)}, \end{aligned} \tag{3.15}$$

where the spatial and temporal amplitudes can be defined as

$$A_i^F(x_m) = [F_i^*(x_m) F_i(x_m)]^{1/2} \tag{3.16a}$$

$$A_i^a(t_n) = [a_i^*(t_n) a_i(t_n)]^{1/2} \tag{3.16b}$$

and the spatial and temporal phases are given by

$$\theta_i(x_m) = \arctan\left(\frac{\mathrm{Im}(F_i(x_m))}{\mathrm{Re}(F_i(x_m))}\right) \tag{3.17a}$$

$$\phi_i(t_n) = \arctan\left(\frac{\mathrm{Im}(a_i(t_n))}{\mathrm{Re}(a_i(t_n))}\right) \tag{3.17b}$$

Wavenumber, frequency and phase speed can be obtained from these variables as

$$k_i(x_m) = -\frac{d\theta_i(x_m)}{dx} \tag{3.18a}$$

$$\sigma_i(t_n) = -\frac{d\phi_i(t_n)}{dt} \tag{3.18b}$$

$$c_i(x_m, t_n) = \frac{\sigma_i(t_n)}{k_i(x_m)} \tag{3.18c}$$

Even though the phase speed is an explicit function of space and time, it may be

averaged in time, allowing the estimation of spatial variation of c.

As mentioned before, CEOF analysis can be performed either in time or frequency domains. For the present work, only the time domain procedure has been tested, however *Stockdon and Holman* (2000) performed frequency domain CEOF to perform their depth inversion algorithm. This approach assumes that all the relevant information is concentrated in the incident band and determination of the cross-spectral matrix is performed over this band only. However, in our case, wave patterns associated with nonlinear effects and harmonic frequencies might be of importance and therefore we can not discard that information beforehand.

Cross-spectral methods

This method is based on the estimation of the time lag between two consecutive spatial realizations of the same process, in this case in the form of two closely spaced time series. We can assume that between these two locations, the initial signal $y(t)$ is affected by a time delay process that can be expressed in the following form: (*Bendat and Piersol*, 1986)

$$z(t) = \alpha y_1(t - \tau_0) + n(t) \tag{3.19}$$

where $y(t)$ and $n(t)$ are uncorrelated, α is an amplification factor, that in the case of sea waves can be a function of space associated with shoaling processes and/or wave decay and $n(t)$ is a perturbation signal accounting for wave shape differences.

The cross covariance of the two processes is defined as (*Bendat and Piersol*, 1986):

$$R_{yz}(\tau) = E[y(t)z(t + \tau)] \tag{3.20}$$

where $E[]$ denotes the expected value. We define the lag of maximum correlation as $\tau = \tau_0$. Under the assumption of no correlation between y and n, it can be proved that the cross covariance between the processes $y(t)$ and $z(t)$ at a certain delay τ is related with the autovariance of the original process by

$$R_{yz}(\tau) = \alpha R_{yy}(\tau - \tau_0) \tag{3.21}$$

Using this relation and the definition of the power density spectrum, it is possible to relate the two sided spectrum with the cross spectrum by

$$\begin{aligned} S_{yz}(f) &= \int_{-\infty}^{\infty} R_{yz}(\tau) \exp^{-i2\pi f\tau}\, d\tau \\ &= \alpha S_{yy}(f) \exp^{-i2\pi f\tau_0} \end{aligned} \tag{3.22}$$

Thus, the cross spectrum corresponds to the amplified autospectrum of the original process $y(t)$ shifted by τ_0. Hence τ_0 represents the mean travel time for the wave between sensors, and it can be expressed as $\tau_0 = k/\sigma\Delta x$. Although this change in phase can also be related to changes in wavenumber k , if we assume that the two measuring locations are close enough for the water depth to be considered constant, wavenumber will remain constant and the phase shift will be directly related with Δx only.

We can rewrite

$$2\pi f\tau_0 = \phi(f) \tag{3.23}$$

and the phase spectrum $\phi(f)$ can be estimated from the co-spectrum and quad-spectrum by

$$\phi(f) = \arctan\left(\frac{Qu(f)}{Co(f)}\right) \tag{3.24}$$

Hence, the wavenumber and phase speed can be estimated as

$$k(f) = \frac{\phi(f)}{\Delta x} \tag{3.25}$$

$$c(f) = \frac{\sigma(f)}{k(f)} = \frac{2\pi f}{k(f)} \tag{3.26}$$

Allowing us to estimate the phase speed at each frequency. However, care must be taken that the two time series are related at any frequency under study, and this is

achieved by computing the coherence γ

$$\gamma^2 = \frac{Co(f)^2 + Qu(f)^2}{C_{11}(f)^2 C_{22}(f)^2} \tag{3.27}$$

where $Co(f), Qu(f)$ are the *co-spectrum* and *quad-spectrum*, the real and imaginary parts of the cross-spectrum respctively, and $C_{ii}(f)$ are the auto spectra. This method has been widely used, including remotely sensed estimates of depth (*Holland*, 2001) and velocity (*Curtis et al.*, 2002). They also used an extension of the method proposed by *Herbers et al.* (1995) for spatially dense arrays of sensors that was not tested in this study.

This method allows computation of the complete phase speed spectrum for each pair of sensors, but we focus on the peak frequency. Hence, the analysis is performed obtaining the phase lag only at the peak frequency f_p, which has to be calculated beforehand. Since resolution of the method is proportional to the run length, $\Delta f = (N\Delta t)^{-1}$, eventually linear interpolation of the phase ramp is required to obtain the phase at peak frequency.

3.3.2 Frequency and wavenumber

Radian frequency σ can be obtained from the pixel intensity time series by using a spectral analysis of the pixel intensity time series, where it is assumed that the frequency of the peak correspond to the incident wave period T_p. The method can be applied to a single cross-shore location and the result is valid throughout the domain. Wavenumber k can be obtained from the combined measured parameters c and σ by $k = \sigma/c$. Since c is a function of space, so will be k. Alternatively, as pointed out before, CEOF analysis provides the spatial wavenumber and temporal radian frequency explicitly for each of the modes detected, as defined in Eq. 3.18 . These two methods were tested on this work.

3.3.3 Wave heights

Wave height profiles are estimated from the in situ wave gage data series. Considering that each also contains data from still water, each series is processed in order to remove the still water and ramping up signals. The reduced time series is trimmed in order to have an integer number of waves by means of a zero-up crossing routine. An example of

the procedure is shown in Figure 3.11

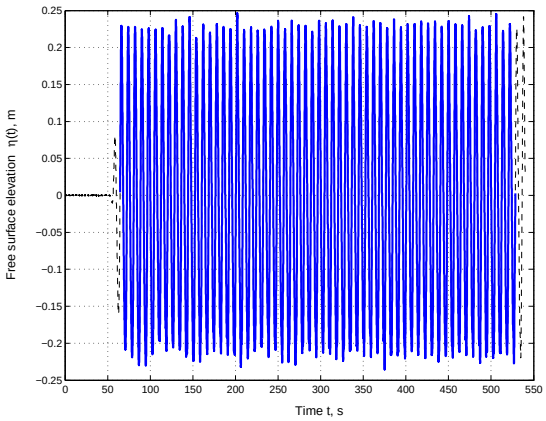

Fig. 3.11: Example free surface time series at Bay 19, $T = 8$ s, $H = 0.40$ m, showing original time series (dashed) reduced time series including 58 waves (solid).

Individual wave heights are calculated as the crest-trough vertical distance. The wave height array is sorted in descending order and significant wave height is calculated as the mean value of the upper one third of the record

$$H_s = \frac{3}{N} \sum_{i=2N/3}^{N} H_i \tag{3.28}$$

This process is carried out for all the in situ wave gages, yielding a wave height profile consisting of six cross shore points.

3.3.4 Numerical model

In order to obtain more densely sampled wave amplitude profiles, the combined refraction/difraction model REF/DIF1 (*Kirby and Dalrymple*, 1994) is used. This model solves the wave height profile for monochromatic waves solving the parabolic mild slope equation. Furthermore, the use of this model is consistent with the use of the composite dispersion equation, as it includes the option to explicitly use the composite dispersion to estimate the phase speed and wavenumber of the shoaling waves, thus nonlinearity is included to some degree.

Model calibration is based on the wave height profile obtained from the six in situ

gages. Instead of focusing the calibration process on the usual program switches, attention is put on some internal constants implemented in the numerical model.

The numerical domain consisted of a longshore uniform bathymetric grid, with $\Delta x =$ 0.1 m and $\Delta y = 0.073$ m, with total $m = 852$ x $n = 50$ (cross shore x longshore) points. The cross shore extent of the domain is smaller than the actual bathymetry, because locations offshore of Bay 19 ($x = 23.45$ m) are not used. A cross section of the bathymetric profile can be seen on Figure 3.12 . Two flat sections not consistent with the actual bathymetry can be noticed, one at each end. The model is driven by wave heights measured at the offshore wave gage (Bay 19, x=23.45 m), thus waves inside the domain are unaffected by the presence of the flat offshore section . The onshore flat section is created internally by the program wherever the actual bathymetry is dry (negative depths) evaluated at still water conditions. The model creates a thin film of depth of $h = 1$ mm to damp out waves at the shoreline boundary (*Kirby and Dalrymple*, 1994).

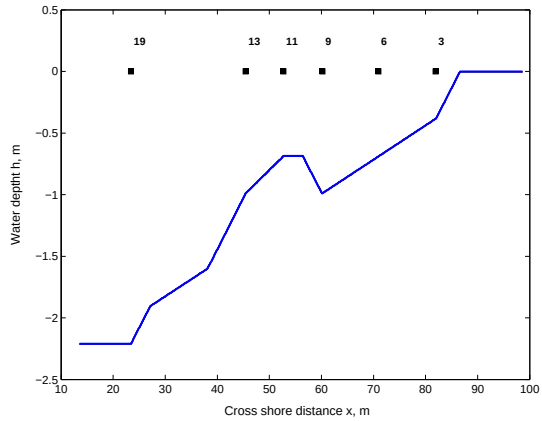

Fig. 3.12: Bathymetric profile for REF/DIF1 simulations . Squares indicate actual wave gage positions.

Friction effects and currents were turned off for all the cases, and the lateral boundaries were considered as closed. One relevant switch was to enable the use of the composite dispersion model of *Kirby and Dalrymple* (1986) in the model, to make results consistent with the expected nonlinear behavior of waves.

The model was initially driven by the measured wave amplitude at the offshoremost location and the incident period. However, since agreement was in general less than

satisfactory by using these switches only, internal empirical constants where modified. In particular all constants related with the breaking model used, corresponding to the model of *Dally et al.* (1985). This breaking model is implemented in REF/DIF1 by means of an energy dissipation factor w, with units time^{-1} (*Kirby and Dalrymple*, 1994)

$$w = \frac{KC_g(1-(\gamma h/H)^2}{h} \tag{3.29}$$

where h is the local water depth, H is the wave height, C_g is the group speed. K is a constant related with the amount of dissipation with a typical value of $K = 0.17$. γ on its part is related with cessation of breaking, under the assumption that for a flat beach, entering breaking waves will continue breaking until they reach a stable wave height described by $H = \gamma h$. The typical value for this constant is $\gamma = 0.4$. An additional parameter is Γ, that turns on breaking when $H/h \leq \Gamma$. Typically Γ follows the saturated breaking criterion of $\Gamma = 0.78$.

Modification of these constants allow us to improve the fitting with observed results. For instance, increasing the value of Γ allows for retarding the onset of breaking, thus enabling the modeled waves to shoal more.On the other hand, decreasing the value of γ allows for continuous wave breaking, a feature observed for some of the tested conditions.

3.4 Summary

In summary, in order to test the benefits of using a nonlinear dispersion equation for depth inversion, a set of experiments were designed.

Data collection considered two methods that combined provide an hybrid data set. Actual wave data was measured by means of a remote sensing technique (video) and in situ wave gages. The latter set is used for calibration of a numerical model as to provide a dense spatial profile of wave height.

Data analysis considers the use of different techniques to retrieve wave properties (wave period, wave phase speed, wavenumbers and wave heights), in an attempt to find the most accurate to be used on the depth inversion algorithm.

4. **RESULTS**

4.1 Introduction

Results of the depth inversion technique applied to the experimental data collected are presented in this chapter. Although data collection considered ten wave conditions, the usable set for application of the hybrid technique consists of only of 5 cases. This selection is based on the lack of an observable signature of the waves on the video system for some cases. As pointed out before, waves can be seen by the camera by means of two light reflection mechanisms (specular or diffuse). Poor lighting conditions meant waves were visible mainly due to diffuse reflection associated with breaking. As mentioned before, wave gage overtopping prevented using large wave heights for the irregular cases, and consequently only a fraction of the waves broke. Figure 4.1 shows the resulting timestack for the onshore looking camera for one of the irregular cases, where it can be seen the lack of wave related signal for relatively long periods of time, hindering the estimation of the wave periods and phase speeds. Therefore, irregular cases where only large waves are recognizable had to be discarded.

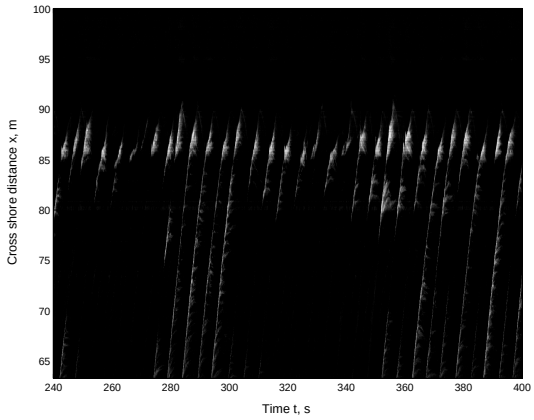

Fig. 4.1: Timestack corresponding to Camera 1 for an irregular wave case, where only large waves can be identified. Case 3, T_p=5.0 s, $H = 0.50$ m.

In consequence, in the following results are presented for the conditions presented on Table 4.1 .

Table 4.1: Summary of usable wave conditions

Wave Case	T, s	$H*$, m
1	2.7	0.6
2	4.0	0.6
3	5.0	0.5
4	6.0	0.5
5	8.0	0.4
6	4.0	0.4

This chapter is organized as follows. First, results for estimation of wave parameters using different techniques are presented, and the best set is selected to be used for depth inversion. Secondly, results from the depth inversion using linear and nonlinear models are presented and analyzed. Finally, an analysis of the possible sources of errors is presented.

4.2 Estimation of the wave height profile

Discretely sampled wave height profiles were obtained from the in situ data collection. In order to obtain more densely sample profiles, the numerical model REF/DIF1 is used. To drive the model, an offshore condition is provided in the form of the incident wave period and the measured wave height at the offshore gage.

Calibration is based on the observed wave height profiles $\hat{H}(x)$ measured next to the east wall of the tank and a sequence of snapshots taken with the handycam camera at bays where wave gages were present. These sets of snapshots allowed visual estimation of the breaking characteristics of each individual wave, which were relevant for the calibration process. A sample series of those snapshots can be seen on Figure 4.3

The calibration procedure was as follows. Based on the observed wave height profile, the parameters γ, K and Γ are modified as to match the maximum wave height. In addition, the wave height to water depth ratio H/h can be computed in order to estimate the occurrence of breaking at each location. This ratio is compared with the behavior

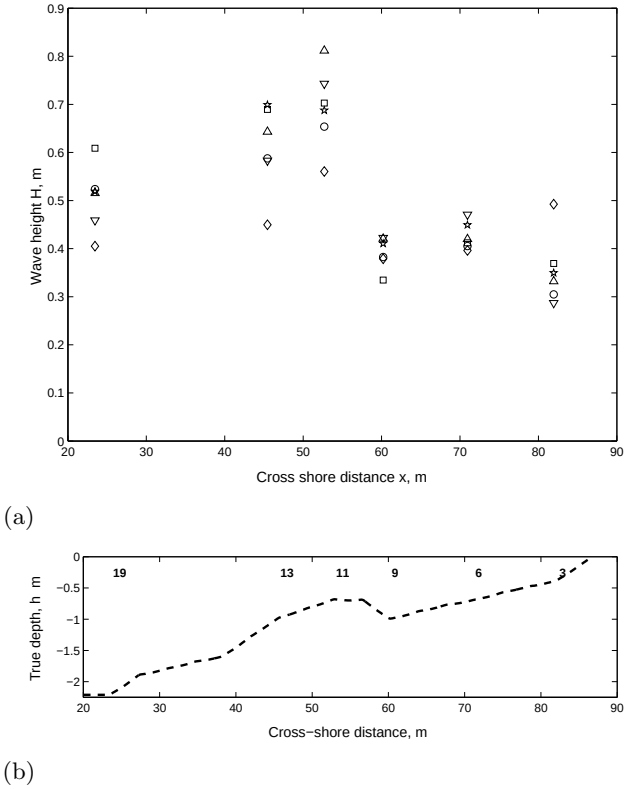

(a)

(b)

Fig. 4.2: Measured wave height profiles $\hat{H(x)}$, all cases. Case 1 (circles), Case 2 (squares), Case 3 (triangles), Case 4 (stars), Case 5 (triangles down), Case 6 (diamonds)

observed on the snapshot series and the parameters updated in an iterative process until agreement is found. It was found that it was difficult to simulate the maximum wave height, apparently due to limited shoaling on the model. However, overall good agreement for wave heights shoreward of the bar trough (Bays 09, 06 and 03) was possible to obtain by modifying the aforementioned breaking parameters.

In an attempt to improve agreement for the maximum wave height without affecting agreement in the shallower areas where nonlinear effects are expected to be important, the offshore wave height condition was relaxed and allowed to differ from the observed value. New values of the offshore wave height were tested in a trial-error scheme, where estimation of the best fit was purely qualitative.

Table 4.2 shows the final set of parameters used for calibration. It can be seen that the parameters governing cessation of breaking and the overall dissipation K showed little

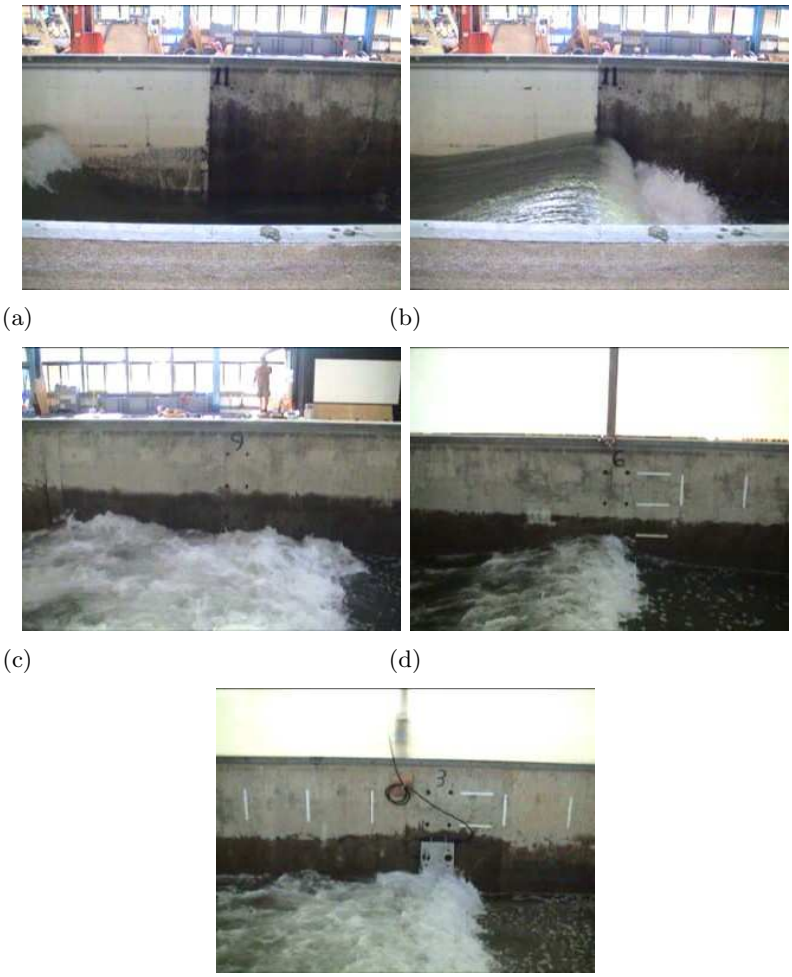

Fig. 4.3: Lateral snapshots of a regular breaking wave (Case 5, $T = 8.0$ s, $H = 0.40$ m a) Plunging point b) Bay 11, $x = 52.73$ m c) Bay 09, $x = 60.04$ m d) Bay 06, $x = 70.99$ m e) Bay 03, $x = 81.97$ m

Table 4.2: REF/DIF1 final parameter set

Wave Case	γ	K	Γ
1	0.40	0.155	0.90
2	0.40	0.155	0.90
3	0.48	0.145	1.15
4	0.41	0.150	0.98
5	0.41	0.170	1.07
6	0.42	0.150	0.85

variation when compared with the proposed values of $\gamma = 0.40$ and $K = 0.17$ (*Dally et al.*, 1985). However, it was found that small variations on K can change significatively the

shape of the profile. It can be noticed also that the values for the parameter governing the onset of breaking (Γ) are quite large when compared with the typical value $\Gamma = 0.78$. This can be explained in terms of the underprediction of shoaling by the model. Actual waves shoal significatively in a narrow region on the offshore face of the bar, resulting in a sudden steepening of the profile. The model in turn predicts a more gentle increase in wave height, underpredicting the peak. Consequently, in order to model the maximum wave height two alternatives are possible. Increasing the offshore value of the wave height, or letting the waves to shoal more before initiating breaking by increasing the value of Γ. The latter option allowed a better agreement with the breaking location observed by the lateral snapshots, and for that reason it was the preferred option. However, this was not enough and a combination of the two options was required.

Figure 4.4 shows the results of the modeling process, where an overall good agreement is found. The exception are the $T = 4.0$ s cases (Cases 2 and 6) where typically the point close to the shoreline was underpredicted. It was observed that for these cases, waves cease breaking after the bar and shoal quickly in the vicinity of bay 3($x = 81.97$ m), a behavior that REF/DIF1 was not capable to reproduce. In particular case 2 required a delicate balance between finding agreement for the maximum wave height or the profile shoreward of the bar. The latter option was selected because is in this region where shallow water nonlinearities are expected to be important.

In the case of the longer period runs, a region of continuous breaking was observed between the bar and the shore. Examination of the measured wave profile shows that wave heights appear not to be changing significatively in this region, probably due to a balance between breaking induced decay and shoaling. This combined effect was difficult to obtain on the numerical simulations. Although continuous breaking can be achieved by letting the parameter governing cessation of breaking to be small, this causes excessive dissipation and instabilities. Dissipation can be modified by changes on the parameter K, but this yields to a change on the slope of the profile, worsening agreement especially in the region between bays 11 and 09 ($x = 52.73$ and $x = 60.04$ m respectively), where wave heights decay due to deshoaling and breaking. Good agreement was found eventually by allowing waves to stop breaking at bay 09, followed by a region of gently shoaling waves

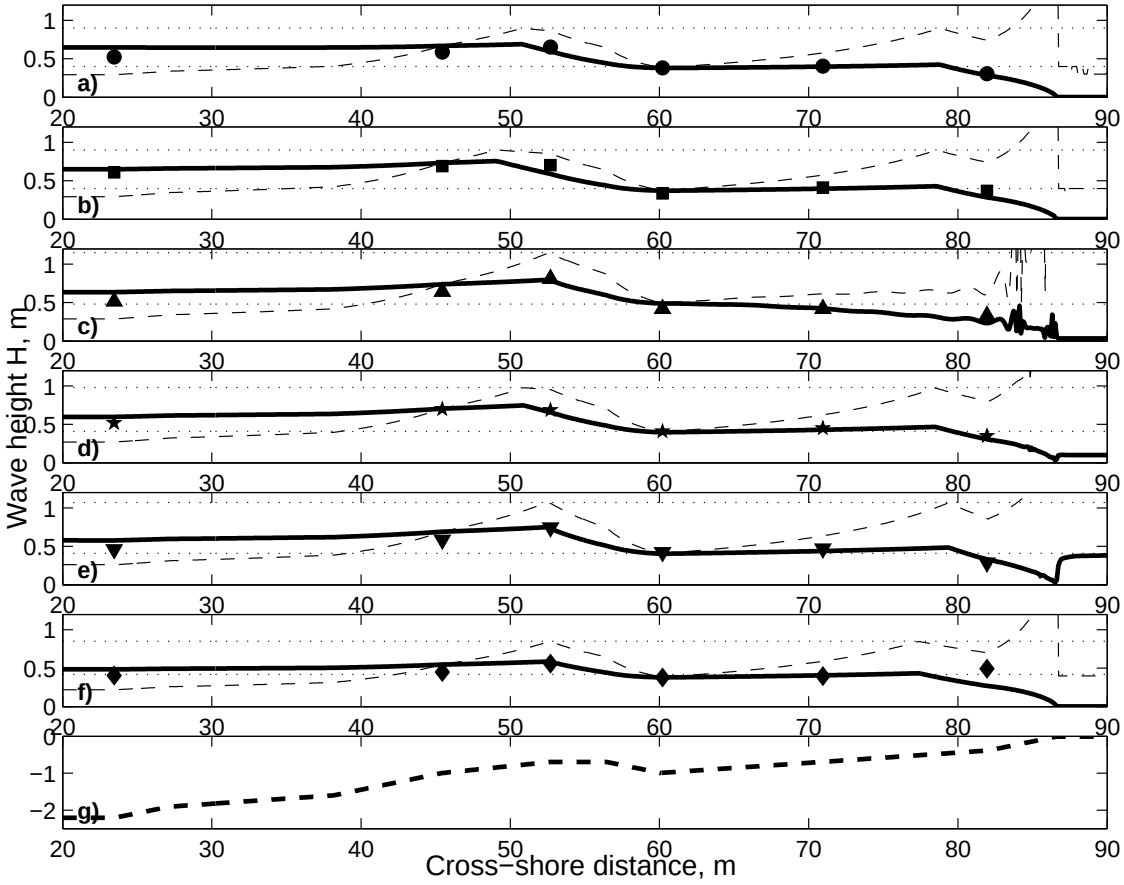

Fig. 4.4: Measured (symbols) and REF/DIF1 modeled wave height profiles (solid lines) $H(x)$. Dashed lines correspond to H/h profile, and dotted lines to the critical values for the onset and cessation of breaking. a) Case 1, b) Case 2, c) Case 3, d) Case 4, e) Case 5, f) Case 6, g) Bathymetry

until they break again close to the shoreline. Even though this is not consistent with breaking observations, our interest is focused on the wave profile rather than an accurate description of the process involved and this behavior was considered acceptable.

In summary, by modifying internal constants of the model and relaxing the offshore condition, it was possible to obtain an overall good agreement between the discretely sampled wave height profile and the numerical simulations. By doing this, a more densely sampled data set is obtained to be used on the nonlinear depth inversion.

4.3 Estimation of frequency, wavenumber and phase speed

Video collected data will be used to estimate phase speed, frequency and wavenumber. In the following a general overview of the results is presented for each of the methods tested.

4.3.1 Wave frequency and wavenumber.

The first parameter to be estimated is the wave period, by estimating the peak frequency f_p from video data. Wave period is obtained as $T = 1/f_p$.

Two methods are used for the estimation. First, the peak frequency f_p can be obtained using spectral analysis of the pixel intensity time series at different cross shore locations. The resulting power density spectrum has a fundamental frequency $\Delta f = 1/(N\Delta t)$, where N is the number of samples of each the time series, typically $N = 4500$ and $\Delta t = 0.1$. To improve the peak frequency estimation, a 3 point parabolic interpolation about the peak of the PSD at each cross shore location is used to determine the peak frequency. However, as pointed out before, the timestacks have been preprocessed as to minimize the background signal and therefore it is expected that the main signal correspond to the breaking related wave signature. However, as a result of the preprocessing, certain cross shore locations show a time series with little variance, and it is assumed that the signal to noise ratio is very low at these locations, making estimation of the peak frequency less clear. Therefore, the data set is screened as to retain cross shore locations whose signal to noise ratio is large. The selection is based on the comparison of the mean pixel intensity value of the time series with the mean pixel intensity value over the entire timestack. Thus, it is assumed that locations showing a larger temporal mean correspond to locations where the wave signal is strong and each of these locations provide an independent estimate of the peak frequency. The global peak frequency is thus estimated as the arithmetic average of the individual frequency estimates over the number of useful locations NL.

The second method estimates the peak frequency as the frequency of the first empirical mode obtained using CEOF analysis. Although the CEOF analysis explicitly provides

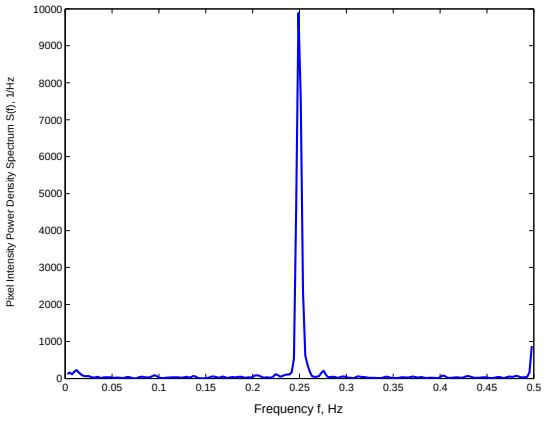

Fig. 4.5: Power density spectrum of the pixel intensity time series at $x = 50.25$, for case 2, $T = 4.0$ s, $H = 0.60$ s

the temporal evolution of the phase at each mode (thus the frequency time series), only the average value is used instead. Considering that accuracy of the CEOF method deteriorates toward the ends of the array (temporally and spatially (*Merryfield and Guza*, 1990)), the average is calculated over the centered 75% of the time series.

Table 4.3: Results for period estimation using spectral analysis

Case	$\bar{f}_p$, Hz	Std.Dev, Hz$*10^{-3}$	NL	$\hat{T}_p$	T	$e\%$
1	0.3706	0.2805	73	2.6983	2.7	-0.09
2	0.2494	0.1247	71	4.0095	4.0	0.48
3	0.2002	0.0284	114	4.9959	5.0	-0.21
4	0.1661	0.0583	83	6.0192	6.0	0.96
5	0.1246	0.049	88	8.0278	8.0	1.39
6	0.2491	0.1543	74	4.0139	4.0	0.69

Table 4.4: Results for period estimation using CEOF analysis

Case	$\bar{f}_p$, Hz	Std.Dev, Hz	$\hat{T}_p$	T	$e\%$
1	0.3701	0.0955	2.7019	2.7	0.10
2	0.2501	0.0887	3.9995	4.0	-0.03
3	0.2002	0.0789	4.9995	5.0	-0.02
4	0.1669	0.0888	5.9982	6.0	-0.09
5	0.1246	0.0922	7.9974	8.0	-0.13
6	0.2499	0.0999	4.0038	4.0	0.19

Table 4.3 and Table 4.4 show the results for both cases, where the error is defined as the percentage difference between the period estimate $\hat{T_p}$ and the input value T.

$$e = \frac{\hat{T_p} - T}{T} * 100 \tag{4.1}$$

As mentioned before, for linear inversions, errors in period induce an amplification of at least a factor of 2 on the depth estimate error (*Dalrymple et al.*, 1998; *Piotrowski and Dugan*, 2002). It can be seen that for the present cases agreement is generally good, with errors of order 1% for the spectral method and excellent agreement for the CEOF case, where the mean error is about 0.2 %. The worst estimate corresponds to the spectral estimate for Case 4, with 1.4% error. Based on the small standard deviations observed, the values obtained from spectral analysis will be used in the inversion algorithm. It can also be noticed that the screening process is very restrictive, since only ~ 90 of the total 234 cross shore locations are used in the estimation ($\sim 40\%$). However, it is considered that this value is large enough to provide an accurate estimate.

Estimation of wavenumber is straightforward once the radian frequency and the phase speed are computed ($k = \sigma/c = 2\pi f_p/c$).

4.3.2 Phase speed

Front tracking

The first method to be tested is the front tracking technique. As mentioned before, this considered the determination of the trajectory of the front of each individual wave, which was characterized as the points where the demeaned pixel intensity timestacks are equal to zero ($I(x,t) = 0$). Other definitions of the front were tested, for instance, a $\mu + n * \sigma$ threshold, where n=1,2,3 and μ, σ are the mean and standard deviation of the pixel intensity time series, respectively. Results showed little sensitivity to the front definition basically due to the very steep gradients in pixel intensity observed near the fronts.

Each timestack is sub sampled in space to improve computational time, by taking every other 10 time series. Thus the spatial domain is reduced to approximately 584 cross shore points with a discretization step of $\Delta x = 10cm$. Other values were tested

($\Delta x = 5, 10$ and 25 cm) and results showed little sensitivity upon the sub sampling value.

The simple average of the phase speed estimates at each cross shore location yield very noisy solutions, consistent with *Madsen et al.* (1997) findings. An 11-point two sided running average filter is applied to the speed estimate profile to reduce spatial scatter. This implies that speed estimates are averaged over 1.1 m, a distance small enough to retain the local trend of the phase speed profile.

Figure 4.6 shows the results for all the cases under study, along with the theoretical estimates of phase speed using the linear and composite dispersion relationships. It can be seen some common features for all cases. First, an offshore region of zero velocity is followed by a sudden increase in the velocity estimate, which is an indirect result of the transition from specular to diffuse reflection from the waves. As pointed out before, for the present experimental setup waves are visible to the video system mainly due to the latter, and consequently in regions where waves are not breaking waves are not clearly identified and have low values of pixel intensity. Therefore, when the threshold is applied to the image to find the points where $I(x,t) = 0$, these regions do not present a recognizable front and speed is not calculated by the algorithm. This explain the zero velocity values observed in the offshore region ($x < 45$ m for most of the cases). A second region is identified shoreward of this point, where waves start to break and the visible signature can be associated with a developing roller. As the roller grows in extension, some but not all the cross shore points in this region satisfy the front condition imposed, resulting in an oscillation of the estimate of speed between zero and nonzero values ($45 < x < 52$ m). Once the roller has developed, a third region can be recognized where more stable estimates can be obtained provided waves continue breaking.

Almost all cases exhibit spikes in the raw estimates near $x = 63.3$, which is the boundary between cameras 1 and 2. Spikes spanned several locations (about 1 m), suggesting that lens distortion may be playing a role here or misregistration of the pixel locations. This problem will be reviewed later in this chapter.

Another feature is observed near the shoreline, where the speed estimates exceed the theoretical values. We suspect that the reason for this is wave set up, which has

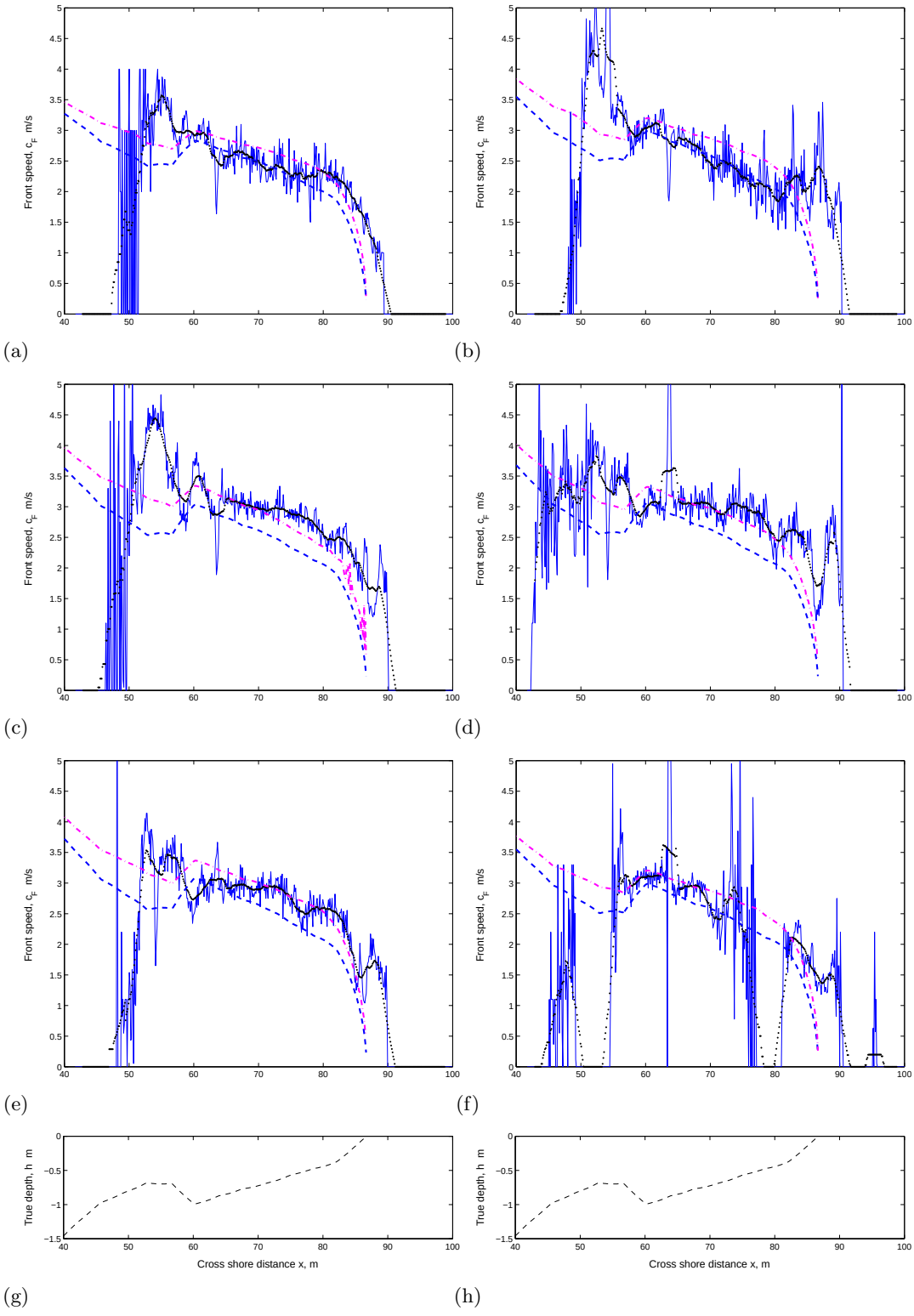

Fig. 4.6: Phase speed estimates using a front tracking technique. Raw estimates (light line), 11-point averaged estimates (dots),linear wave theory (dashed) and composite dispersion (dash dotted). a) Case 1; b) case 2; c) case 3; d) case 4; e) case 5; f) case 6 g) h) bathymetry.

not been accounted for in the calculations. Consequently, theoretical estimates consider zero velocity at the still water shoreline, whereas actual waves had a finite forward finite speed. However, it must be noticed that near the shoreline, swash motion corresponds to a standing wave propagating in both directions, which may cause incident waves to travel on top of this standing oscillation, affecting its speed. *Puleo et al.* (2003) found good agreement between measured speed in the surf and swash zone with the bore celerity estimates, suggesting that swash motions do not affect the incident wave speed significantly. Although back swash speeds can also be estimated from timestacks, the algorithm accounted for forward propagating features only.

Other local features can be noticed as well. Speeds are largely overpredicted over the bar and the functional shape of the speed profile in that region shows almost no correlation with the theoretical estimates. Similarly, some cases show a strong positive gradient of speed near the shoreline followed by quick decay. Analysis of the timestacks at the corresponding locations showed that both regions are characterized by a strong generation of foam, both propagating and persistent which is associated with strong breaking. Eventually, this can be attributed to the combined effect of roller growth and roller movement relative to the wave. As the roller establishes, it slides down along the front of the wave, effectively propagating faster than the wave itself, until it reaches a stable position relative to the wave, where it slows down until its speed relative to the wave is zero. This process was described by *Basco* (1985) and can be appreciated qualitatively on Figure 4.7 , corresponding to case 1. The region delimited by the vertical lines on the figure correspond to the most intense breaking signal for that event. Analysis of the timestack shows that the front of the breaking signal has a very steep positive slope, followed by region of relatively stable slope and a final deceleration. Furthermore, for this case waves were typically plunging in the region near bay 11 ($x = 52.73$ m). Analysis of the lateral snapshots showed in some cases a clear overturning of the wave with a foamy crest and a resplash from the plunging jet from the trough of the previous wave. It should be noted that if this is the case, the point actually recorded on video images would correspond to some unidentified point between the wave crest and the wave front. It expected that this will result in an spurious velocity not explained by the dispersion

models used and may explain part of the discrepancies observed on regions of strong breaking.

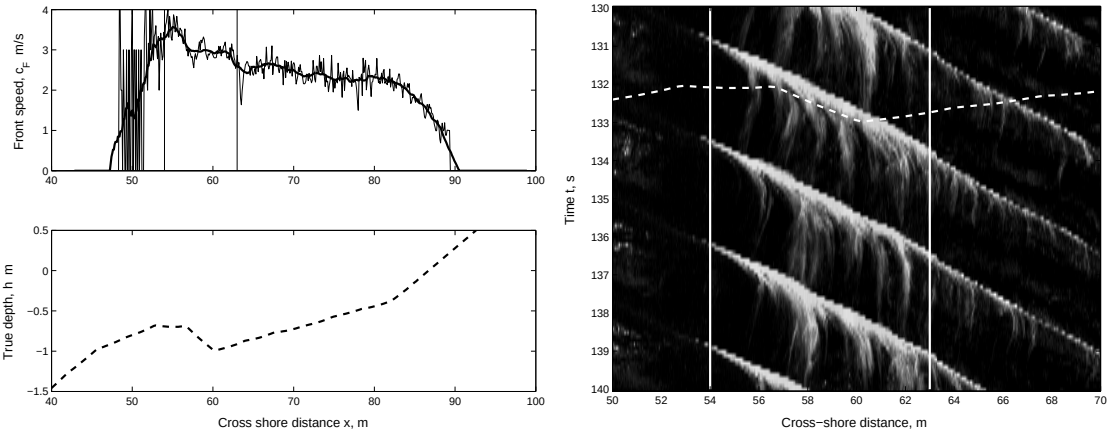

(a) (b)

Fig. 4.7: Phase speed estimate using a front tracking technique, for case $T = 2.7$ s, $H = 0.60$ m. a) Raw phase speed profile (thin) and filtered profile (thick) b) blow up of the corresponding timestack in the region of initiation of breaking. Vertical lines correspond to the initiation of roller growth and its stabilization at the wave front.

Crest tracking

In an attempt to minimize the observed effects apparently related with roller growth, a crest tracking technique was implemented. However, identification of the crest is ambiguous, at least in the sense that the observed quantity would actually correspond to the crest of the actual wave. The crest is assumed to correspond to the location of maximum of pixel intensity, but this initially presents the problem of saturation of the pixel intensity signal ($I = 255$) for relatively long periods of time. To minimize this effect, an ensemble averaged timestack is used instead, which exhibits a smoother surface, as can be seen on Figure 4.8 .

The ensemble averaged timestack is scanned in both dimensions, and maxima sets are obtained for each scan. It is assumed that the crest would correspond to the intersection set of the maxima. The technique is illustrated on Figure 4.9 , where multiple values of maxima are found when scanning in space due to the window size used. The final set appears to be well correlated with the wave trajectory (Figure 4.9 b)).

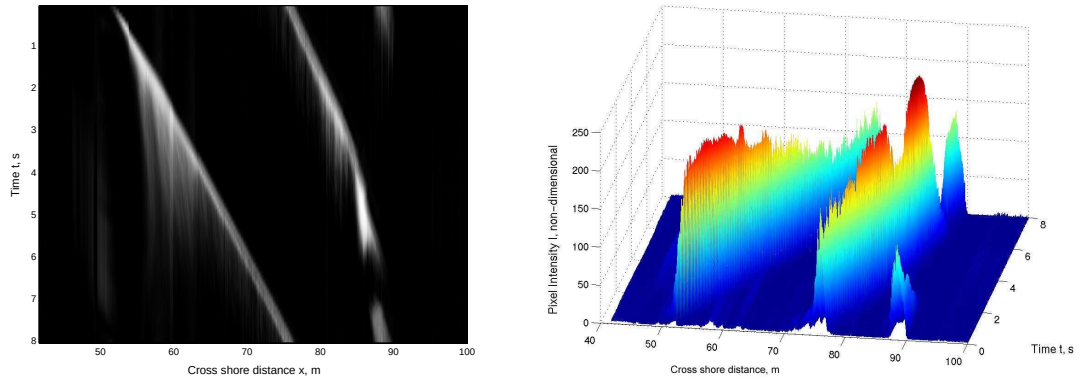

(a) (b)

Fig. 4.8: Phase averaged timestack for $T = 8.0$ s, $H = 0.40$ m. a) Timestack b) Surface

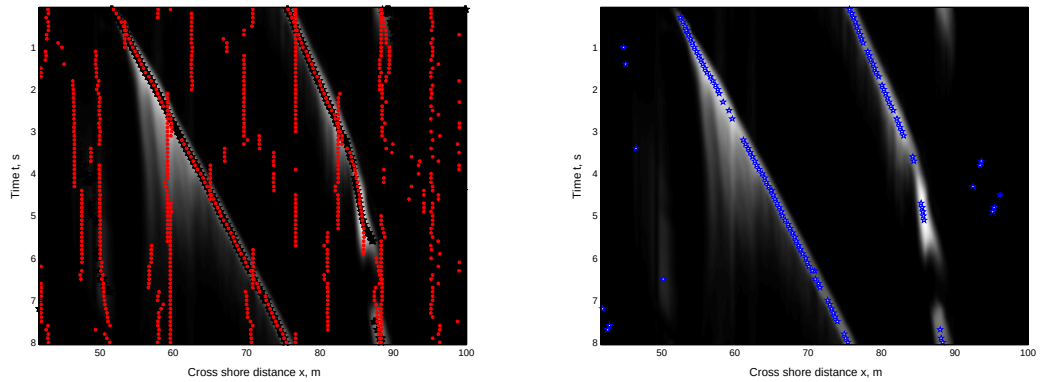

(a) (b)

Fig. 4.9: Crest selection routine for $T = 8.0$ s, $H = 0.40$ m., a) location of identified maxima using a time scan (stars) and spatial windows scans (circles) b) Intersection set

The intersection method causes the resulting data set to be coarser spatially and temporally, and is linearly interpolated to grid resolution, as shown on Figure 4.10 a). The local estimate of phase speed is obtained as the local slope for both the interpolated and the original data set. An example of the results is shown on Figure 4.10 .

Results typically showed a high amount of scatter, a behavior attributed to local shifts in the location of the maxima of pixel intensity relative to the true wave signal. A similar source of inaccuracy was reported by *Suhayda and Pettigrew* (1977) for a situation where the crest could be clearly identified, where wave shape changes caused a difference

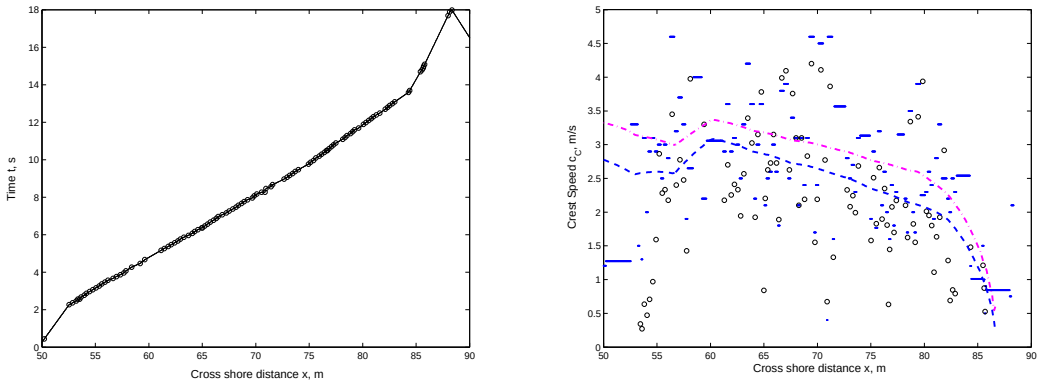

(a) (b)

Fig. 4.10: Crest tracking results for $T = 8.0$ s, $H = 0.40$ m., a) Linear interpolation of the crest trajectory, (circles) measured data set and (dots) interpolated set; b)Speed estimates for the interpolated (dots) and measured data set (circles).

in the velocities of the whole wave and the crest. *Lippmann and Holman* (1991) found, however, that peaks in the intensity series of breaking waves were well correlated with actual wave peaks, but a proper assessment would require one to one comparison between the pixel intensity time series and a synchronous wave gage time series, something not available for the present case. The use of filtering in the form of running averages did not provide improvements on the signal, and the crest tracking technique was consequently discarded.

Cross spectral methods

Considering that period estimation offered good results, the use of cross spectrum between closely spaced sensors (pixels) appeared to be a good technique to estimate phase speed. Furthermore, the technique has been widely used in field estimations of celerity (e.g. *Thornton and Guza*, 1982; *Holland*, 2001) and also using remote sensing techniques (e.g. *Lippmann and Holman*, 1991; *Curtis et al.*, 2002).

The input data set corresponds to the merged timestacks. An 11-point running average was applied in the time domain to remove high frequency variability. The data set is down sampled in space every 25 cross shore points to speed up computations, resulting in a spacing between sensors of $\Delta x = 0.25$m.

Estimates of the cross spectrum, phase and coherence are obtained for all pairs of consecutive wave gages. The resulting data set is screened in order to remove cross shore locations where the local peak frequency estimate $\hat{f}_x$ differ by more than one standard deviation from the global peak frequency estimate (e.g. Table 4.3). In addition, pairs where coherence was less than $\gamma^2 = 0.85$ where discarded as well. Typically phase speed results showed a few outliers, that were removed by consecutive application of a 1-sided standard deviation filter, until the standard deviation of the phase speed profile was less than 5 m/s. This value is selected arbitrarily, but previous results and theoretical values showed that the maximum speed would be of $O(5$ m/s), therefore this value allows retention of a few moderately large local estimates. Results are interpolated to the original resolution and an 11 point filter is applied, consistent with other methods used here.

Figure 4.11 shows the results obtained for all cases. It can be observed that speed estimates are usually bounded by the speed estimates obtained by linear wave theory and the composite dispersion, but show a large amount of variability. Similarly to what was observed for the front tracking methods, offshore estimates of speed are very small and usually underpredicted in the crest of the bar, something that can be related again with the viewing mechanism. Shoreward of the bar, variability shows an oscillatory pattern with relatively stable wavelengths, of the order of wavelength of the wave. A similar result for regular waves propagating over a bar-through system was obtained by *Grilli and Skourup* (1998), where it was argued that the cause of these modulations is the release of free waves at harmonic frequencies due to wave deshoaling on the shoreward face of the bar. Analysis of the power density spectrum for the present study shows in some cases up to 4 harmonics (e.g. for the longer wave), suggesting that these modulations effectively are taking place. In any case, the presence of these modulated phase speed profiles hinders significatively the applicability of this method for depth inversion using regular waves.

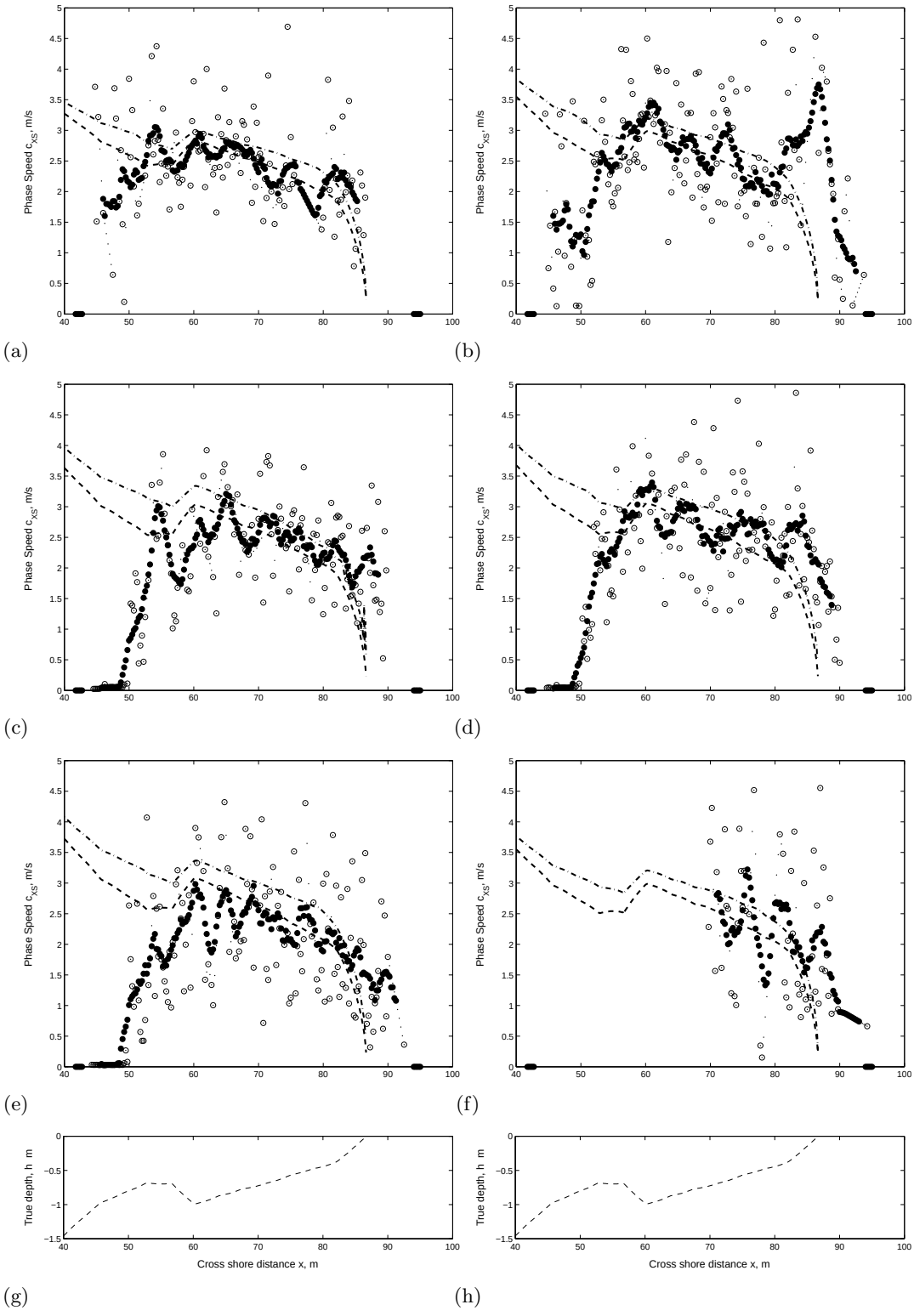

Fig. 4.11: Phase speed estimates using a cross spectral methods, raw results (circles) 11-point averaged (dots),linear wave theory (dashed) and composite dispersion (dash dotted). a) Case 1; b) case 2; c) case 3; d) case 4; e) case 5; f) case 6 g) h) bathymetry.

CEOF analysis

Phase speed estimates were also estimated using time domain CEOFs. Although frequency domain EOFs have been used successfully by *Stockdon and Holman* (2000) for depth inversions, a time domain is adopted here in order to estimate the presence of propagating signals of different frequencies, specifically harmonics.

Considering that CEOFs will try to explain the variability observed in the time series, the input timestacks are screened and the regions with low variability at both spatial ends are removed for the analysis, by adopting a threshold based on the overall variance on the timestack. This effectively reduces the maximum distance between sensors, ΔX.

Merryfield and Guza (1990) showed that the amount of variability explained by the first mode is dependant not in the number of gages used, but on the parameter $\Delta k \Delta X$, where Δk is the wavenumber bandwidth, an ΔX is the maximum distance between sensors. Ideally, this parameter has to be of $O(2\pi)$ as to maximize the variance of the first mode. At the same time, the array has to be long enough to resolve the wavenumber of the waves present. In our case, the longest wave has a wavelength of $L = 36$ m at the offshore face of the bar, while the maximum usable length for the array is $\Delta X = 35.26$ m (after removing the low variability ends). Therefore, it is expected that waves can be resolved, but variability would probably be spread between various modes. As a result, the amount of variance in the first mode is not expected to change significatively by changing the number of gages. A sensitivity test was performed using ($\Delta x = 5, 10, 25, 50$ and 100 cm) and confirmed this assumption. Though resolution obviously decreased, the overall trend on the speed profile is retained regardless of Δx, as can be seen on Figure 4.12 . Finally a discretization of Δx=0.25 m was selected for consistency with the previous methods.

Table 4.5 shows the variance explained for the first three modes and the associated frequencies. It can be seen that frequencies corresponding to the first three harmonics are well retrieved, but the accumulated variance explained by the first three modes is typically of order 50%, which can be considered as a poor performance by the method.

Phase speed estimates for the first three modes of each case are shown on Figure

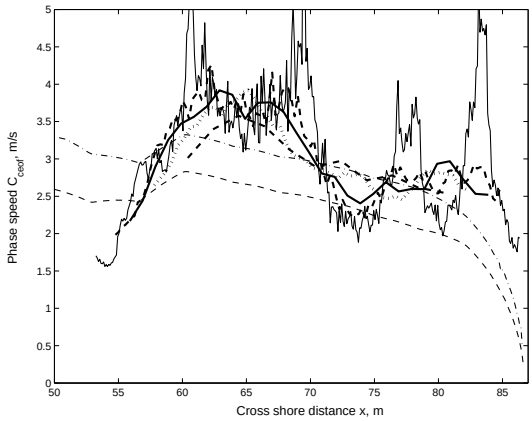

Fig. 4.12: Sensitivity test for CEOF results depending on discretization size, Δx: 10 cm (thin line), 25 cm (dotted line), 50 cm (thick line), 200 cm (thick dashed line)

Table 4.5: Variance and observed frequencies for the first three modes obtained by CEOF analysis. f_o corresponds to the theoretical input frequency.

Case	Variance explained by mode %				Mode frequency, Hz			f_o	Δx
	M_1	M_2	M_3	Σ	M_1	M_2	M_3	Hz	m
1	35.53	12.26	6.36	54.15	0.37	0.74	1.11	0.37	0.25
2	46.57	12.33	5.31	64.21	0.25	0.50	0.75	0.25	0.25
3	35.29	13.16	7.22	55.67	0.20	0.40	0.60	0.20	0.25
4	33.09	14.13	7.99	55.22	0.17	0.33	0.50	0.17	0.25
5	30.22	13.45	7.47	51.14	0.12	0.25	0.37	0.13	0.25
6	42.90	11.89	5.73	60.53	0.25	0.50	0.75	0.25	0.25

4.13 . Again results show an oscillatory behavior about the composite model, but with larger amplitudes. The oscillation observed for Case 3 has a wavelength of roughly 15 m, whereas the linear estimate of wavelength for the average depth between the bar through and the shoreline yields 12.9 m, suggesting that modulation is present. However, it can be observed also that the speed of modes 2 and 3 is very similar to that of the main mode, something that eventually could be interpreted as locked harmonics and is not consistent with free harmonics. However, considering the relative low variability explained by the first mode one possibility is that higher modes are contaminated by variability leaked from the first mode.

One alternative that was not tested is reducing the bandwidth Δk by frequency averaging the covariance matrix over a narrow band of frequencies, which corresponds to

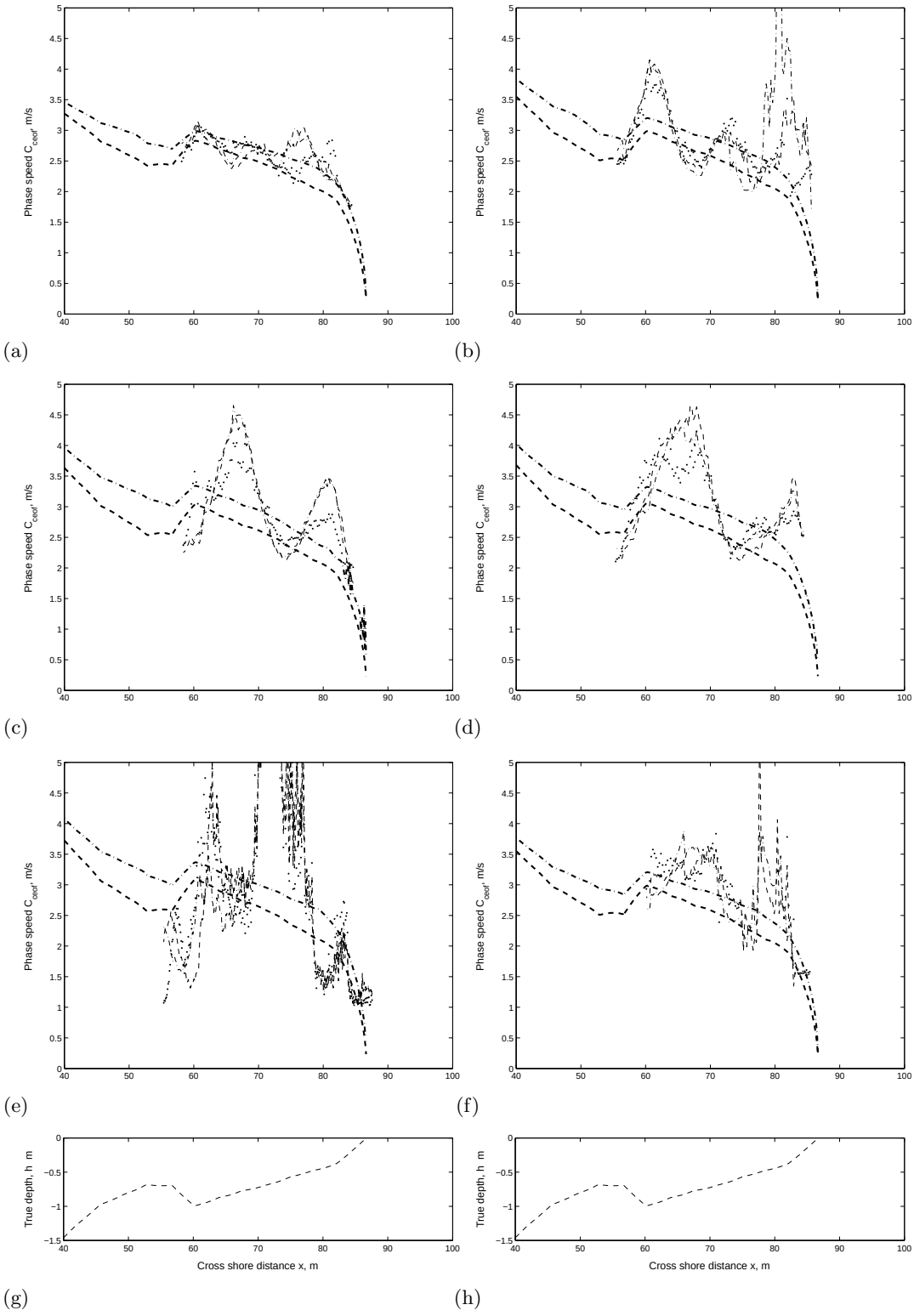

Fig. 4.13: Phase speed estimates using CEOF analysis with $\Delta x = 0.25$ m, showing modes 1 (solid), 2 (dashed), 3 (dash dotted) ,linear wave theory (thin dashed) and composite dispersion (thin dash dotted). a) Case 1; b) case 2; c) case 3; d) case 4; e) case 5; f) case 6 g) h) bathymetry.

a frequency domain EOF (*Merryfield and Guza*, 1990). Eventually, this would result in a higher variance explained by the first mode and would help to differentiate the presence of harmonics.

4.3.3 Misregistration

To this point, all the methods described assumed that the timestack provide the true world coordinates of the wave. For the video technique, the absolute location of a visible point on the camera field of view can be obtained by applying a set of transformation equations between the 2-D image space to the 3-D world coordinates. However, in general this system has 11 unknowns and only two direct linear equations. Determination of the transformation requires thus knowledge of the world and image locations of a set of at least six control points (GPC, ground control points). However, determination from a single camera is not possible unless one of the world coordinates is constrained *Holland et al.* (1997). With this constraint and knowing the location of the cameras, as little as two GCPs are required to solve the equations.

Hence, the usual assumption for field observations is that the signal has little variability in the vertical direction when compared with the horizontal accuracy, and all points are assumed to be at $z = z_0$. As a consequence, the image can be rectified and the corresponding horizontal world coordinates (x, y) of the visible point observed by the pixel located at (u, v) in image space are known. The one to one relation between a pixel and the spatial point is thus predefined (*registered*) and fixed for each run.

For the experimental set up used in this study, the assumption of little variability does not hold true, because the free surface has a finite vertical displacement $\eta(x, t)$, but the data collection technique assumed that this displacement was negligible and assumed all points to be located at $\eta = 0$. In consequence, the true laboratory coordinates of the visible point are different and do not correspond to the assumed ones, thus the point is being *misregistered*. Possible solutions include a relocation of the cameras as to minimize the vertical variability (the optimal location would be pointing vertically down); a dynamic correction of the transformation coordinates; or an estimation of the induced error. The first option has some technical difficulties regarding data transmission

and instrument deployment and has not been attempted yet, but obviously would require new data collection discarding the existent data set. The second is a very complex option and would require at least knowledge of the instantaneous free surface to generate a new rectification matrix at each time step. In consequence, the only plausible option is to obtain an estimate of the error induced by the vertical constraint assumption and use it to correct the phase speed estimates for latter calculations. The timestacks could be resampled spatially to correct the distortion, but apparently book-keeping of the correction is not obvious. In the following, an estimate of the distortion is calculated and presented as horizontal error bars.

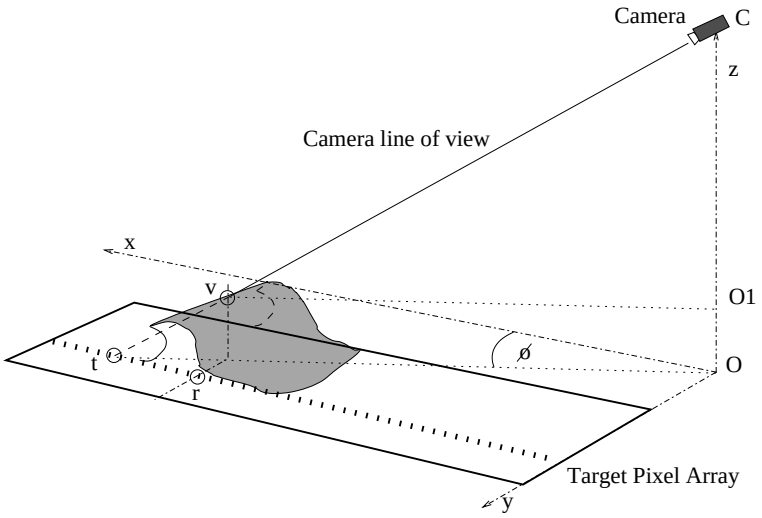

Fig. 4.14: Misregistration of the pixel array. The target pixel (t) is shadowed by the finite amplitude wave at point (v), which has a corresponding location (r) when projected over the pixel array.

Though it might be possible to find an analytical solution for a simplified free surface displacement, we attempt to solve the problem on a geometrical basis. Figure 4.14 shows an schematic of the problem. Without loss of generality, the analysis is presented herein for a single pixel on a given pixel array, thus its registered world coordinates (x_t, y_t, z_0) are known. This pixel is termed as the *target*. The camera location (x_c, y_c, z_c) is also known and it is assumed that both points do not move during each run. Therefore, the azimuthal angle defined as

$$\phi_t = \tan^{-1}\left(\frac{y_t - y_c}{x_t - x_c}\right) \tag{4.2}$$

is fixed and known for each pixel on the target array. Misregistration occurs when a finite amplitude wave interferes in the line of view between the camera and the target. In this situation, the point observed by the camera is not the target, but some unknown point on the wave surface(v on Figure 4.14) which has world coordinates $(x_v, y_v, z_0+\eta_v)$. Considering that waves are traveling along the $x-$coordinate, we need to estimate the value of $x_r = x_v$, which corresponds to the projection of v over the pixel array, showed as r on the figure. Longshore wave form variations are assumed to be negligible.

x_v can be estimated by similarity between the triangles $\triangle CtO$ and $\triangle CvO_1$, where the distance $\overline{OO_1}$ is equivalent to η_v. The maximum difference error $x_t - x_r$ occurs when η_v is maximum, therefore a estimate of the error can be done by assuming that $\eta_v = A$, the known wave amplitude previously calculated from the numerical simulations. Troughs are not considered because they do not posses a visible signature and have not been used to estimate phase speeds.

It might be apparent that another error is being induced by this procedure, that is the assumption that the visible pixel corresponds to the crest of the wave. It is assumed implicitly that the true front of the wave is *shadowed* by the crest, therefore a clear distinction between the two is not possible, but the error introduced should be within the error made on estimating A, therefore accuracy is not degraded. The method is applied to all cameras and all pixels on each pixel array. Estimation of the visible points $(v's)$ is done by computing the intersection of the plane generated by all the lines of view and the surface generated by an longshore uniform wave amplitude profile.

As a result, the cross-shore location of each pixel can be corrected. It is important to mention that this misregistration error is not expected to induce a significant error on the speed estimates, because phase speeds are calculated basically as local gradients of the trajectory and the misregistration causes an overall translation of the trajectory, of the same order for two consecutive points. In addition, misregistration causes the discretization size to be reduced as

$$\frac{\Delta x_{\text{true}}}{\Delta x_{\text{target}}} = \frac{z_c - A}{z_c} \tag{4.3}$$

where Δx_{true} is the corrected step size, Δx_{target} is the registered step size ($\Delta x_{\text{true}} = 0.25$ m), $z_c \approx 14.10$ m is the vertical position of the camera relative to the target plane, and A is a measure of the vertical offset caused by finite amplitude waves. This difference affects the speed estimates as $(\Delta x_{\text{true}} - \Delta x_{\text{target}})^{-1}$. Using the maximum wave amplitude observed in the surf zone ($A = 0.25$ m), the maximum error is about 1.8% on the speed estimate. However, this value would occur only in the vicinity of the maximum wave height. Hence misregistration is assumed to affect the location but not the magnitude of the speed.

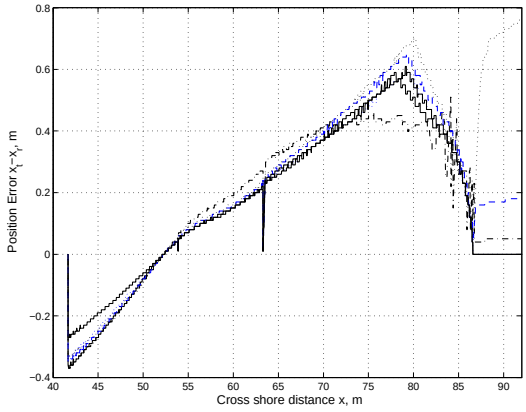

Fig. 4.15: Estimation of cross shore position error induced by misregistration, for all cases.

Results of the method can be observed on Figure 4.15 , from where it can be seen that maximum displacements are about 70 cm, corresponding to roughly 3 pixels in the subsampled series used for speed estimation. Misregistration reduces the effective domain, by shifting offshore (relative to the camera) pixels onshore and viceversa. The zero crossing of the error corresponds to $x = 52.20$ m, the cross-shore location of camera 3, meaning that at this location the line of view is perpendicular to the pixel array. Spikes at $x = 63.3$ m and $x = 53.87$ m correspond to the boundaries between cameras. The cause of these spikes is not clear but might be associated with the observed spikes on the

front-based speed estimate.

Front tracking speeds can be corrected by shifting their cross shore locations. Results are shown as horizontal error bars on Figure 4.16 . Though the error appears to be relatively small, it would effectively shift the speed estimates toward the linear dispersion relationship, thus they might have an influence on the depth inversion algorithm. However, they are not included in the analysis explicitly.

4.3.4 Summary

Different techniques to estimate phase speeds from the data records were tested. From these, front tracking appears to be the one in closest agreement with theoretical estimates, but with a large amount of scatter. However, this does not necessarily mean that the method is providing the correct answer for the speed of propagation of the fundamental frequency, because the method follows the front of a wave of changing form, thus several frequencies are included. In addition, other methods tested showed modulation on the speed estimate of the fundamental consistent with previous findings for monochromatic waves, something not observed for the front based speed estimate. Nevertheless, it is expected that if the front tracking estimate is used in the region with good agreement with theory, it might provide a useful estimate for depth inversion.

The final set to test the nonlinear depth inversion is reduced to 5 cases (Cases 1 to 5), because Case 6 exhibits a region of zero velocity and the more abrupt change at the boundary between cameras, making it less suitable for inversion.

4.4 Depth inversion

Once all the relevant parameters ($A(x), \sigma, c(x)$ and $k(x)$) are estimated, depths were obtained explicitly using the linear dispersion relation

$$h = \frac{1}{2k} \ln \left(\frac{gk + \sigma^2}{gk - \sigma^2} \right) \tag{4.4}$$

and iteratively using the composite dispersion model (*Kirby and Dalrymple*, 1986) given by Eq. 3.1 .

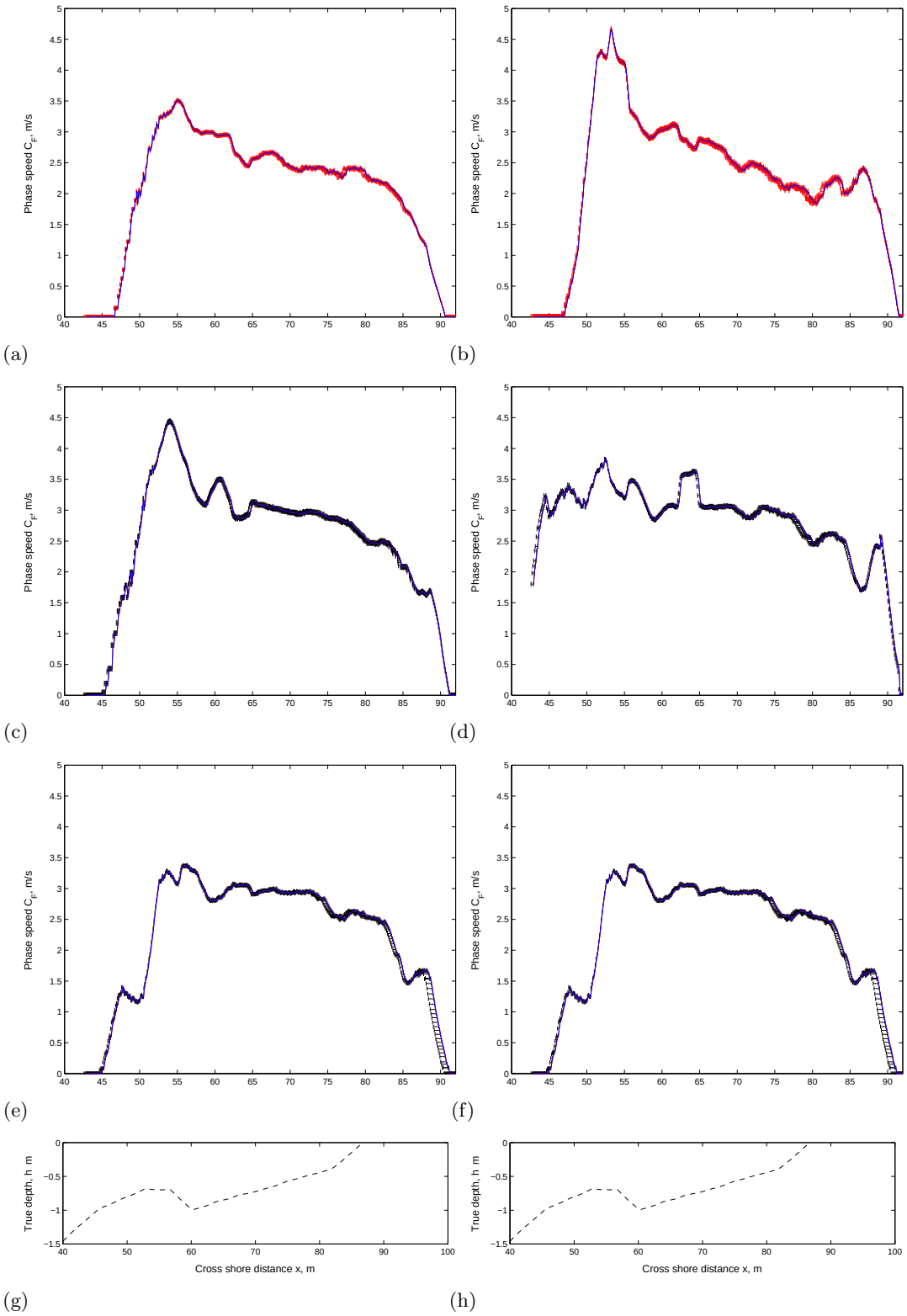

Fig. 4.16: Front tracking phase speed. Error bars correspond to the cross shore shift due to misregistration. a) Case 1; b) case 2; c) case 3; d) case 4; e) case 5; f) case 6 g) h) bathymetry.

Although speed estimates were obtained beyond the still water shoreline, the current implementation of the algorithm does not account for wave set-up, and wave heights were calculated up to the shoreline only. Consequently, depth estimates beyond the still water shoreline and points with zero velocity are removed from the analysis. As a consequence, the spatial domain is further reduced, covering $x = 46.9$ m to $x = 86.55$ m.

Accuracy of the depth estimates is analyzed based on the difference and relative errors, defined as (*Stockdon and Holman*, 2000)

$$D(x) = \hat{h}(x) - h(x) \tag{4.5a}$$

$$R(x) = \frac{\hat{h}(x) - h(x)}{h(x)} * 100 \tag{4.5b}$$

where $\hat{h}(x)$ is the sample estimate obtained using one of the inversion techniques and $h(x)$ is the true still water depth. D is measured in meters and R in percentage. Positive values of D (R) represent an overestimate of depth.

To estimate performance over each individual profile, mean values of each error are calculated as

$$\bar{\Phi} = \frac{1}{N_x} \sum_{i}^{N_x} \Phi(x_i), \qquad \Phi = D, R \tag{4.6}$$

where N_x is the number of cross shore points where depth has been estimated. These performance indicators are affected by the sign of each individual estimate, allowing cancelation ($\bar{\Phi} = 0$), something that can be misleading. For this reason, an estimate of the variability of the error over the profile is also obtained as an RMS estimate

$$\Phi_{\text{rms}} = \sqrt{\frac{1}{N_x} \sum_{i}^{N_x} \Phi^2(x_i)}, \qquad \Phi = D, R \tag{4.7}$$

which is insensitive to the sign.

Depth estimates are obtained for each individual case. An average profile is obtained by computing the median of the 5 estimates at each location. The usage of the median is suggested by *Stockdon and Holman* (2000) because it is less sensitive to outliers and

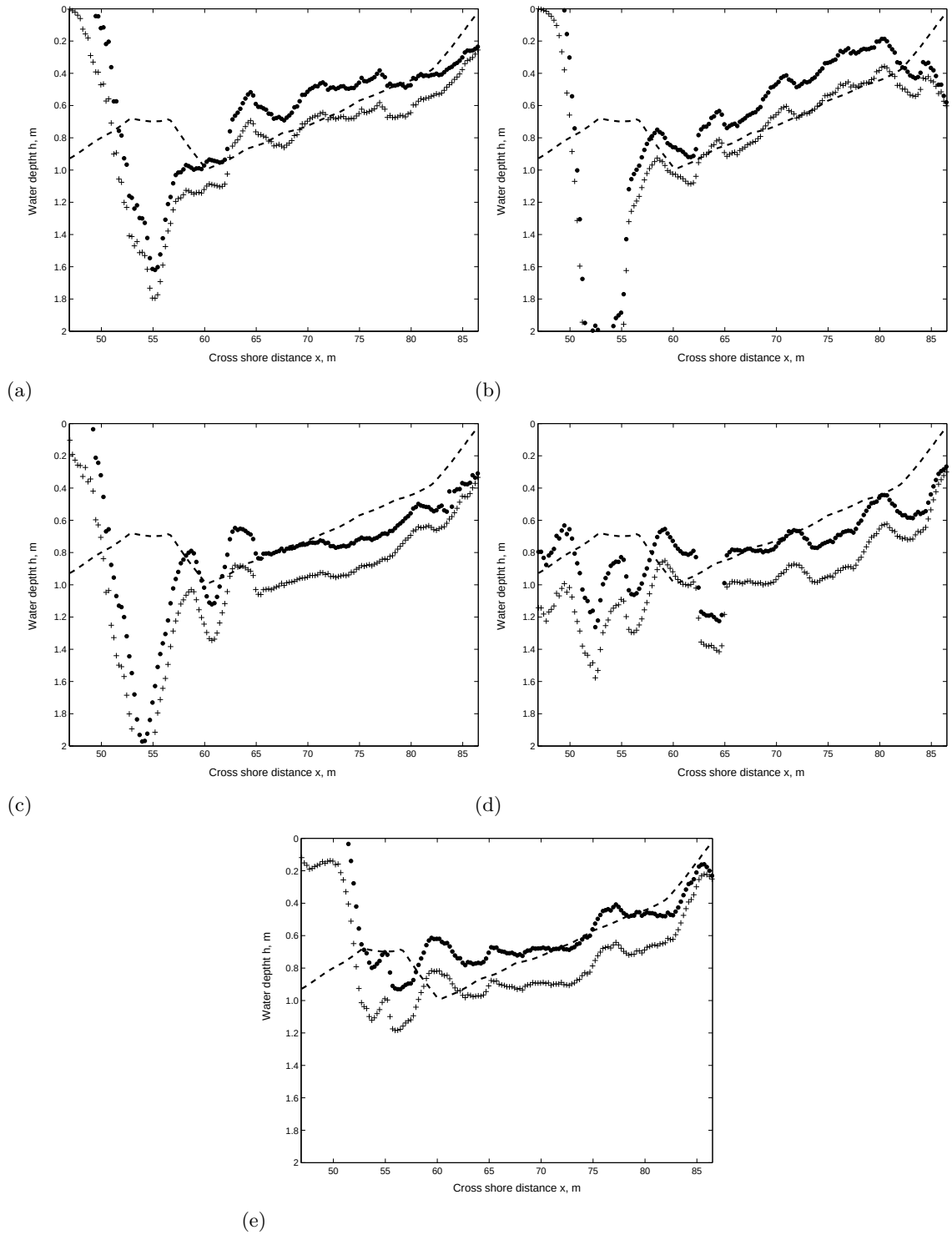

Fig. 4.17: Estimated depth profiles linear (pluses), composite (dots) a) Case 1; b) case 2; c) case 3; d) case 4; e) case 5.

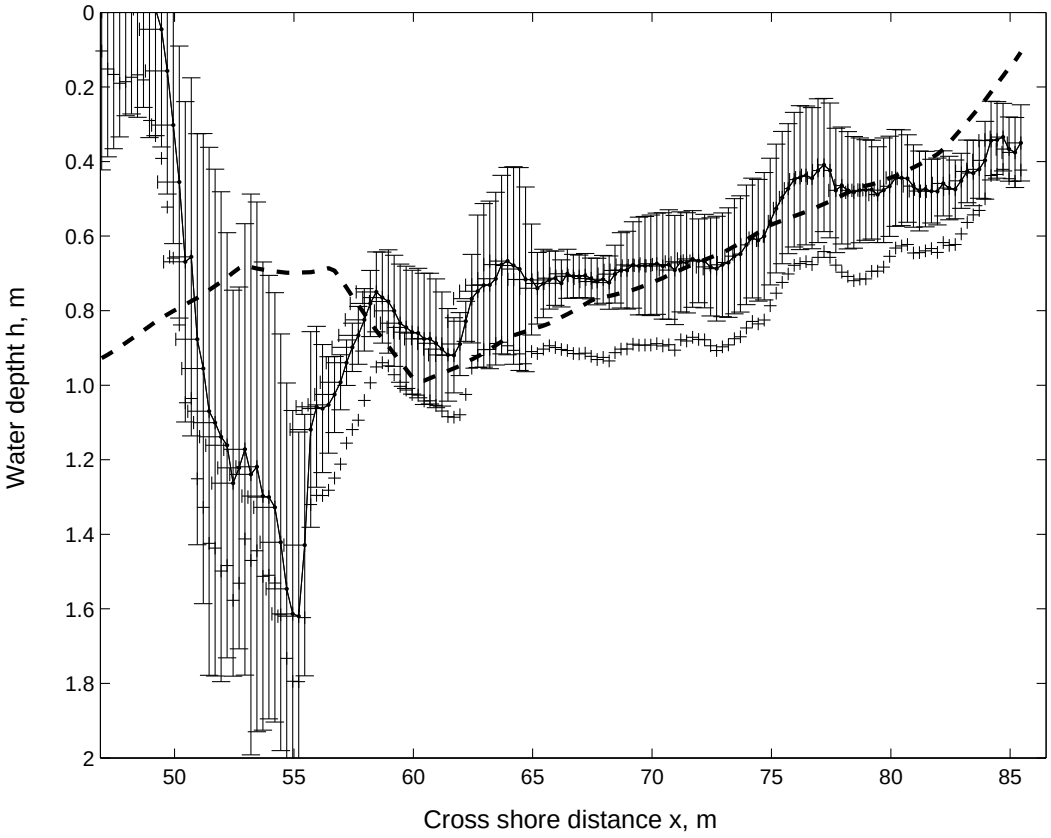

Fig. 4.18: Estimated average depth profile using linear (pluses) and composite (dots) dispersion. Vertical error bars correspond to one standard deviation for the composite model and horizontal error bars correspond to the misregistration error.

it was found to be more accurate.

Results for all individual cases are shown on Figure 4.17 . It can be seen that depths over the bar are severely overpredicted and show little correlation with the bar shape, as a result of the large estimates of the velocity in that region from the front tracking technique. Shoreward of the bar, individual profiles appear to be more correlated with the actual depth, although showing a significant amount of scatter. Interestingly, shorter periods appear to produce better estimates with the linear dispersion relation, but as the period increases, linear theory estimates get worse and the composite model improves. This is consistent with the observed behavior of linear estimates in shallow water (e.g. *Stockdon and Holman*, 2000; *Holland*, 2001).

Somewhat surprisingly, the average profile is relatively smooth and shows an overall

good agreement with shoreward face of the bar and the planar beach, specially in the region $60 < x < 83$ m. Shoreward of $x = 83$ m , the beach steepens and both methods exhibit depth overprediction. Apparently, the retrieved depths correspond to the local instantaneous depth including set up. Difference errors in this region were of order $O(10)$ cm, a value consistent with set up. In addition, it can be observed that in this region the composite dispersion estimates show an asymptotical behavior toward the linear model, because REF/DIF1 computed amplitudes decay quickly to zero at the shoreline.

Table 4.6: Accuracy of depth estimates for individual profiles and the average profile. $60 < x < 85.5$, $N_x = 102$

Case	Linear				Composite			
	$\bar{D}$	D_{rms}	$\bar{R}$	R_{rms}	$\bar{D}$	D_{rms}	$\bar{R}$	R_{rms}
	m	m	%	%	m	m	%	%
1	0.08	0.13	47.24	151.90	-0.08	0.15	15.70	135.93
2	0.05	0.15	72.52	357.42	0.12	0.21	39.56	344.19
3	0.03	0.27	0.87	210.22	0.08	0.15	51.13	165.50
4	0.29	0.31	90.11	194.75	0.10	0.17	53.51	167.49
5	0.16	0.19	55.20	146.28	-0.04	0.12	17.43	127.09
Avg	0.17	0.19	41.74	63.83	-0.02	0.10	7.26	40.99

Table 4.7: Accuracy of depth estimates for individual profiles and the average profile. $60 < x < 82.5$, $N_x = 89$

Case	Linear				Composite			
	$\bar{D}$	D_{rms}	$\bar{R}$	R_{rms}	$\bar{D}$	D_{rms}	$\bar{R}$	R_{rms}
	m	m	%	%	m	m	%	%
1	0.06	0.11	11.61	21.26	0.12	0.16	-16.20	20.79
2	0.00	0.06	0.49	9.36	-0.18	0.20	-29.67	33.24
3	0.24	0.26	39.91	44.87	0.05	0.13	11.58	21.93
4	0.27	0.30	44.08	49.57	0.07	0.14	12.32	21.28
5	0.15	0.18	26.78	33.69	-0.06	0.12	-6.90	14.54
Avg	0.16	0.17	27.14	32.41	-0.05	0.09	-5.13	11.86

Although agreement for the average profile appears to be good even at the shoreface of the bar, the analysis will focus on the region shoreward of the bar trough, $60 < x < 85.5$ m. Performance estimators are shown on Table 4.6 . It is clear that estimates based on a single case show a poor performance. Typically the mean bias was of order 10 cm (overprediction) for both dispersion models, but for the longer periods, the composite

model showed comparatively half the variability (D_{RMS}) of the linear model. Relative errors showed on Table 4.6 are large, but its analysis is difficult when the very shallow true depths are used for comparison. As $h \to 0$, computation of $R(x)$ diverge, making the analysis difficult. This is behavior can be seen on Figure 4.19 , where the median value of the relative error at each location is shown. Clearly, relative errors increase abruptly around $x = 80$ m ($h \sim 0.40$ m).

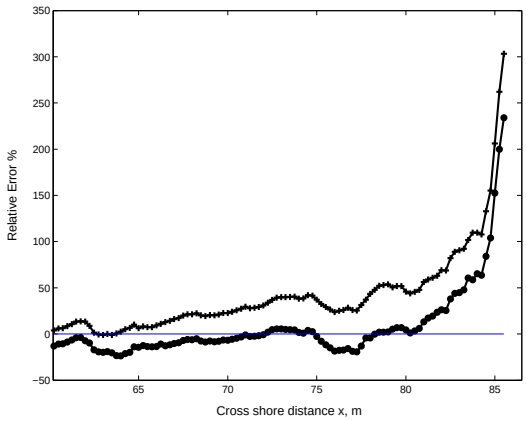

Fig. 4.19: Median relative error profile $\bar{R}(x)$ for linear (pluses) and composite (circles) based inversions.

As observed from Figure 4.18 and Table 4.6 , performance estimators for the average profile shows an overall good correlation, with relatively low values for D_{rms}, where the composite model reduced the variance in half relative to the linear model. The bias estimator $\bar{D}$ shows a very low value for the composite case, suggesting that cancelation is occurring. Again, analysis of the relative errors is difficult due to the small values of the true depth. In order to minimize this effect, another subset is analyzed, by using only the portion where the true depth is larger than $h = 0.35$ m. This value is selected arbitrarily, but is close to the depth where the change of slope is occurring and close to the location where relative errors increase. The new subset domain covers only a uniform slope section of the beach, $60 < x < 82.5$ m.

Results are shown on Table 4.7 . The difference error estimates for individual profiles varied when compared with the longer set, but the RMS estimate did not change significatively. This suggests that variability was either uniform or it was mainly influenced

by this larger section of the profile. The previous finding that linear wave theory performs better with shorter periods and composite does it better for long period cases is confirmed. Error estimates for the average profile did not change significatively, showing that the use of the composite model reduces the mean relative error from order 27% (RMS 32%) to order 5% (RMS 12%).

Interestingly, the composite result shows a change in the bias sign. Where typically linear theory overpredicted the depths because of the larger (nonlinear) velocities, for the present results incorporation of nonlinearity induced an underprediction of the depths. One possible reason can be related with uncertainties in wave amplitude, suggesting overprediction of A.

As seen on Figure 4.19 , the median based estimate of the relative error profile for $60 < x < 82.5$ m shows a slowly increasing trend for the linear dispersion results, whereas for the composite model the trend is less evident. In order to clarify if this behavior is caused by the decreasing h, the accumulated set of individual depth estimates for the reduced domain ($60 < x < 82.5$ m)is used to analyze the dependency of this performance estimator as a function of the nonlinearity parameter $\delta = A/h$. As can be seen on Figure 4.20(a) , results show a high amount of scatter. However, linear trends fitted to each data set show that relative error increases with nonlinearity, but the slope of the linear fit is much smaller for the case of the composite model. However, when a similar analysis is performed over the absolute value of the relative error, the trend for the linear estimate is almost the same, but for the composite it appears to be almost insensitive on nonlinearity, but biased with a larger value than the one observed from the average profile. This suggests that error is not influenced by the definition of R and its dependency on h, but on nonlinearity instead.

Considering that analysis of the depth estimates for individual cases showed that linear dispersion seems to perform better for shorter periods, a similar analysis can be done using as reference the dispersion parameter $\mu = kh$. Figure 4.20(b) shows the dependency of the absolute value of the relative error as a function of μ. It can be seen that for intermediate waters, the two techniques appear to perform similarly. As water becomes more shallow, it is apparent that composite estimates have a better performance,

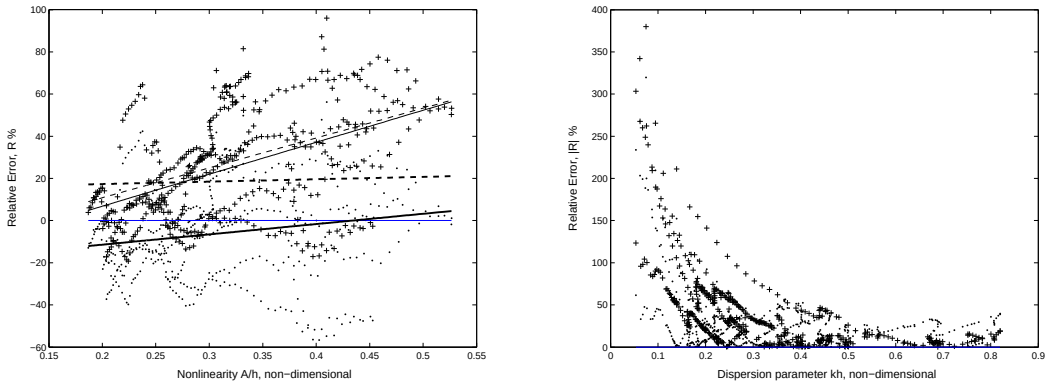

(a) (b)

Fig. 4.20: Relative error as a function of non dimensional parameters for linear dispersion (pluses and thin lines) and composite dispersion (circles and thick lines). Lines correspond to best fit estimates. a) Nonlinearity $\delta = A/h$; b) Dispersiveness $\mu = kh$.

suggesting that the composite model is a better estimator in shallow water.

It must be noted, however, that this analysis considered all the individual estimates of depth, which showed a large variability which hinders the analysis. A true assessment of the performance of both methods and its dependency on δ and μ should be performed when individual estimates are fairly accurate, in order to isolate other effects not taken into account here.

In summary, it appears that the inclusion of nonlinearity effectively improves depth estimation in shallow waters.

4.4.1 Sensitivity analysis for the composite model

Sources of error and sensitivity analysis for nonlinear depth inversions can be classified in a similar way to those described in § 2.4 for the linear case.

First we focus on the sensitivity of the composite dispersion equation upon the wave properties measured ($\sigma(T), k$, and A). Although for the linear dispersion variational calculus provides an analytical expression (Eq. 2.10), the composite dispersion is more complex in terms of the derivatives to be evaluated and a numerical study is used instead. The algorithm is as follows: For a given true depth h_o, it is possible to obtain

a set $\{T_o, k_o, A_o\}$ that satisfy the composite dispersion equation (Eq. 3.1). Then, by introducing a perturbation δ to any of the parameters and assuming the other two constant, a depth estimate $\hat{h}_o$ can be obtained ($\hat{h}_o = f(\delta T, k_o, A_o)$ for example). Thus, the relative error defined on Eq. 4.5b for the depth estimate can be obtained. This results in a set of 3-D surfaces of the relative error, but in order to simplify the analysis 2-D slices are used instead.

The first parameter analyzed is the wave period T. The true water depth is set to $h = 4$ m, and a range of periods between 4 and 15 seconds are used, thus allowing relative water depths to vary from shallow to intermediate. 9 perturbation values are applied ($0, \pm 1, \pm 2, \pm 5, \pm 10$ %), and the slice to be analyzed is selected by means of a fixed amplitude value, $A/h = \delta = 0.25$. This value is expected to be large enough to illustrate the differences of behavior between the linear and the composite model without introducing too much bias. Results are presented in terms of the dispersiveness parameter kh because of generality.

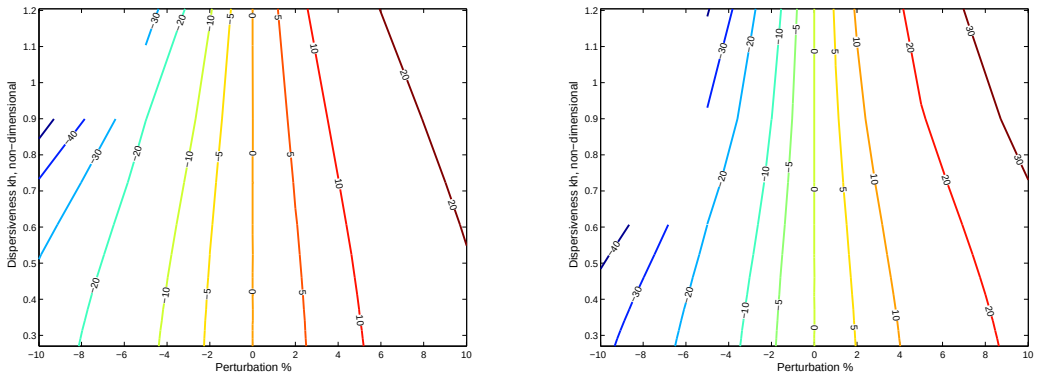

(a) (b)

Fig. 4.21: Relative error maps on depth estimates induced by a wrong estimation of the wave period. True water depth $h = 4$ m, nonlinearity $\delta = A/h = 0.25$ a) Linear dispersion b) Composite dispersion.

Results are shown on Figure 4.21 for both dispersion models. Figure 4.22 shows two transects of these maps at 2% and 5% perturbation. Linear dispersion follows the trend described in § 2.4 , that is, the relative error on the depth estimate at least doubles the period error, and increases exponentially as kh increases, seriously limiting accuracy

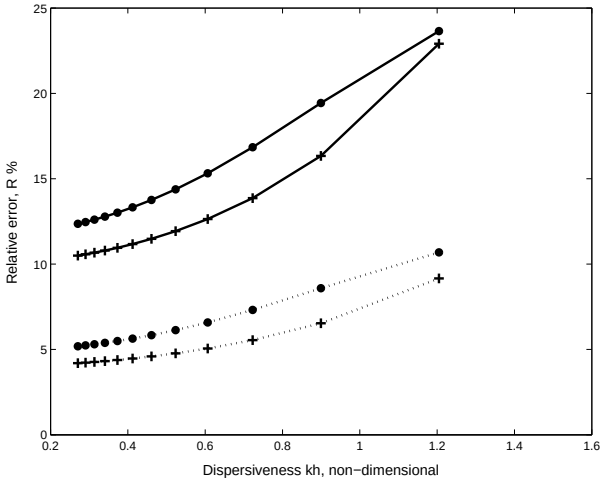

Fig. 4.22: Relative error on depth estimates induced by a wrong estimation of the wave period. True water depth $h = 4$ m, nonlinearity $\delta = A/h = 0.25$. (solid) 5% perturbation; (dotted) 2% perturbation; (pluses) Linear dispersion (circles) Composite dispersion.

for intermediate to deep water. Interestingly, the composite dispersion follows a similar trend, but with larger deviations, thus limiting more the usable range. It should be mentioned, however, that for the present set of results, wave period was estimated typically with less than 1% error, therefore it is expected that observed errors on this study are not related with this type of error. Furthermore, the maximum value used was $kh = 0.8$

The same perturbation set is applied to the case when wavenumber is not correctly estimated. True wavenumbers are estimated by solving the linear and composite dispersion equations with the same water depth, input amplitude and range of periods as before. It should be noted that the calculated wavenumbers are different depending on the equation used. Results are shown on Figure 4.23 for 2% and 5% perturbations. Again, depth errors are more than two times the error on wavenumber. The trend is exponential but with a smaller slope than in the period case, allowing for a somewhat larger range of relative depths. The composite dispersion again shows more sensitivity to this type of error. Even though for the cases under study the largest value of kh was 0.8, the sensitivity on wavenumber could explain a large portion of the error observed, especially when considering that since wave period was accurately estimated, wavenumber errors are directly related with phase speed errors, which showed a large amount of

variability.

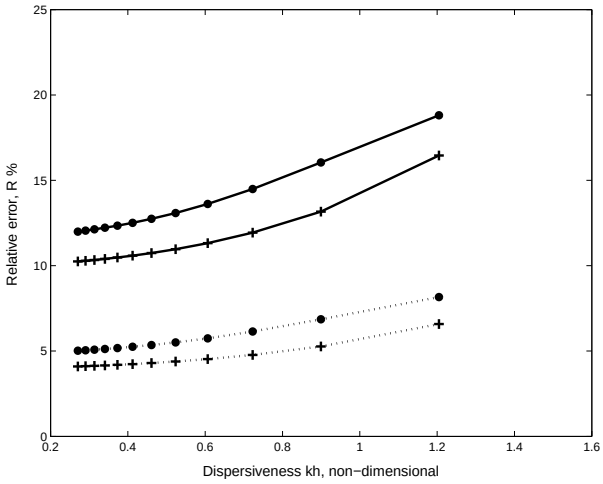

Fig. 4.23: Relative error on depth estimates induced by a wrong estimation of the wavenumber. True water depth $h = 4$ m, nonlinearity $\delta = A/h = 0.25$. (solid) 5% perturbation; (dotted) 2% perturbation; (pluses) Linear dispersion (circles) Composite dispersion.

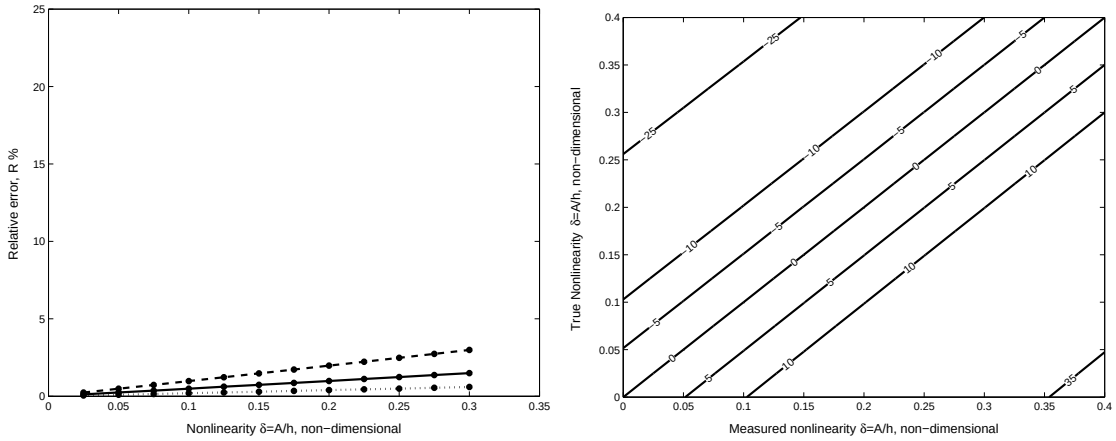

(a) (b)

Fig. 4.24: Relative error on depth estimates induced by a wrong estimation of the wave amplitude. True water depth $h = 4$ m, wave period $T = 18$ s. a) Perturbation analysis (solid) 5% perturbation; (dotted) 2% perturbation; (dashed) 10% perturbation; b) Error map when he measured amplitude is allowed to take any value.

Errors in the estimation of wave amplitude can be studied only for the composite dispersion. The same range of perturbations are applied to wave amplitudes on the range $A = 0.1 - 1.2$ m ($A/h = 0.025 - 0.3$). In this case, the wave period was set to $T = 18$

s in order to simulate shallow water conditions ($kh = 0.23$). As can be seen on Figure 4.24(a) , the error in the retrieved depth is significantly less than the previous cases, showing a linear trend. In fact, the error in depth is much smaller than the input error on amplitude, although is a function of A. Considering this and the current limitations on retrieval of wave amplitude from remote sensing, where rather than small perturbations it is possible to obtain large perturbations, the analysis is extended as to estimate the relative error induced when *any* other value of wave amplitude is used as input. Results are shown on Figure 4.24(b) , where errors up to 35% are observed, showing a one-to-one relation between the relative error and the difference between the measured and the true amplitude (or A/h). The result is not surprising when the definition of relative error and the shallow water approximation are considered. From the latter, written in terms of amplitude following *Hedges* (1976) model

$$c = \sqrt{g(h + A)} \tag{4.8}$$

an estimate of depth $\hat{h}$ can be obtained from a measured amplitude A_m as

$$\hat{h} = \frac{c^2}{g} - A \tag{4.9}$$

Hence, the relative error is

$$\begin{aligned} R &= \frac{(c^2/g - A_m) - h_t}{h_t} \\ &= \frac{(c^2/g - A_m) - (c^2/g - A_t)}{h_t} \\ &= \frac{(A_t - A_m)}{h_t} \end{aligned} \tag{4.10}$$

where it has been assumed that c is the true phase speed and A_t is the true amplitude. Thus, when the linear dispersion is used, $A_m = 0$ the relative error is equal to the true nonlinearity parameter, $R = A_t/h$. This stresses the need to include amplitude dispersion effects in shallow water.

The second type of error is related with the assumption that the inversion technique

used is capable to fully explain the physical processes taking place. To date, most of the observed errors in shallow water have been related with amplitude dispersive effects which have been taken into account in the present study by using the composite model. However, it is apparent that other wave processes may play a role and have not been considered before, mainly because their overall effect can be considered small when compared to the nonlinear effect. Wave set up for instance, needs to be accounted for in the vicinity of the still water shoreline, specially if a nonlinear model is used for the inversions since it is required for estimation of wave amplitude and speeds beyond the shoreline. Accounting for this effect is a complicated process, because it is coupled with the wave height profile, thus requiring an iterative implementation, where wave heights are used to estimate set up, which is used to feedback a new estimate of wave height. Possibly, instead of using a direct inversion method like the composite model, assimilation techniques would be more suitable if wave set up needs to be included.

4.4.2 Summary

Depth inversions using a linear and a nonlinear model were performed for 5 wave conditions. Statistics of error for the average profile obtained showed that the inclusion of nonlinear effects in shallow water reduced the error to the same degree of accuracy reported by previous work obtained using linear dispersion on intermediate to shallow water. Sensitivity analysis showed that a large portion of the error is related with error on the estimation of the phase speed, therefore, an accurate estimate of this parameter is essential. In addition, the analysis showed that if nonlinear effects are not included, relative errors of the order of the nonlinearity parameter are to be expected.

5. CONCLUSIONS

The present study had the main objective to test a nonlinear model for the retrieval of depths using remotely sensed data. Nonlinearity was introduced by means of a simple dispersion equation that required only one extra parameter (wave height) as input and allowed direct comparison of the improvements of the nonlinear technique over traditional depth inversion methods based on the linear dispersion relation.

Results showed improved depths in shallow water, where errors for the average profile retrieved were reduced from 25% to 5% after inclusion of nonlinearity. Thus, inclusion of nonlinearity allowed shallow water estimates to have the same degree of accuracy obtained by previous studies in intermediate water using linear dispersion. In addition, the model tested introduces nonlinearity by means of a wave amplitude profile. Although the source for this parameter for the present study was numerical simulations calibrated with in situ measurements, we do not consider this as a limitation of the model. Instead, numerical simulations were here used as a proxy for a remotely sensed wave amplitude profile. It is expected that future developments of in remote sensing will allow this parameter to be estimated with more ease than free surface maps required by other more complex inversion techniques. If all the variables are measured remotely, nonlinear depth inversion has the additional advantage that it does not require calibration constants, hence its applicability would be straight forward.

Analysis of the error in depth retrievals showed that the accuracy of the method is particularly sensitive to wave period and phase speed estimates, limiting its applicability in intermediate to deep water conditions. Inaccuracies in wave amplitude appear to be less important, but it is essential to include them as the relative error is proportional to the nonlinearity parameter. The usage of the nonlinear model highlighted the importance of other processes that have not been considered in previous depth inversion works, such as wave setup. However, it is considered that the effect of wave setup is secondary and would be confined on a narrow region closer to the still water shoreline, not affecting

significatively depth retrieval outside this region.

The experimental set up used consisted of a barred beach, whose overall shape was not possible to recover from the present data set and algorithm used. However, this is not considered as a failure of the nonlinear inversion technique but rather a lack of skill on determining the celerity profile from the data for the conditions tested and the data set available. It is known that celerity can be correctly estimated under other circumstances, and it is expected that this can be corrected by using other phase speed estimation techniques not implemented yet. Furthermore, the data set evaluated provided little relevant wave information on the shoaling region, where nonlinear effects have been reported to be of importance as well. It is expected that the model tested here would be capable to account for those effects, leading to better depth estimates. However, it seems that extension to the shoaling region would be more exigent on the accuracy of the wave amplitude estimates.

Bibliography

Aarninkhof, S., and R. Holman (1999), Monitoring the nearshore with video, *Backscatter*, *10*(2), 8–11.

Aarninkhof, S., B. Ruessink, J. Roelvink, and A. de Kruif (2003), Quanitification of surf zone bathymetry from video observations of wave breaking, in *Coastal Sediments '03*.

Basco, D. R. (1985), A qualitative description of wave breaking, *Journal of Waterway, Port, Coastal and Ocean Engineering*, *111*(2), 171–188.

Bell, P. S. (1999), Shallow water bathymetry derived from an analysis of X-band marine radar images, *Coastal Engineering*, *37*, 513–527.

Bendat, J. S., and A. G. Piersol (1986), *Random Data Analysis and Measurement Procedures*, second revised ed., John Willey & Sons.

Chen, Q., J. T. Kirby, R. A. Dalrymple, A. B. Kennedy, and A. Chawla (2000), Boussinesq modeling of wave transformation, breaking and runup,II:2D, *Journal of Waterway, Port, Coastal, and Ocean Engineering*, *126*(1), 48–56.

Curtis, W. R., K. K. Hathatway, T. K. Holland, and W. C. Seabergh (2002), Video-based wave direction measurements in a scale physical model, *Tech. Rep. ERDC/CHL CHETN-IV-49*, U.S. Army Corps of Engineers.

Dally, W. R., R. G. Dean, and R. A. Dalrymple (1985), Wave height variation accross beaches of arbitrary profiles, *Journal of Geophysical Research*, *90*(C6), 11,917–11,927.

Dalrymple, R. A., A. B. Kennedy, J. T. Kirby, and Q. Chen (1998), Depth inversion for nonlinear waves shoaling over a barred-beach, in *Proceedings, 26th International Conference on Coastal Engr.*, pp. 2395–2408, ASCE.

Dankert, H., and W. Rosenthal (2004), Ocean surface determination from X-Band radar-image sequences, *Journal of Geophysical Research*, *109*(C04016), doi:10.1029/2003JC002,130.

Dingemans, M. W. (1997), *Water Wave propagation over uneven bottoms*, *Advanced Series on Ocean Engineering*, vol. 13, World Sci., River Edge, N.J.

Dugan, J., H. Suzukawa, C. Forsyth, and M. Farber (1996), Ocean wave dispersion surface measured with airborne IR imaging system, *IEEE Trans, Geosci. Remote Sens.*, *34*(5), 1282–1284.

Dugan, J. P., C. C. Piotrowski, and J. Williams (2001), Water depth and surface current retrievals from airborne optical measurements of surface gravity dispersion, *Journal of Geophysical Research*, *106*(C8), 16,903–16,915.

Goda, Y. (2000), *Random Seas and Design of Maritime Structures*, *Advanced Series on Ocean Engineering*, vol. 15, World Sci., River Edge, N.J.

Grilli, S. T. (1998), Depth inversion in shallow water based on nonlinear properties of shoaling periodic waves, *Coastal Engineering*, *35*, 185–209.

Grilli, S. T., and J. Skourup (1998), Depth inversion for nonlinear waves shoaling over a barred-beach, in *Proceedings, 26th International Conference on Coastal Engr.*, pp. 603–616, ASCE.

Hedges, T. (1976), An empirical modification to linear wave theory, *Proc. Instn. Civ. Engrs.*, *61*(Part 2), 575–579.

Herbers, T., S. Elgar, and R. Guza (1995), Generation and propagation of infragravity waves, *Journal of Geophysical Research*, *100*(C12), 24,863–24,872.

Holland, T. K. (2001), Application of the linear dispersion relation with respect to depth inversion and remotely sensed imagery, *IEEE Transactions on Geoscience and Remote Sensing*, *39*(11), 2060–2071.

Holland, T. K., R. A. Holman, T. C. Lippmann, J. Stanley, and N. Plant (1997), Practical use of video imagery in nearshore oceanographic studies, *IEEE Journal of Oceanic Engineering*, *22*(1), 81–92.

Horel, J. D. (1984), Complex Principal Components analysis:Theory and examples, *Journal of Applied Meteorology*, *23*(6), 1660–1673.

Inman, D. L., R. J. Tait, and C. E. Nordstrom (1971), Mixing in the surf zone, *Journal of Geophysical Research*, *76*(15), 3493–3514.

Izquierdo, P., J. Nieto, C. Guedes Soares, R. S. González, and G. Rodríguez (2005), Comparison of wave spectra from nautical radar images and scalar buoy data, *Journal of Waterway, Port, Coastal, and Ocean Engineering*, *131*(3), 123–131.

Kennedy, A. B., Q. Chen, J. T. Kirby, and R. A. Dalrymple (2000a), Boussinesq modeling of wave transformation, breaking and runup,I:1D, *Journal of Waterway, Port, Coastal, and Ocean Engineering*, *126*(1), 39–47.

Kennedy, A. B., R. A. Dalrymple, J. T. Kirby, and Q. Chen (2000b), Determination of inverse depth using direct Boussinesq modeling, *Journal of Waterway, Port, Coastal, and Ocean Engineering*, *126*(4), 206–214.

Kirby, J. T., and R. A. Dalrymple (1986), An approximate model for nonlinear dispersion in monochromatic wave propagation models, *Coastal Engineering*, *9*, 545–561.

Kirby, J. T., and R. A. Dalrymple (1994), Combined refraction / difraction model REF/DIF1, version 2.5 . Documentation and user's manual, *Tech. Rep. CACR-94-22*, Center for Applied Coastal Research, Ocean Engineering Laboratory, University of Delaware.

Kirby, J. T., G. Wei, Q. Chen, A. B. Kennedy, and R. A. Dalrymple (1998), FUNWAVE 1.0 Fully nonlinear Boussinesq wave model. Documentation and user's manual, *Tech. Rep. CACR-98-06*, Center for Applied Coastal Research, Ocean Engineering Laboratory, University of Delaware.

Kisthawal, C., S. Basu, and S. Karthikeyan (2001), Retrieval of vertical wind profiles during monsoon from satellite observed winds over the Indian Ocean using complex EOF analysis, *Proc. Indian Acad. Sci. (Earth Planet. Sci.)*, *110*(1), 77–86.

Lippmann, T., and R. A. Holman (1991), Phase speed and angle of breaking waves measured with video techniques, in *Coastal Sediments ' 91*, vol. 1, pp. 542–556.

Lynnet, P. J., T.-R. Wu, and P. L. Liu (2002), Modeling wave runup with depth integrated equations, *Coastal Engineering*, *46*, 89–107.

Madsen, P., O. Sørensen, and H.A.Schäffer (1997), Surf zone dynamics simulated by a Boussinesq type model.Part I. Model description and cross-shore motion of regular waves, *Coastal Engineering*, *32*, 255–287.

Mei, C. C. (1989), *The applied dynamics of ocean surface waves*, *Advanced Series on Ocean Engineering*, vol. 1, World Sci., River Edge, N.J.

Merryfield, M., and R. T. Guza (1990), Detecting propagating signals with complex empirical orthogonal functions: A cautionary note, *Journal of Physical Oceanography*, *20*, 1628–1633.

Misra, S. K., A. B. Kennedy, and J. T. Kirby (2003), An approach to determining nearshore bathymetry using remotely sensed ocean surface dynamics, *Coastal Engineering*, *47*, 265–293.

Musumeci, R. E., I. A. Svendsen, and E. Foti (2003), The flow in the surf zone: A fully nonlinear Boussinesq model for breaking waves, *Tech. Rep. CACR-03-05*, Center for Applied Coastal Research, Ocean Engineering Laboratory, University of Delaware.

Narayanan, C., V. Rama Rao, and J. Kaihatu (2004), Model parameterization and experimental design numbers in nearshore bathymetry inversion, *Journal of Geophysical Research*, *109*(C08006), doi:1–/1029/202JC001,765.

Nieto Borge, J. C., and C. Guedes Soares (2000), Analysis of directional wave fields using X-band navigation radar, *Coastal Engineering*, *40*, 375–391.

Nwogu, O. (1993), Alternative form of Boussinesq equations for nearshore wave propagation, *Journal of Waterway, Port, Coastal, and Ocean Engineering*, *119*(6), 618–638.

Piotrowski, C. C., and J. P. Dugan (2002), Accuracy of bathymetry and current retrievals from airborne optical time series of imaging of shoaling waves, *IEEE Transactions on Geoscience and Remote Sensing*, *165*, 27–39.

Puleo, J. A., G. Farquharson, S. J. Frasier, and K. T. Holland (2003), Comparison of optical and radar measurements of surf and swash zone velocity fields, *Journal of Geophysical Research*, *108*(C3), 3100.

Raubenheimer, B., R. Guza, and S. Elgar (1996), Wave transformation across the inner surf zone, *Journal of Geophysical Research*, *101*(C10), 25,589–25,597.

Ruessink, B., P. Bell, I. van Enckevort, and S. Aarninkhof (2002), Nearshore bar crest location quantified from time-averaged X-band radar images, *Coastal Engineering*, *45*, 19–32.

Schäffer, H. A., P. A. Madsen, and R. Deigaard (1993), A Boussinesq model for waves breaking in shallow water, *Coastal Engineering*, *20*, 185–202.

Scott, C. P., D. T. Cox, S. Shin, and N. Clayton (2004), Estimates of surf zone turbulence in a large scale laboratory flume, in *Proceedings, 29th International Conference on Coastal Engr.*, p. in press, ASCE.

Stockdon, H. F., and R. A. Holman (2000), Estimation of wave phase speed and nearshore bathymetry from video imagery, *Journal of Geophysical Research*, *105*(C9), 22,015–22,033.

Suhayda, J. N., and N. R. Pettigrew (1977), Observations of wave height and wave celerity in the surf zone, *Journal of Geophysical Research*, *82*(9), 1419–1424.

Svendsen, I., P. Madsen, and J. B. Hansen (1978), Wave characteristics in the surf zone, in *Proceedings, 16th International Conference on Coastal Engr.*, pp. 520–539, ASCE.

Thornton, E. B., and R. T. Guza (1982), Energy saturation and phase speeds measured on a natural beach, *Journal of Geophysical Research*, *87*(C12), 9499–9508.

Thornton, E. B., and R. T. Guza (1983), Transformation of wave height distribution, *Journal of Geophysical Research*, *88*(C10), 5925–5938.

Trizna, D. B. (2001), Errors in bathymetric retrievals using linear dispersion in 3-D FFT analysis of marine radar ocean wave imagery, *IEEE Transactions on Geoscience and Remote Sensing*, *39*(11), 2465–2469.

van Enckevort, I., and B. Ruessink (2001), Video observations of nearshore bar behavior. Part 1: alongshore uniform variability, *Journal of Geophysical Research*, *106*(C8), 16,969–16,979.

van Enckevort, I., and B. Ruessink (2003), Video observations of nearshore bar behavior. Part 1: alongshore uniform variability, *Continental Shelf Research*, *23*, 501–512.

Wallace, J. M., and R. E. Dickinson (1972a), Empirical orthogonal representation of time series in the frequency domain. Part I: Theoretical considerations, *Journal of Applied Meteorology*, *11*(6), 887–892.

Wallace, J. M., and R. E. Dickinson (1972b), Empirical orthogonal representation of time series in the frequency domain. Part II: Application to the study of tropical wave disturbances, *Journal of Applied Meteorology*, *11*(6), 893–899.

Wei, G., J. T. Kirby, S. T. Grilli, and R. Subramanya (1995), A fully nonlinear Boussinesq model for surface waves. Part 1. Highly nonlinear unsteady waves, *Journal of Fluid Mechanics*, *294*, 71–92.

Wei, G., J. T. Kirby, and A. Sinha (1999), Generation of waves in Boussinesq models using a source function method, *Coastal Engineering*, *36*, 271–299.

Wolf, J., and P. Bell (2001), Waves at Holderness from X-band radar, *Coastal Engineering*, *43*, 247–263.

APPENDIX

A. NONLINEAR DEPTH INVERSION WITH A SYNTHETIC DATA SET

A.1 Introduction

Considering that the inverted depths obtained for the remotely sensed data set can be affected by the phase speed estimates obtained from the remotely sensed data set, a fully synthetic data set is generated by using a phase resolving model to simulate wave evolution and used as input for the phase speed and inversion algorithms. The model is driven by actual data taken at the offshoremost wave gage and the model skill is evaluated at the remaining wave gages by comparing low order statistics for the wave time series, such as mean wave height profile, mean water level profile, skewness and asymmetry.

The selected model is based on the fully nonlinear Boussinesq equations, extended to improve the dispersive characteristics on intermediate water ((*Kirby et al.*, 1998)). In the following we review briefly the characteristics of the model, model set up and calibration parameters.

A.2 FUNWAVE 1-D

FUNWAVE is based on the extended Boussinesq equations (*Wei et al.*, 1995), for fully nonlinear conditions, ie, $\delta = a/h = O(1)$ with improved dispersion by following *Nwogu* (1993) approach. Further extensions to include surf zone phenomena and run-up are included as presented by *Kennedy et al.* (2000a) and *Chen et al.* (2000). In particular wave breaking is incorporated using extra momentum terms with an eddy viscosity formulation. Breaking is not always active, and is turned on when the front slope of the wave (η_t) is larger than a critical value (*Kennedy et al.*, 2000a). Other wave dissipation mechanisms as bottom friction were not included for the present runs but are available on the program code.

The model uses a slot technique to improve numerical stability on the swash region,

where the beach can be alternatively dry or wet. The slots allow for the water level to be below the beach surface, thus simulating a dry beach (*Kennedy et al.*, 2000a).

A.3 Model set-up

A.3.1 Boundaries

In order to provide the appropriate boundary conditions for the model, the bathymetry is slightly modified at both ends.

Offshore boundary The numerical wavemaker is set to be co-located with wave gage at Bay 19 ($x = 23.45$ m), because the free surface time series at this location will be used to drive the model. The source function used by the model (*Wei et al.*, 1999) propagates waves in both directions. Hence an offshore sponge layer is required in order to minimize reflection of these waves and offshore traveling reflected waves from the true bathymetry. The domain offshore from the numerical wavemaker is defined to be flat, with a water depth of $h = 2.21m$. This flat bottom is extended for at least $4L_{off}$, where L_{off} is the wavelength at the peak frequency under study. The value was selected as to include two wavelengths of free wave travel and a sponge layer of the same size. For uniformity on the runs, the numerical domain was set to be the same for all the runs, thus L_{off} was calculated based on the longest period, $T = 8$ s. This selection yields to $L_{off} \approx 36.4m$, thus $4L = 145.6$ m. For simplicity, the total extent of this region was set to $150m$.

Onshore Boundary As to provide enough extent for wave run up, the beach is artificially extended with the foreshore slope ($m = 1/12$). A sponge layer is set on the dry beach, and numerical slots are defined shoreward from the point where $h = 0.5m$. The extension of this portion of the beach played some role on the mean water level profile, as explained later.

A.3.2 Grid size

In order to have maximum spatial resolution, the grid size is set to the minimum value allowing stable runs. This is important for two reasons. First, it improves the dispersive

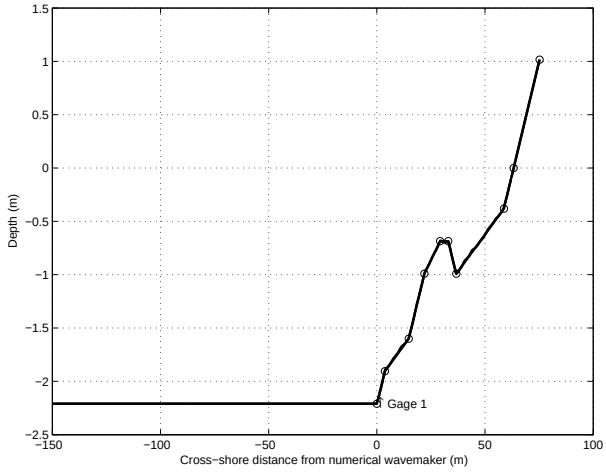

Fig. A.1: Numerical domain for FUNWAVE simulations.

capabilities of the model as shorter wavelengths can be modeled, since the minimum wavelength is twice the grid size. However, this can lead to large water depth to wavelength ratios, and this short wave can increase its size rapidly causing the model to blow up, hence a fine tuning is required on grid size selection. Secondly, in order to ensure model stability a numerical filter is included on the main code in the region seaward of the still water shoreline involving 20 grid points. This causes a rapid decay in wave height in this $20\Delta x$ m region, and to minimize this effect the grid size is required to be as small as possible. Trial and error yield a grid size value of $\Delta x = 0.25m$. The time step is closely related to this value through a Courant type condition, for numerical stability (*Kirby et al.*, 1998), thus

$$dt < \frac{1}{2}\frac{\Delta x}{\sqrt{gh_{max}}} = 0.027s \tag{A.1}$$

where $g = 9.81ms^{-2}$ is the acceleration due to gravity and $h_{max} = 2.21m$. The time step was selected as $dt = 0.01s$.

A.3.3 Other parameters

The model includes several other parameters that can be modified in order to maximize the model skill. Since these parameters played in some cases a major role on the model

behavior, they will be explained in the following.

Breaking parameter *cbkv*: The Boussinesq equations are derived from the assumption of irrotational flow and therefore energy dissipation mechanisms are not included. In an attempt to model wave evolution after breaking, a breaking model capable of preserving wave shape while simulating wave decay is included by modeling the eddy viscosity and its temporal and spatial variation. Thus, breaking dissipation is turned on and off as the eddy viscosity has non-zero or zero values respectively. This is achieved by assuming that the waves are not changing shape locally and that the spatial front slope of the wave $\eta_x \approx \eta_t$, and comparing this value against a reference parameter $\eta_t^* = cbkv\sqrt{gh}$(*Kennedy et al.*, 2000a). *Kirby et al.* (1998) suggests values for this parameter on the range $cbkv \sim 0.35 - 0.65$, with the lower value for bar/through systems. It was found for the present experiments that this parameter plays a major role on the calibration results, with better agreement for $cbkv \sim 0.20 - 0.30$.

Slots width and shape (δ, λ) : In order to model the moving shoreline, a permeable seabed is modeled using a slot technique, allowing for the water level to be below seabed elevation (*Kirby et al.*, 1998), by altering the cross-section of the beach using the following definition (*Kennedy et al.*, 2000a):

$$b(\eta) = \begin{cases} 1, & \eta \geq z^* \\ \delta + (1-\delta)\exp^{\lambda(\eta - z^*)/h_0} & \eta < z^*. \end{cases} \tag{A.2}$$

by the addition of a narrow slot of width δ (assuming a unit width beach) and λ controls the transition between the slot and the actual cross-section of the beach.

Typically the slot domain is defined shoreward of the location where the water depth is $h = 0.5$ m. Sensitivity tests run on the extent of the slot domain did not show important variations. δ and λ showed to have some effect on the mean water profile, and are calibrated for each run.

Filtering *itfltr*: High frequency harmonics are numerically generated due to nonlinear interaction as the program runs. These short wavelength waves can grow quickly and cause the model to blow up. One way to overcome this is through numerical filtering, but this procedure may also remove harmonics actually generated by nonlinear energy transfer. Therefore, filtering should be used as little as possible. *Kirby et al.* (1998) suggests that good results are obtained when filtering every 4 wave periods. For the present experiments, filtering was tried every 800, 1600 and 3200 time steps. The lower value is equal to $3T$ for the shorter wave ($T = 2.7$ s) and the higher value is exactly $4T$ for the longer wave ($T = 8.0$ s). Sensitivity tests showed little variation and filtering is done every 3200 time steps for all the cases.

Source function width *swidth*: FUNWAVE uses a spatially distributed mass source for wave generation instead of a line source. The cross shore profile for this function is expressed in terms of a Gaussian shaped profile, whose width W is found to be of order half wavelength ($W = swidthL/2$), where *swidth* is of $O(1)$.

Sensitivity runs on this parameter showed that it affects the wave height profile nearby the source up until the breaking point, showing the corresponding Gaussian-shaped profile and typically wave height values showed an inverse correlation with *swidth*. *Wei et al.* (1999) points out that the region inside the source is basically "wasted space", because the waves generated here are not the same as the target waves in the far field, but this region has to be large enough to provide a proper far field representation. In an attempt to maximize the effective domain, an intermediate value of *swidth*=0.45 was selected and used for all cases. This value is consistent with the range *swidth*=0.3-0.5 proposed by *Wei et al.* (1999).

A.3.4 Reference statistics

In general, the numerically generated free surface time series is compared "by eye" with their corresponding in situ data. However, this evaluation remains subjective and for long time series it can be more complicated to make an accurate assessment. Hence, the use of some sort of statistics is required.

The first method, valid for both random and monochromatic cases is the evaluation of the wave height profile, and in this case the root-mean-square height is calculated as (e.g. *Goda*, 2000)

$$H_{rms} = \sqrt{8m_0}, \qquad m_0 = \frac{1}{t}\int_0^t \eta_0^2(t)dt \tag{A.3}$$

where $\eta_0(t) = \eta(t) - \bar{\eta}$ is the mean removed free surface elevation, where the mean water level is calculated as

$$\bar{\eta} = \frac{1}{t}\int_0^t \eta(t)dt \tag{A.4}$$

In the following, the mean removed free surface profile will be denoted as η unless otherwise stated.

To measure the nonlinear behavior of the model, higher order spectral estimates are computed from the free surface profiles to account for right-left and crest-through shape differences. Following *Kennedy et al.* (2000a), wave asymmetry is defined as

$$A_s = \frac{\langle H(\eta)^3 \rangle}{\langle \eta^2 \rangle^{3/2}} \tag{A.5}$$

where H denotes the Hilbert transform and $\langle\rangle$ is the mean operator. Skewness, related to crest-through shape is defined as

$$S_k = \frac{\langle \eta^3 \rangle}{\langle \eta^2 \rangle^{3/2}} \tag{A.6}$$

A.4 Results

A.4.1 Model calibration

As pointed out above, the first assessment for the model is in terms of the comparison of the free surface profiles at the locations where real data is available. First we analyze the random cases, where very good agreement is obtained specially for the offshore gages at bays 13,11 and 9. As we progressed onshore, some individual peaks show a phase shift, but the overall structure of the wave train is well obtained. For all the conditions,

the last wave gage (bay 03) shows less agreement, the reason being the presence of a numerical filter at the shoreline in the model. As would be expected, the model skill is dependant on the dispersive properties of each condition.

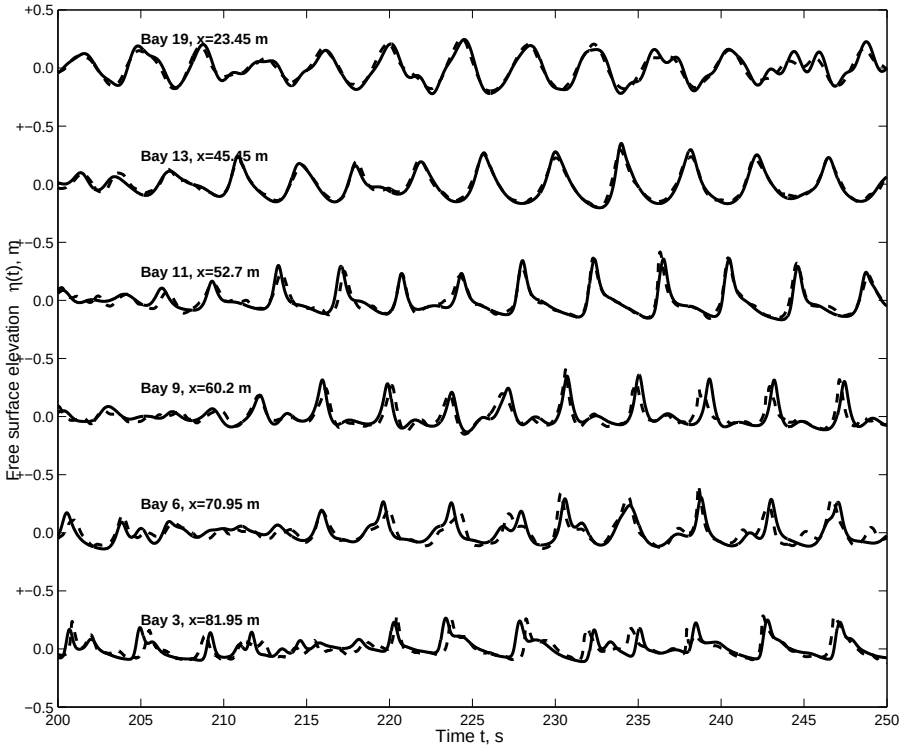

Fig. A.2: Sample free surface time series $\eta(t)$ from FUNWAVE simulations for for an irregular case, $T_p = 4.0$ s, $H_s = 0.40$ m. Numerically generated (solid) and experimental (dashed) free surface series.

Figure A.2 shows a sample result for irregular case 10, T_p=4.0 s and H_s =0.40 m. For the regular wave conditions, a similar trend is observed, with the model showed better agreement for cases with low values of kh at the wavemaker. Although agreement is good for the offshore gages (bays 19 and 13), after breaking occurs the model fails to catch the surface profile for the more dispersive conditions. For instance, for periods shorter than $T = 5.0$ s (regular) the model is unable to match the saw-tooth profile observed shoreward of the bar, where waves appear to be reforming and sometimes reshoal. The model typically predicts waves with flatter troughs and peaked crests in this region, with peaks larger than than those observed for the in situ measurements (e.g. bay 09 on Figure A.3). Although the same pattern is somewhat observed for the longer periods,

the presence of secondary waves and height of the peaks is better matched by the model resulting in an overall good agreement. Figure A.4 shows the case with best agreement for regular waves, corresponding to the longer period.

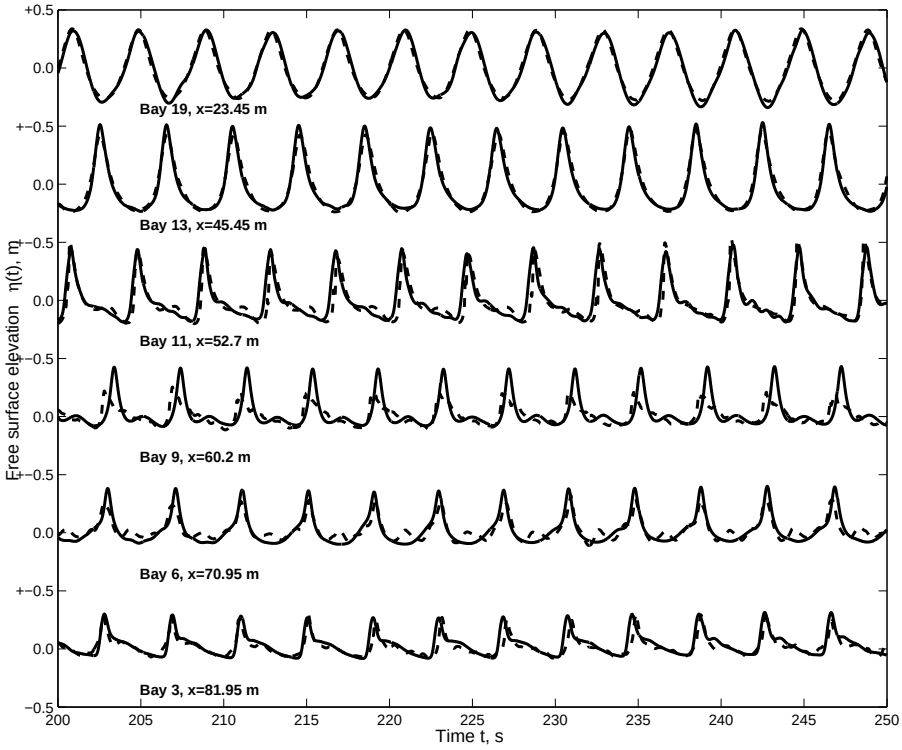

Fig. A.3: Sample free surface time series $\eta(t)$ from FUNWAVE simulations for an regular case, $T = 4.0$ s, $H = 0.60$ m. Numerically generated (solid) and experimental (dashed) free surface series.

Wave height profile An example result for irregular cases can be seen on Figure A.5 a), where agreement is very good, despite the by eye observed differences for individual waves. It should be noted, however, that agreement is highly dependant on the breaking parameter *cbkv*. Furthermore, spatial resolution of the experimental sets is too coarse to identify the breaking location, making the choice of the best fit somewhat arbitrary. Two locations show a similar level of disagreement for all runs (both regular and irregular). At bay 9, located at the bar trough, numerical data tends to overpredict wave height. Bay 3 shows a very poor agreement due to the presence of the numerical filter previously mentioned. For regular cases (see Figure A.6 a) for an example), agreement was less

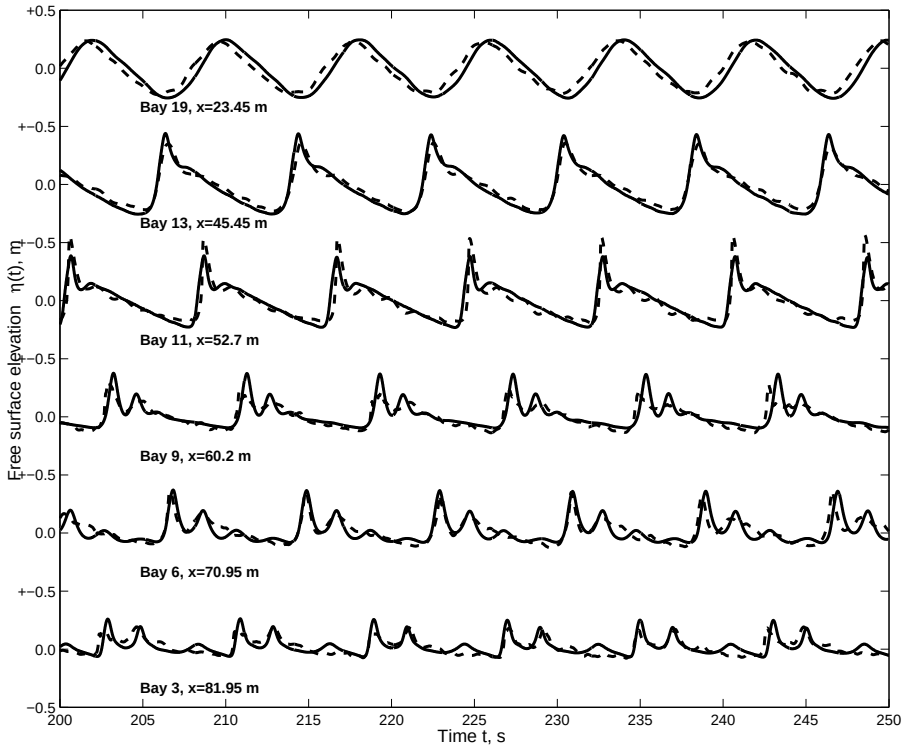

Fig. A.4: Sample free surface time series $\eta(t)$ from FUNWAVE simulations for an regular case, $T = 8.0$ s, $H = 0.40$ m. Numerically generated (solid) and experimental (dashed) free surface series.

satisfactory. Again, selection of the parameter *cbkv* plays an important role on the profile characteristics. In general, the choice was oriented to low values of *cbkv*, which implies that the model will turn on breaking with a less pronounced front slope, thus introducing dissipation earlier. This choice was made on the basis to obtain a better match for the overall profile, rather than matching the wave height for the highest point. The combined effect on wave decay due to breaking and de-shoaling on the shoreward side of the bar is not well predicted by the model. Thus, allowing the model to break later (with higher values of *cbkv*) resulted in overprediction of wave heights for the remainder of the beach.

Mean Water Profile Agreement is generally good for both random and regular cases (Figure A.5 and Figure A.6 b)). It should be noted that, following *Kennedy et al.* (2000a), the result for mean water level from the FUNWAVE runs at the offshoremost gage is set to be equal to the observed value from the experiments and the remainder

points are corrected accordingly. After this correction, agreement is usually good before and over the bar, but agreement deteriorates after the bar. Although the profile shows a similar shape for the numerical and actual data, the numerical values are slightly larger than the observed ones. Interestingly, it was found that the mean water level profile is dependant on the extent of the dry portion of the beach, showing an asymptotic behavior as this part of the domain is expanded. One possible reason for this is the effect of the slots on the overall mass of the model, but this has not been analyzed further. The total length of the domain was selected as to minimize this effect using a reasonably large dry beach.

Skewness and Asymmetry Both statistics show good agreement for irregular cases (Figure A.5 c) and d)), but agreement deteriorates for the regular ones, specially skewness (Figure A.6 c), where small deviations on the overall shape appear to have a large importance on the statistic, especially the observed differences in wave height. In some regular cases (not shown here), asymmetry also show poor agreement caused by phase shifts on the location of the peaks. However, considering that our interest is focused on the wave height profile, calibration was based on the low level statistics wave height and set up.

A.4.2 Wave parameters estimation

After the model has been calibrated for each run, the resulting free surface maps consisting of 213 cross shore locations and 327.68 seconds of simulation are used to estimate wave parameters such as wave phase speed, frequency and wavenumber.

Interestingly, the technique that offered an overall better estimation is CEOF analysis. In particular, for regular cases the first mode explained typically more than 65% of the total variance, with some leakage to modes 2 and 3. Periods were retrieved again with high accuracy (within 1%), and wavenumber profiles showed a scatter-free profile. Interestingly, as can be seen on Figure A.7 an oscillatory pattern was markedly visible, apparently consistent with the findings of *Grilli and Skourup* (1998) for regular waves over barred beaches. The front technique using zero-up crossings was also tested, showing

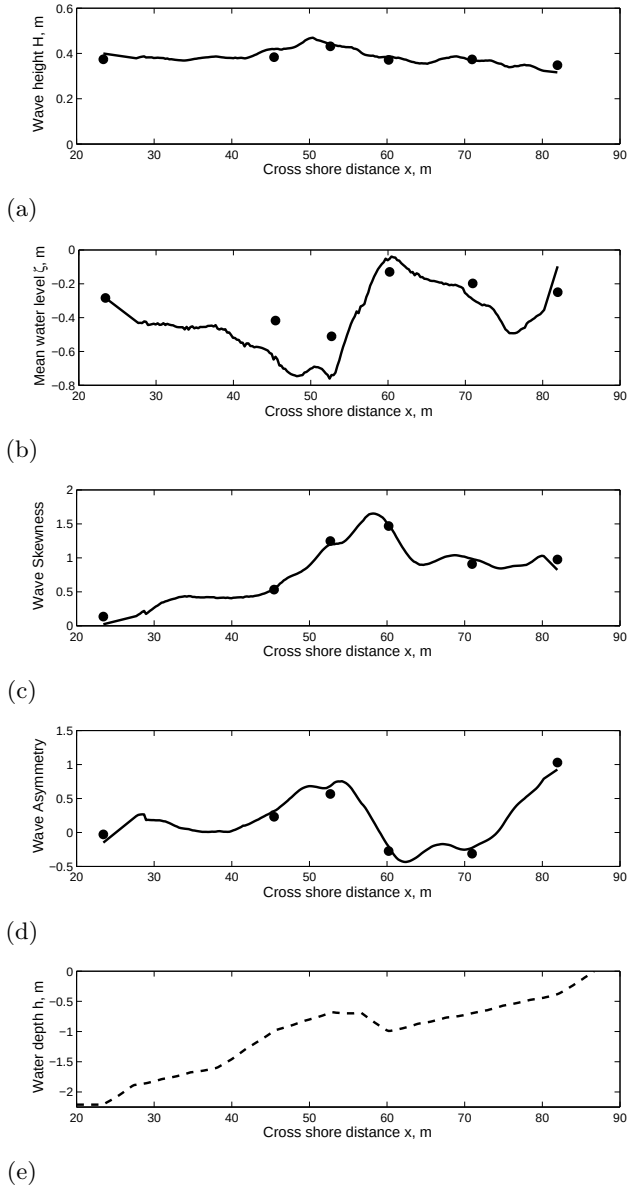

Fig. A.5: FUNWAVE calibration profiles for an irregular case, T_p=4.0 s, H_s = 0.40 m. Experimental data (circles), FUNWAVE (lines). a) Wave height profile; b) mean water level profile; c) skewness profile; d) asymmetry profile; e) bathymetry.

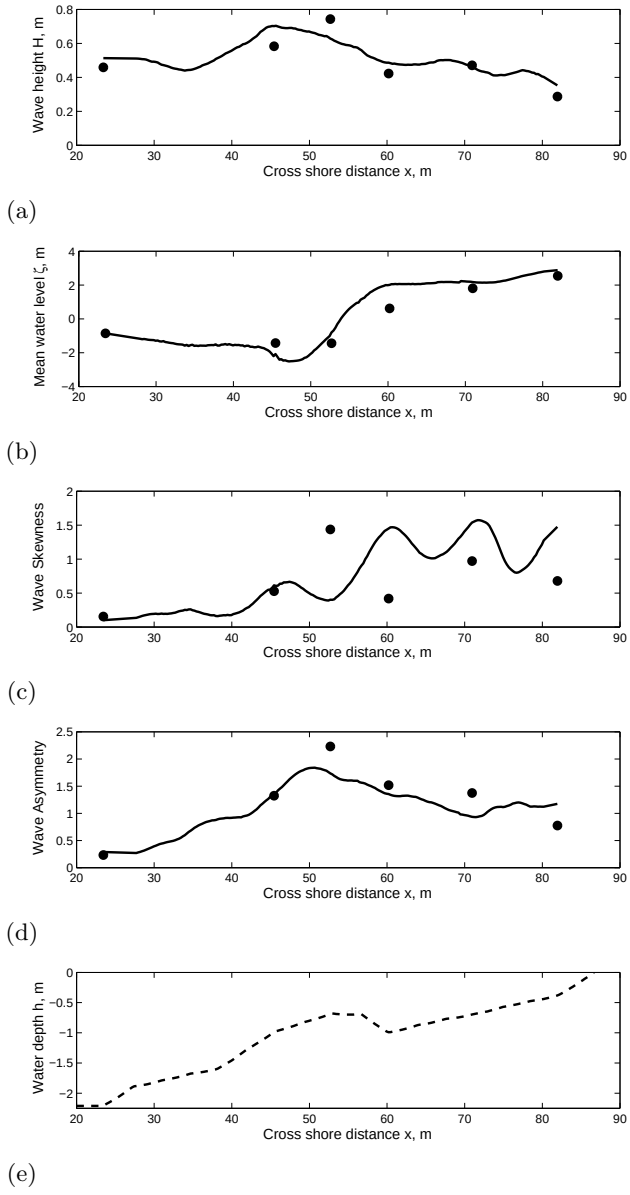

Fig. A.6: FUNWAVE calibration profiles for a regular case, T=8.0 s, $H = 0.40$ m. Experimental data (circles), FUNWAVE (lines). a) Wave height profile; b) mean water level profile; c) skewness profile; d) asymmetry profile; e) bathymetry.

a noisy yet not oscillatory behavior. The difference between the two profiles suggest that front tracking techniques are related with more than one frequency acting simultaneously, thus changing wave shape and the relative location of the front, making the use of a single frequency equation (like the dispersion equation) less obvious. This oscillatory behavior occurred on all regular cases, and consequently were discarded for the inversion because of the known influence of the speed estimates on the inversion technique.

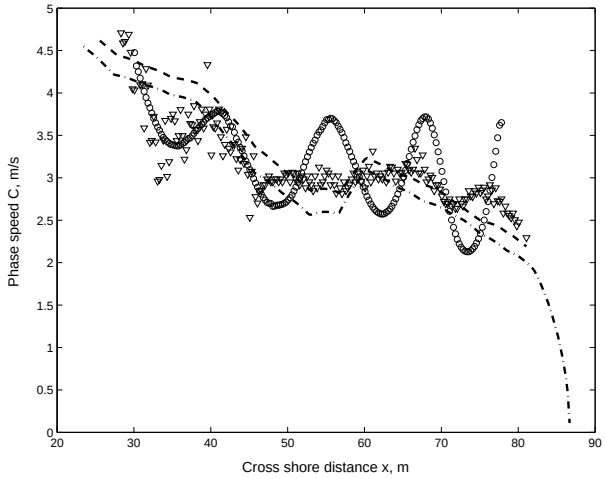

Fig. A.7: Estimated phase speed profile using CEOF (mode 1) for a regular case, $T = 8.0$ s, $H = 0.40$ m. Speed estimate for mode (circles), front tracking (triangles) theoretical linear dispersion (dash-dot) and composite dispersion with FUNWAVE amplitude (dashed).

For irregular cases, CEOF analysis typically returned first modes explaining 50% of the variance. Period estimates from this technique were typically within 1% of the real period, with a single outlier case showing a 5% deviation. Wavenumbers (and consequently speeds) showed relatively scatter-free profiles, with a profile that resembles the overall bar shape.

A.4.3 Depth inversion

Both linear and nonlinear depth inversion methods were tested on the synthetic data set. These sets cover a larger offshore domain than the video set, thus allowing estimation of depths before and over the bar. On the other hand, considering that the numerical filter imposed affected the time series close to the shoreline, the domain is slightly shorter than

the video domain near the shoreline. Depths were inverted for each of the 4 irregular wave cases, and the median profile estimated from these. We focus on the performance of the methods for the average profile only, shown on Figure A.8

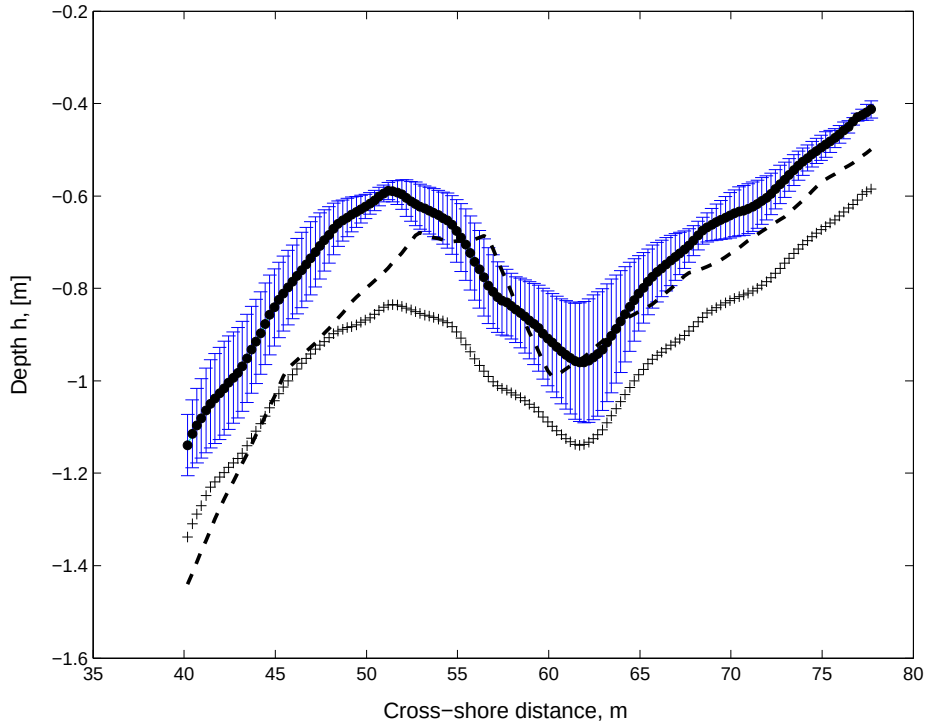

Fig. A.8: Estimated average depth profile for synthetic free surface data sets using linear (pluses) and composite (dots) dispersion. Vertical error bars correspond to one standard deviation for the composite model .

It can be observed that both methods predict the overall structure of the bar-trough system, although showing an offshore shift for the bar location, which has not been investigated in detail. Somewhat surprisingly, the composite model performs a very good job on the trough of the bar, a region where typically field based inversions struggle. This behavior can be attributed to the use of a synthetic data set, where the observed signal corresponds with the waveform itself and not with other wave related phenomena, for instance the roller. As mentioned before, it is possible that those elements can have non zero relative velocities which cause erroneous speed estimates. Analysis of the error showed that both methods have a similar performance when comparing relative RMS

errors ($O(15\%)$), suggesting that each method is strong but in different sections of the profile, a behavior that can be observed on Figure A.8 , where offshore of the bar the linear method appears to perform very well. Once waves begin to break, the composite method seems to perform better.

A.5 Summary

By using a synthetic data set was possible to test the algorithms implemented to be used with remotely sensed data. The overall structure of the bar-trough system was recovered with a typical bias of -9 cm (10 cm for the linear inversion), and relative RMS of 14% (18% linear). The bar location showed an offshore bias, but this is expected to be a result of the hydrodynamics of the model rather than a flaw of the depth inversion algorithm.

.